ROYAUME DU MAROC
Université Mohammed V - RABAT -
جامعة محمد الخامس – الرباط –
Faculté des sciences
كلية العلوم
CENTRE D'ETUDES DOCTORALES - SCIENCES ET TECHNOLOGIES

N° d'ordre : **3735**

THESE

En vue de l'obtention du : ***DOCTORAT***

Structure de Recherche *: Laboratoire de la Matière Condensée et Sciences Interdisciplinaires (LaMCScI)*
Discipline *: Physique Informatique*
Spécialité *: Physico-chimie des matériaux et nanotechnologie*

Présentée et soutenue le: 24/12/2022 par :

Majid EL Kassaoui

Theoretical investigations for hydrogen storage properties improvement in metal-organic frameworks and new bi-dimensional systems

JURY

Hamid EZ-ZAHRAOUY	PES, Université Mohammed V-Rabat, Faculté des Sciences	Président/Rapporteur
Rachid BENCHRIFA	PES, Université Mohammed V-Rabat, Faculté des Sciences	Examinateur/Rapporteur
Ahmed HOURMATALLAH	PES, Université Sidi Mohamed Ben Abdellah, Ecole Normale Supérieure	Examinateur/Rapporteur
Mohammed LOULIDI	PES, Université Mohammed V-Rabat, Faculté des Sciences	Examinateur
Mustapha JOUIAD	PES, Université de Picardie Jules Verne, France	Examinateur
Omar MOUNKACHI	PH, Université Mohammed V-Rabat, Faculté des Sciences	Examinateur
Marwan LAKHAL	PA, Université Ibn Zohr, Ecole Supérieure de Technologie de Laâyoune	Invité
Abdelilah BENYOUSSEF	PES/Expert, Académie Hassan II des sciences et techniques-Rabat	Co-Directeur
Abdallah El KENZ	PES, Université Mohammed V-Rabat, Faculté des Sciences	Directeur de Thèse

Année Universitaire: 2022/2023

ROYAUME DU MAROC
Université Mohammed V
- RABAT -
جامعة محمد الخامس
– الرباط –
Faculté des sciences
كلية العلوم

DOCTORAL THESIS

By

Majid EL Kassaoui[1]

Supervised by

Abdallah El Kenz[2]

Theoretical investigations for hydrogen storage properties improvement in metal-organic frameworks and new bi-dimensional systems

[1]e-mail:psmajid0@gmail.com
[2]e-mail:akenzele@yahoo.com
Laboratory of Condensed Matter and interdisciplinary Sciences (LaMCScI)

Acknowledgment

This thesis was carried out at the Laboratory of Condensed Matter and Interdisciplinary Sciences (LaMCScI) of the Faculty of Sciences, University Mohammed V-Rabat, Morocco under the supervision of Prof. **Abdallah EL KENZ**.

At first, I would like to express my sincere gratitude to my supervisor Professor **Abdallah EL KENZ**, for his patience and support. His advice, constructive remarks, and scientific input have been of great help to me throughout this research project. It is a privilege to be your student. Thank you for the trust you have placed in me and I hope this work lives up to your expectations.

I am also very grateful to my co-supervisor Prof. **Abdelilah BENYOUSSEF** for both the productive conversations and valuable suggestions wich have contributed greatly to the improvement of the thesis.

I would also thank the thesis committee for reviewing my work and giving their insightful and useful comments. It is an honor for me that they agree to judge this work.

I would like to thank Prof. **Hamid EZ-ZAHRAOUY** from University Mohammed V-Rabat, Faculty of Science, to be the president of the jury members of this thesis. I am also grateful to him for his interest and time devoted to reporting this manuscript.

I would like also to offer my thanks to Prof. **Rachid BENCHRIFA** from University Mohammed V-Rabat, Faculty of Science, for reporting and reviewing this PhD thesis.

I would also like to extend my thanks to Prof. **Ahmed HOURMATALLAH** from Ecole Normale Supérieure, Bensouda, Fès, for reporting and reviewing this PhD thesis.

I owe my sincere and earnest thankfulness to Prof. **Mohammed LOULIDI** from University Mohammed V-Rabat, Faculty of Science, for patience in revising my papers,

for providing invaluable insight and constructive criticism to the work I have done. It has truly been a great pleasure to work with you.

I would like also to thank Prof. **Mustapha JOUIAD** from University of Picardie Jules Verne, France, for reviewing this thesis.

I would like also to express my thanks to Prof. **Omar MOUNKACHI** from University Mohammed V-Rabat, Faculty of Science, for reviewing this thesis.

I would like to take this opportunity to express my sincere gratitude to Prof. **Marwan Lakhal** for his helpful guidance, suggestions, contributions, and encouragements throughout the course of this work. My thanks also go to my LaMCScI's colleagues.

At last, my gratitude goes to my parents, my brothers, to my friends and every people who helped and supported me in any way during during my research.

Abstract

With the exponential increase in demand for effective and renewable energy, the hydrogen era has begun. Hydrogen energy is an ideal candidate to replace fossil fuels due to its high energy density, ease of availability and zero carbon emission. However, the development of a suitable storage media is the biggest challenge toward the realization of H_2 based mobility applications. To date, the common H_2 storage practices are exclusively in the form of high-pressure gas cylinders and liquid hydrogen, which prevent its applications due to safety concerns and socio-economic constraints. Therefore, H_2 storage on solid materials via physisorption is an ingenious alternative. We study two interesting axes in hydrogen storage materials.

The first is a new approach aimed at tuning the hydrogen storage properties of metal organic frameworks type MOF-5. Using calculations of the density functional theory (DFT) comprising van der Waals interactions, we show that our system may reach a maximum gravimetric storage capacity of 4.09 wt% for multiple hydrogen molecules. Moreover, the decoration of Li, Be and Na combined to the substitution, shows an exceptional improvement of hydrogen storage properties. For example, Mg-MOF-5:Li_2 has a capacity up to 5.41 wt% and 513 K as desorption temperature.

In the second axis, *ab initio* calculations have been also applied to study the potential of t-graphene-like boron nitride ($t - B_4N_4$) and beryllium carbide (Be_2C) as new 2D material for hydrogen storage. Our results show that the adsorption energy of H_2 on the Li-decorated $t - B_4N_4/Be_2C$ monolayer is appropriate for hydrogen storage, with a maximum gravimetric capacity of 12.47 wt% and 10.21 wt% for $t - B_4N_4$ and Be_2C, respectively. In addition, the desorption temperature estimates were validated by AIMD simulations of hydrogenated Li@$t - B_4N_4$ and Li@Be_2C. To summarize, these materials are interesting candidates for hydrogen storage due to their promising hydrogenation properties.

Key words: Hydrogen storage; Metal-organic framework-5; 2D materials; Ab initio calculations; AIMD; Adsorption; Metal functionalization.

Résumé

Avec l'augmentation de la demande énergétique mondiale, l'hydrogène peut être considérer comme un vecteur énergétique renouvelable et écologique et l'une des solutions envisageables pour une transition énergétique vers l'énergie propre. Cependant, cet élément est fortement explosif. De ce fait, le mode de stockage approprié pour un usage sécuritaire reste le stockage solide, toute fois, la capacité de stockage pour ce mode reste limiter et les conditions d'utilisation plus au moins sophistiqué. Dans ce contexte, un intérêt considérable est porté sur le stockage de l'hydrogène dans les matériaux qui répondent à certaines propriétés thermodynamiques fondamentales et aux critères de la US-DoE.

Comme premier axe, les matériaux poreux de type MOF-5 sont étudiés. Vue leurs hautes capacités de stockage et de leur grande surface spécifique, ils sont un bon candidat pour le stockage d'hydrogène. Les résultats obtenus à la fois pour la décoration et la substitution, montrent que ces deux stratégies améliore considérablement les propriétés de dé/hydrogénation de la cellule unitaire-MOF-5 suite à la diminution remarquable d'énergies de formation, et qui est traduit également par l'augmentation de la température de décomposition vers l'ambiante. En ce qui concerne la capacité de stockage, elle est environ 5.41% par poids pour le Mg-MOF-5 décoré par Li. Ces résultats s'accordent avec les normes fixées par US-DoE.

D'autre part, des calculs basés sur la modélisation *ab initio* ont été effectué pour étudier le potentiel du nitrure du bore tétragonal ($t - B_4N_4$) et du carbure de béryllium (Be_2C) en tant que nouveaux matériaux 2D pour le stockage de l'hydrogène. Les résultats obtenus montrent que l'énergie d'adsorption de l'hydrogène sur la monocouche $t - B_4N_4/Be_2C$ décorée par Li est convenable pour le stockage, avec une capacité de stockage de 12.47 et 10.21% par poids pour $t - B_4N_4$ et Be_2C, respectivement.

Mots clés: Stockage de l'hydrogène; Matériaux poreux; Matériaux 2D; la théorie de la densité fonctionnelle; AIMD; Température de désorption; Hydrogénation.

Résumé détaillé

Aujourd'hui, avec le développement industriel et la croissance démographique, nous épuisons de plus en plus les ressources énergétiques fossiles, comme le charbon, le pétrole et le gaz naturel. De ce fait, le monde s'interroge sur deux problématiques. L'une est liée au risque d'épuisement de ces ressources, et l'autre à la pollution environnementale, amplifié par l'émission de gaz à effet de serre. Dans ce sens, la recherche de source d'énergie alternative propre, permettant d'ouvrir la voie au développement de systèmes de stockage d'électricité d'une manière efficace et à faible coût est d'une necessité primordiale. Les énergies solaire, éolienne et géothermique sont des sources renouvelables connues et déjà exploitées depuis longtemps mais avec une contrainte d'intermittence au niveau de la production. Actuellement, l'utilisation de l'hydrogène (H_2) comme vecteur énergétique renouvelable et écologique est l'une des alternatives sérieuses envisagées pour l'industrie et d'autre application stationnaire et mobile. Cependant, l'adoption massive de l'économie de l'hydrogène est lente en raison du manque d'incitations et de difficultés techniques au niveau de son stockage.

Jusqu'à maintenant, le stockage de l'hydrogène dans des matériaux à l'état solide semble être la solution la plus pratique étant donné qu'il s'agit d'une méthode plus sûre que la compression à haute pression ou la liquéfaction à faible température. C'est pour cela que de nombreuses recherches sont menées par les scientifiques et les industriels pour trouver des matériaux adéquats pour l'absorption et l'adsorption de l'hydrogène. À cet effet, les matériaux organo-métalliques microporeux (Metal-Organic Frameworks: MOFs) sont des composés potentiel pour le stockage de l'hydrogène à l'état solide en raison de la multiplicité des configurations possibles, de leur porosité permanente, du large volume de leur pore et de la grande capacité de stockage (16% par poids). Cependant, si cette capacité est obtenue sur ce MOFs dans un intervalle raisonnable de pression, il n'en demeure pas moins qu'elle est obtenue à une température de désorption de 77 K. Basé sur ceci, nous avons décidé de faire une étude approfondie sur l'influence des différentes stratégies pour améliorer les propriétés d'hydrogénation de MOF-5.

Afin d'étudier le stockage de l'hydrogène dans le type MOF-5, de comprendre les mécanismes physiques sous-jacents et de proposer des approches qui améliorent ses pro-

priétés de stockage de l'hydrogène, tout en répondant aux critères de la US-DoE, nous avons mené une étude théorique des propriétés structurales, électroniques, thermodynamiques en utilisant les calculs basés sur le premier principe de la théorie fonctionnelle de la densité (DFT). Dans ce contexte, et pour la première fois pour ce modèle, les résultats des calculs montrent que le connecteur-MOF-5 de formule général $Zn_4O(C_8H_4O_4)_3$ a une bonne stabilité thermodynamique avec une température de décomposition de 115.4 K. De plus, l'analyse des liaisons chimiques des atomes du connecteur montre un bon accord entre les résultats expérimentaux et théoriques. D'autre part, une étude détaillée de l'effet de la décoration et la substitution sur la stabilité, les propriétés thermodynamiques et d'hydrogénation de la cellule unitaire-MOF-5 a été réalisée. Les résultats obtenus à la fois pour la décoration (par : Li, Be et Na) et la substitution (par : Mg et Cd), montrent que ces deux méthodes améliorent considérablement les propriétés de dé/hydrogénation de la cellule unitaire-MOF-5 suite à la diminution remarquable d'énergies de formation ($-38.91 kJ.mol^{-1}.H_2$), et qui est traduit également par l'augmentation de la température de décomposition vers l'ambiante (300 K). Concernant les capacités, elles sont de l'ordre de 5.41, 4.78 et 4.45% en poids pour Mg-MOF-5:Li_2, Zn-MOF-5:Li_2 et Cd-MOF-5:Li_2, respectivement. Pour la température de désorption elle est de 513 pour Mg-MOF-5:Li_2 et de 463 K pour Zn-MOF-5:Li_2. D'où, nous constatons que ces améliorations pourraient conduire à l'utilisation de ces modèles dans des applications de stockage de l'H_2 avec des normes acceptables données celons US-DoE.

Pour le deuxième axe, nous avons focalisé nos efforts sur une étude évaluant le potentiel du nitrure du bore tétragonal ($t-B_4N_4$) et du carbure de béryllium (Be_2C), en tant que nouveaux matériaux 2D pour le stockage de l'hydrogène. L'intérêt de cette étude réside dans la compréhension fondamentale du comportement de ces deux composés et l'amélioration de leurs performances d'hydrogénation lors de la décoration par des atomes légers. Les résultats obtenus montrent que l'énergie d'adsorption de l'hydrogène sur la monocouche $t-B_4N_4$ et Be_2C décorée par Li est appropriée pour ce type de stockage, avec une capacité de 12.47 et 10.21% par poids pour $t-B_4N_4$ et Be_2C, respectivement. De plus, basé sur la dynamique moléculaire ab initio (AIMD), les estimations de température de désorption pour ces systèmes hydrogénés ont été validées. A partir d'une analyse de l'énergie d'activation des systèmes considérés, nous remarquons que la diffusion de la molécule H_2 est plus rapide à la surface de $t-B_4N_4$ et Be_2C par rapport au graphène monochouche.

List of Figures

1.1 Simple phase diagram for hydrogen [12] 6
1.2 (left) Several hydrogen storage methods. (right) Comparison of gravimetric/volumetric density of different hydrogen technologies [4]. 8
1.3 Vessel types of hydrogen compressed storage [19]. 9
1.4 Schematic of a cryogenic tank for liquid H_2 storage. 10
1.5 Hydrogen storage density under different pressure and temperature conditions. 11
1.6 Chemisorption of metal crystal and hydrogen storage. 13
1.7 Structure of various carbon materials: fullerenes (left) and nanotubes (right). 15
1.8 Structures of microporous materials: (a) zeolites, (b) covalent organic frameworks, and (c) metal organic frameworks. 16
1.9 Historical developments in MOF synthesis. 17
1.10 Conventional solvothermal synthesis of MOF structures 18
1.11 Crystal structure of MOF-5 (C, black; Zn, blue; O, red; gust molecule, yellow sphere and all H atoms have been omitted for clarity) [65]. 19
1.12 Series of isoreticular metal-organic frameworks (IRMOFs-n with n=1-8, 10, 12, 14, 16) based on MOF-5. Yellow spheres indicate the location of the cavities in the cubic cage. 20
1.13 (left) Hydrogen gas sorption isotherm for MOF-5 at (A) 78K and (B) 298 K. (right) A plot between excess gravimetric H_2 uptake, measured at 77 K and 2 MPa or above, for various MOFs. 21
1.14 Examples of several 2D-materials, each containing different chemical elements and atomic configurations. 22

2.1 Illustration of the concept behind the pseudopotential and the pseudo wave function. The solid blue lines show the all-electron wave function Ψ^{ae} and the ionic potential V^{ae}. The dashed lines show the pseudo wave function Ψ^{ps} and pseudopotential V^{ps}. r is the distance from nuclear. 33

3.1 Representative schema of a) cubic MOF-5 structure, b) the simplified connector; zinc atoms are the yellow spheres, oxygen atoms are in red, carbon in black, and hydrogen is the purple one. The three adsorption positions: metallic site, carboxylic site and cyclic site are visualized in S1, S2 and S3 squares respectively. 41
3.2 Energy as a function of the angle between the hydrogen molecule and the connector surface in the three adsorption sites 43
3.3 The first adsorption energy as a function of the adsorption site, orientation and adsorbate height in the connector of MOF-5 44
3.4 Calculated total and partial density of states for connector (a) without adsorption and (b) with adsorption of hydrogen molecule. 45
3.5 Density and transfer charge in this connector at plane (002) (a) without H_2 and (b) with H_2 adsorption 45
3.6 Sorption structures of two molecules of hydrogen on the S1-S3 site with: (a) S-S, (b) V-V, (c) H-H orientations of the two H_2 46
3.7 Variation of lattice parameters of connector as a function number of H_2 molecules adsorbed with desorption temperature for three orientations . . . 49
3.8 Corresponding energy profiles of H_2 migration in the $Zn_4O(C_8H_4O_4)_3$ system 51

4.1 Unit cell of the double connector of Zn-MOF-5 crystal. 53
4.2 Hydrogen molecule adsorption in appropriate adsorption sites and along three orientations: (a) horizontal, (b) vertical and (c) sloping orientation. . 55
4.3 The total density of states (T-DOS) and partial density of states (P-DOS) for unit cell-MOF-5 based Zn before (a) and after (b) adsorption of single H_2 56
4.4 Z-decorated primitive cells of M-MOF-5. Gray, red, black and blue atoms represent the metal M = Zn, Cd and Mg, oxygen, carbon and hydrogen respectively 57
4.5 Adsorption energies for the three orientations of the adsorbed H_2 at the unit cell of M-MOF-5:Z_2 systems, where Z = Li (a), Be (b) and Na (c). (a1), (b1) and (c1) present the analysis of the charge density between H_2 and Z 58
4.6 Adsorption energy as a function of adsorbed hydrogen molecules number at the cyclic site of M-MOF-5:Li_2 (a), M-MOF-5:Be_2 (b) and M-MOF-5:Na_2 (c) 60

5.1 Top view of a t-graphene monolayer (4 × 4 supercell) and the studied adsorption sites (denoted as H-1, H-2, B and T). 66

5.2 (a–d) Relative energy profile for the movement of the Sc atom along four different pathways. 67
5.3 Top and side views of isosurface charge densities of M@t-graphene: (a) 2Li, (b) 2Na, (c) 2K, (d) 2Ca and (e) 2Sc. Yellow and cyan indicate the accumulation and depletion of charge, respectively. The chosen isovalue was 0.0023 e/Å^3 68
5.4 Top and side views of the optimized structures of (a) 8Li@t-graphene, (b) 8Na@t-graphene, (c) 8K@t-graphene, (d) 8Ca@t-graphene, and (e) 8Sc@t-graphene. Black, green, orange, magenta, light blue and orchid balls represent C, Li, Na, K, Ca, and Sc atoms, respectively 69
5.5 The variation in the calculated binding energy of adsorbed nLi@t-B_4N_4 monolayer. 71
5.6 T-DOS (a) and P-DOS (b) of t-B_4N_4 monolayer, Li@t-B_4N_4, 2Li@t-B_4N_4 and 8Li@t-B_4N_4. (c) Top and side views of the isosurface charge density plot for the Li-functionalized t-B_4N_4 sheet. The isosurface level was set to 0.0039 e/Å^3. (d) MD simulations of the Li atoms functionalized systems. . 72
5.7 (a-c) Top and side views the hydrogen adsorption at different concentrations of Li on t-B_4N_4 system. 74
5.8 Average adsorption energy ($|E_{ads}|$) and hydrogen gravimetric density in t-boron nitride systems with different Li concentrations: (a) 1Li@t-B_4N_4, (b) 2Li@t-B_4N_4, and (c) 8Li@t-B_4N_4 75
5.9 $32H_2$/8Li@t-B_4N_4 system as obtained at the end of 5000 fs AIMD simulations at different values of temperatures: (a) 100 K; (b) 200 K; (c) 300 K. B, N and Li are represented by brown, purple and green balls respectively. Light pink and dark blue represent H_2 molecules with a distance from the Li atom less than and more than 2.5 Å, respectively. 75
5.10 Single hydrogen molecule migration pathways and the corresponding barrier energies on the systems: (a) t-B_4N_4 and (b) t-graphene. 76

6.1 (a) Top and side views of relaxed Be_2C monolayer, (b) the phonon spectra, (c) band structure, (d) total and partial density of state, and (e) variation of the total-energy and temperature between 0 and 20 ps during AIMD simulations at 298 K and the corresponding top and side snapshots of 2D Be_2C monolayer. 80
6.2 (a) Side and top views of different adsorption sites, (b) the calculated adsorption energies at the three most preferable sites as a function of the H_2-Be_2C distance. 82

6.3 DOS of single adsorption of a hydrogen molecule on pristine Be_2C in the (a) TBe1/2, (b) TC and (c) B adsorption sites. 83
6.4 The optimized structures of Li/Na/K/Mg-decorated Be_2C on both sides using the DFT/vdW function. 85
6.5 Top and side views of charge density differences for two-sided metal-decorated Be_2C monolayer at the most preferable adsorption site (TBe2) for: a) Li_2, b) Na_2, c) K_2, and d) Mg_2. The magenta and cyan areas stand for the charge gain and loss, respectively. The isosurfaces value are set to 0.0007 e/Å^3 86
6.6 DOS plots of 2M@Be_2C monolayer at most adsorption site (TBe2) for: (a) 2Li, (b) 2Na, (c) 2Mg and (d)2K. 87
6.7 AIMD simulations were run for 55 ps at 298 K in (6×6)-supercell; temperature and total energy of the beryllium carbide decorated with 8Li, 8K, 8Mg and 8Na. 88
6.8 Average/successive adsorption energies as a function of the number of adsorbed hydrogen molecules on (a) 2Li@Be_2C and (b) 2K@Be_2C. 89
6.9 Hydrogen storage capacities for $16H_2/2Li@Be_2C$ and $16H_2/2K@Be_2C$ compared to other different 2D-materials. 90
6.10 Images of AIMD simulations at 100 and 298 K of $64H_2$ desorbed 8Li@Be_2C and 8K@Be_2C systems as obtained at the end of 20 ps. 91

List of Tables

1.1 Properties of hydrogen isotopes form covalent atomic and diatomic molecules 5
1.2 Major U.S. Department of Energy (DOE) targets of on-board hydrogen storage for light-duty fuel cell vehicle. 8
1.3 Key characteristics of four types pressure vessels. 9
1.4 Hydrogen storage properties of some complex hydrides 14

3.1 Experimental data and calculated values for the structural parameters of MOF-5 41
3.2 Coupling energies of two molecules of hydrogen in the system 47
3.3 Calculated adsorption energies of nH_2 molecules on connector and average height between H_2 and substrate 48

4.1 The adsorption energy for the three sites and their orientations vs the hydrogen molecule distance at the unit cell surface: (a) Horizontal, (b) Vertical and (c) Sloping 55
4.2 The average adsorption energies (kcal/mol), the bond length of H_2 and the adatom distance between Z and H_2, as well as the storage capacities and desorption temperature in unit cell of M-MOF-5:Z_2. 61

5.1 Binding energies of M-decorated t-graphene system at the most preferable adsorption site together with those corresponding to the experimental cohesive energies of bulk metals. The optimized distances separating the M atom from substrate and Bader charge acquired by metals. 66
5.2 The results of the average adsorption energies of nH_2/mM@t-graphene, the H-H bond length, the distance between M and the hydrogen molecules H_2 and a hydrogen gravimetric density (wt.%) 69

6.1 The successive and average adsorption energy (E_s and E_{ads}) per H_2, the average distances between H_2 and Be_2C monolayer (D) and adsorbed hydrogen distance (H-H) 83

6.2 The calculated binding energy (E_b) of single Li/Na/K/Mg-decorated Be_2C system and Bader charge analysis of M atoms at TBe2, TC, B, H1, H2, and TBe1 sites. 84

List of abbreviations

US-DOE	United States Department of Energy
CNTs	Carbon nanotubes
IRMOFs	Isoreticular metal-organic frameworks
TPES	Total primary energy supply
2D	Two-dimensional
PV	Photovoltaics
ICE	Internal combustion engine
PEM	proton exchange membrane
BET	Brunauer-Emmett-Teller
DMFC	Direct Methanol Fuel Cell
PAFC	Phosphoric Acid Fuel Cell
AFC	Alkaline Fuel Cell
DMF	N,N'-dimethylformamide
MOF-5	Metal-organic framework-5
COFs	Covalent organic frameworks
BDC	Benzene DiCarboxylate
SWNT	Single wall structure
MWNT	Mmultiple wall structure
HCP	Hexagonal close-packed
DC	Direct current
RF	Radio frequency
UHV	Ultra-high vacuum
C_g	Gravimetric capacity
C_v	Volumetric capacity
wt.	Weight
T_{des}	Desorption Temperature
P	Equilibrium pressure
T	Temperature
R	The gas constant
E_a	Activation energy
K_β	Boltzmann constant
G	Free energy
ΔH	Heat of formation
ΔS	Entropy
E_{tot}	Energy total
DOS	Density of states
PDOS	Partial desnity of states
VB	Valence band
CB	Conduction band
TM	Transition metal

ab initio	First principal calculation
Ψ	Many-body wave function of electrons
$\hbar$	Planck's constant devised by 2π
e	Charge of the electron
m_e	Mass of the electron
M_I	Mass of the nucleus
Z_I	Charge of the nucleus
R_I	Position of the nuclei
r_i	Position of electron
T_e	Kinetic energies of the electrons
T_n	kinetic energies of the the nuclei
V_{int}	Internal potential
V_{ext}	External potential
V_{nn}	nucleus-nucleus potential
$n_H(z)$	Number of hydrogen in plan z
$n_S(z)$	Number of interstitial sites in plan z
$\rho(z)$	Density of Hydrogen in plan z
t_{eq}	Equilibrium time
t_f	Filling time
t_r	Relaxation time
V_{ee}	Electron electron potential
V_{KS}	Effective potential
$V_H(r)$	Hartree potential
$V_{xc}(r)$	Exchange-correlation potential
$\hat{H}$	Hamiltonian operator
Z	Partition function
LDA	Local density approximation
GGA	Generalized gradient approximation
PAW	Projector augmented wave
PBE	Perdew–Burke–Ernzerhof
MEP	Minimum energy path
NEB	Nudged elastic band
CDD	Charge density difference
vdW	Van der Waals
vdW-DF	van der Waals density functional
E_{ads}	Adsorption energy
E_{Cp}	Coupling energy
VESTA	Visualization for electronic and structural analysis
DFT	Density functional theory
AIMD	Ab initio molecular dynamics

Contents

Acknowledgment i

Abstract iii

Résumé iv

Résumé détaillé v

List of figures x

List of tables xii

List of abbreviations xiii

General Introduction 1

0.1 *Problem statement and motivation* . . . 1

0.2 *Thesis objectives* . . . 2

0.3 *Thesis layout* . . . 2

1 A comprehensive review of hydrogen storage: problems and targets 4

1.1 Introduction . . . 4

1.2 Hydrogen: energy carrier . . . 5

1.2.1 The unique properties of hydrogen . . . 5

1.2.2 Phase diagram . . . 6

1.3 Main storage techniques . . . 7

1.3.1 US-DOE technical targets for hydrogen storage . . . 7

1.3.2 Compressed H_2 storage . . . 9

1.3.3 Liquid/cryogenic H_2 storage . . . 10

1.3.4 Cryo-compressed H_2 storage . . . 10

1.3.5 Hydrogen in solid state materials . . . 11

1.3.5.1 Chemisorption storage . . . 12

1.3.5.2 Physisorption storage . . . 14

1.4 Theoretical aspects of hydrogen storage in MOFs . . . 16
1.4.1 A brief history of MOFs . . . 16
1.4.2 MOFs synthesis . . . 17
1.4.3 Size and morphology of MOF-5 crystal . . . 18
1.4.4 Isoreticular series . . . 19
1.4.5 IRMOFs for H_2 storage at low temperature . . . 20
1.5 2D-materials: Recent advances in hydrogen storage . . . 21
1.5.1 2D-Graphene . . . 22
1.5.2 2D-Graphane . . . 23
1.5.3 2D-Graphyne . . . 23
1.5.4 2D-t-graphene . . . 23
1.5.5 2D-Hexagonal boron nitride . . . 24
1.6 Summary . . . 24

2 Theoretical background: DFT and AIMD 26
2.1 Introduction . . . 26
2.2 Density Functional Theory (DFT) . . . 26
2.2.1 Born-Oppenheimer Approximation . . . 27
2.2.2 Hartree-Fock theory and the variational principle . . . 28
2.2.3 Hohenberg-Kohn theorem . . . 29
2.2.4 Kohn-Sham Formalism . . . 30
2.2.5 Exchange and Correlation Functionals . . . 31
2.2.5.1 Local Density Approximation (LDA) . . . 31
2.2.5.2 Generalized Gradient Approximation (GGA) . . . 32
2.2.6 Plane wave pseudopotential method . . . 32
2.2.6.1 Projector Augmented Waves: PAW . . . 34
2.2.7 Van der Waals Interactions . . . 35
2.3 Quantum Espresso . . . 35
2.4 Nudged Elastic Band . . . 36
2.5 Ab Initio Molecular Dynamics . . . 36

I Hydrogen Storage in Metal Organic Framework-5 (MOF-5) 38

3 Modeling hydrogen adsorption in the MOF-5 connector 39
3.1 Motivation . . . 39
3.2 Computational method . . . 39
3.3 Results and discussion . . . 40

3.3.1 Connector-MOF-5 geometry . . . 40
3.3.2 Connector stability: energy of formation and decomposition temperature . . . 41
3.3.3 Hydrogen adsorption for the connector . . . 42
3.3.3.1 The first hydrogen adsorption sites and their energy . . . 42
3.3.3.2 Adsorption energy for two hydrogen molecules . . . 46
3.3.3.3 High-coverage of H_2 adsorption and storage capacities . . . 47
3.3.3.4 Assessment of hydrogenation on connector properties . . . 48
3.3.3.5 H_2 molecular diffusion inside connector . . . 50
3.3.4 Summary and conclusion . . . 50

4 Lightweight metal decorating of M-MOF-5: Implications for hydrogen storage 52
4.1 Motivation . . . 52
4.2 Methodology and models . . . 53
4.3 Results and discussions . . . 54
4.3.1 Energy of formation considerations . . . 54
4.3.2 Adsorption of one hydrogen molecule in Zn-MOF-5 . . . 54
4.3.3 Nature of M@MOF-5-Z and H_2-Z interactions . . . 57
4.3.4 Gravimetric storage and desorption temperature . . . 60
4.4 Summary and conclusion . . . 61

II Hydrogen Storage in two-dimensional materials 62

5 2D-boron nitride for improved hydrogen storage applications 63
5.1 Motivation . . . 63
5.2 Computational methods and physical quantities . . . 64
5.3 Results and discussion . . . 65
5.3.1 Evaluating the stability of M on t-graphene . . . 65
5.3.2 Stability/Adsorption of Li on t-B_4N_4 monolayers . . . 70
5.3.3 Hydrogenation of nLi@t-B_4N_4 system . . . 73
5.3.4 Thermodynamical stability . . . 74
5.3.5 Single H_2 molecular diffusion . . . 76
5.4 Summary and conclusion . . . 77

6 Design of 2D-Be_2C as high capacity and reversible hydrogen storage media 78
6.1 Motivation . . . 78

6.2 Models and simulation details 79
6.3 Results and discussion 79
6.3.1 Crystalline and electronic properties of monolayer Be_2C 79
6.3.2 H_2 adsorption on pristine Be_2C monolayer 81
6.3.3 Metal decoration of Be_2C monolayer 84
6.3.4 H_2 adsorption on Li/K-decorated Be_2C monolayer 87
6.3.5 Thermodynamics of adsorption hydrogen molecules 91
6.4 Summary and conclusion 92

General Conclusion and Perspectives **93**

Appendices **116**

A List of publications **117**

B List of conferences and Seminars **119**

General Introduction

0.1 *Problem statement and motivation*

Actually, the modern society has shown great concern regarding the effects of hydrocarbons and the combustion of fossil fuels (oil, coal and natural gas) as the base of our energy economy, currently generating more than 80% of the global energy and releasing dangerous amounts of Carbon dioxide (up to 34 Mt per year, 40% higher than in 2010) and other greenhouse gases into the atmosphere. Many countries all around the world have encouraged initiatives to switch to a zero-emission energy-based economy by implementing new technologies and using alternative, cleaner and more sustainable sources such as solar, biomass, hydropower, wave power and wind. Hydrogen in this respect is an environmentally benign, safe and attractive medium; being among the most abundant element in the universe, with a high energy density (141.79 MJ/kg) and water as the major by product of its combustion. However, the bottleneck of these technologies lies principally on the development of safe and efficient methods for hydrogen storage. To encourage developments in this direction, the U.S. Department of Energy (DOE) has set the year 2025 as a target for hydrogen storage for 5.5 wt% in gravimetric capacity and 40 g/L in volumetric capacity, reversible hydrogen uptake/release at around ambient conditions, fast sorption kinetics, etc.

So far, a lot of efforts has been made to develop hydrogen storage systems that are safe, cost-effective, environmental-friendly and more importantly with high energy densities. Current technologies used for hydrogen storage include compression in gas cylinders, liquefaction in cryogenic tanks and adsorption/absorption into solid state materials. Compressed gas and cryogenic liquid state storage are not so suitable for practical applications due to the safety, high weight, size of the tank, evaporative losses and high maintenance and energy costs for liquefaction process. Consequently, the storage of hydrogen in solid state materials appears to be the most feasible solution since it is a safer and more convenient method compared to other technologies.

Solid storage represents a distinctive class of storage systems and has become the most promising approach for hydrogen storage. This type can be classified into two main

categories, namely physical adsorption and chemical absorption. In interstitial metal hydrides and complex hydrides, the hydrogen atoms are chemically bonded with metallic elements. In high specific area substrates, the hydrogen molecules can be adsorbed on the surface and pores via physisorption through the van der Waals interactions such as metal organic frameworks (MOFs) and two-dimensional materials (2D). These latter are potential materials for solid state hydrogen storage. Furthermore, a large number of studies have been carried out to provide new strategies to address the limitations of hydrogen storage systems. Among the most promising strategies reach that objective: reduction of size, alloying, morphology control, engineering strain, doping effect, and metal decoration (functionalization).

0.2 *Thesis objectives*

The principal purpose of this thesis is to deeply understand and develop new strategies to obtain metal organic frameworks (MOF-5) and 2D-materials with highly efficient in H_2 storage applications, which can be divided into two aspects namely **metal decoration** and **substitution**. The specific goals of this thesis are the following:

- Improve the thermodynamic stability of systems.
- Determine the hydrogen adsorption energies of metal-decorated systems with vdW corrections.
- Increase the gravimetric and volumetric storage capacities.
- Analyze the adsorption/desorption process of H_2 molecules using ab initio molecular dynamics.
- Figure out the underlying physical mechanisms and calculate the activation barriers of the hydrogen molecule.

0.3 *Thesis layout*

In this thesis, entitled "Theoretical investigations for hydrogen storage properties improvement in metal-organic frameworks and new bi-dimensional systems", a theoretical study of hydrogen storage properties of MOF-5 and 2D-materials is presented. These calculations are made using the density functional theory (DFT) and DFT based ab initio molecular dynamics (AIMD), to examine the kinetics and thermodynamics of (de)hydrogenation properties. The content of this study is divided in six chapters.

- The first chapter is devoted to the background knowledge of the hydrogen properties, reviewing the different types and methods of hydrogen storage focusing on the storage properties of metal organic frameworks and different 2D-materials.

- In the second chapter, a general description of the theoretical approaches used in this thesis is presented. Firstly, we will present a discussion on the use of density functional theory (DFT) with various approximations followed by a description of the concept of ab initio molecular dynamics (AIMD). Finally, we will discuss the implementation of the plane wave-pseudopotential method in the program package of Quantum ESPRESSO.

- In the third chapter, and for the first time for this material, we provide an examination of structural, electronic and thermodynamic properties of connector-MOF-5 by ab intio calculations. Also, an investigation of the adsorption mechanism of hydrogen molecule with different orientations in multiple adsorption sites. As for the kinetic aspect, the diffusion of H_2 was evaluated through the calculation of the activation energy.

- The fourth chapter reports the main results of this thesis, the functionalization of the unit cell of MOF-5 via light metal using van der Waals interaction. The effects of decoration by Li, Be and Na elements in the cyclic site on the adsorption energy, the capacity and the desorption temperature, with and without the substitution of Zn by Mg and Cd have been studied.

- In the fifth chapter, firstly, we study a t-graphene-like boron nitride monolayer ($t-B_4N_4$) as a new 2D material for molecular hydrogen storage. Secondly, the stability, electronic and storage properties of H_2 on metal-decorated $t-B_4N_4$ monolayer were investigated.

- In the last chapter, the effect of light metal (Li, Na, K and Mg) decoration on the stability of beryllium carbide (Be_2C) monolayer and its hydrogen adsorption/desorption is investigated by density functional theory (DFT) and DFT based AIMD.

Finally, the main conclusion gives a brief summary and criticism on our results. it includes a discussion of the impact of our findings to future research for the uses of MOF-5 and 2D materials as solid-state hydrogen storage application.

Chapter 1

A comprehensive review of hydrogen storage: problems and targets

1.1 Introduction

In our current way of life, energy is required for everything. Therefore, it is necessary to develop a sustainable edge technology for finding renewable energy produced from the primary sources such as solar, biomass, hydropower, wave power, wind and geothermal energy. Unfortunately, the share of the renewable energy sources is still small, and definitely not enough to satisfy the world's energy demand entirely. As a new energy vector, hydrogen is a field that has received a lot of interest due to its abundance, high power density and environmental friendliness [1, 2].

Hydrogen is an ideal clean carrier for mobile and stationary power sources as well as the most promising alternative to the combustion of finite, carbon-rich and environmental harmful fossil fuels, such as diesel and gasoline [3, 4]. The development of hydrogen energy systems involves four stages: production, distribution, storage and power conversion [5].

The methods of production, distribution and power conversion are the subject of much research, but the main obstacle is how to store hydrogen efficiently and safely under appropriate conditions [6].

The aim of this chapter is to view various aspects of hydrogen and its storage. An overview is given for the differents storage methods available today with respect to the progress made recently and problems still there. We will focus specifically on hydrogen storage in the solid state and more precisely in metal-organic framework-5 and 2D materials. We will describe the problems of this form of storage and solutions already proposed.

1.2 Hydrogen: energy carrier

1.2.1 The unique properties of hydrogen

Hydrogen was first discovered in 1671 by British scientist Robert Boyle. He was experimenting with different metals by dipping them in acid. When a pure metal is placed in acid, a type of reaction called a single-displacement reaction occurs. In 1766–1781, English physicist and chemist Henry Cavendish identified it as a chemical element. Subsequently, the French chemist Antoine Lavoisier gave the element its current name. Hydrogen (H) comes from the French word hydrogène, which was coined by Lavoisier by combining the Ancient Greek word húdōr (*'water'*) and gennáō (*'I bring forth'*), in other words 'water maker'. On Thanksgiving Day 1932, Harold Urey and his colleagues in the US detected a second, rarer, form of hydrogen. This has twice the mass of normal hydrogen, and they named it deuterium [7]. Two years later, an unstable isotope, tritium (3H), with an atomic weight of 3 was prepared by the group of by Ernest Rutherford in 1932 [8].
Hydrogen is the most abundant element in the universe (about 75% by mass) and the ninth most abundant element on Earth. As the lightest element, hydrogen is the first element in the periodic table of chemical elements with a single proton and electron. It is an odourless, flammable and colourless gas, and its solubility in water is very low.
Table 1.1 summarizes the properties of Hydrogen, deuterium and tritium with the following values of the main parameters [9, 10].

Property	**Hydrogen**	**Deuterium**	**Tritium**
		Atomic Hydrogen	
Symbol	H	D	T
Atomic mass (*amu*)	1.008	2.014	3.016
Nuclear stability	stable	stable	Radioctive
Ionisation energies (eV)	13.595	-	-
Electronegativity (Pauling)	2.1	-	-
		Molecular Hydrogen	
Symbol	H_2	D_2	T_2
Abundance (%)	99.985	0.0156	$\sim 10^{-15}$
Molecular mass (*amu*)	2.016	4.028	6.032
Bond distance (Angstrom)	0.7414	0.7414	0.7414
Critical Temperature (K)	33.19	38.35	40.60
Dissociation energy (kJ/mol)	435.9	443.4	446.9

Table 1.1: Properties of hydrogen isotopes form covalent atomic and diatomic molecules

1.2.2 Phase diagram

The hydrogen molecule H_2 can be found in different shapes depending on the temperature and the pressure, which are shown in the phase diagram below. At normal conditions, hydrogen is in gaseous state. It has the second lowest boiling point and melting points of all substances. Hydrogen liquefies below 20 K at atmospheric pressure. In these conditions, the liquid is 800 times denser than the gas at ambient temperature.
On the other hand, the first liquefaction hydrogen was obtained by Claude using a cycle divided into several steps [11]. The gas is firstly cooled from the ambient to 230 K by a group mechanical refrigeration then up to 80 K using a liquid nitrogen ex-changer. Hydrogen then undergoes compression-expansion cycles which further reduce temperature before being subjected to Joule-Thompson relaxation which leads to the liquefaction. Other processes can be envisaged such as the Brayton cycle which uses the liquid helium whose liquefaction temperature is lower than that of hydrogen or Magnetometer cycle refrigeration. The hydrogen is in solid state below its melting point of -259 °C and atmospheric pressure. The density of hydrogen at atmospheric pressure as a gas (at room temperature) is $0.09 kg.m^{-3}$, as a liquid (at -253°C) $70.8 kg.m^{-3}$ and as a solid (at -262°C) $70.6 kg.m^{-3}$. A phase diagram of hydrogen is shown in Figure 1.1, with a triple point at -259.1 °C and 0.07 bar and a critical point at -239.8 °C and 13 bars. At atmospheric pressure the boiling point is at -253 °C and the melting point at -259 °C. The boiling point of a fuel is a critical parameter since it defines the temperature to which it must be cooled in order to store and use it as a liquid [11, 12].

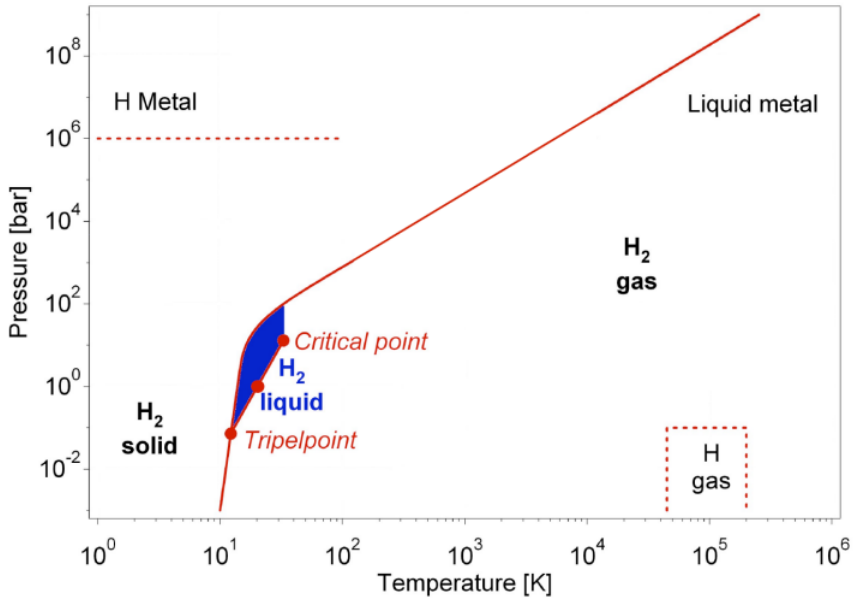


Figure 1.1: Simple phase diagram for hydrogen [12]

1.3 Main storage techniques

1.3.1 US-DOE technical targets for hydrogen storage

An increased research activity in the field of Hydrogen storage has been observed since the early 2000's, mainly due to the need for a practical storage method that could be used in various applications such as the residential, industrial, and more importantly, automotive sector. More than that, the density of hydrogen is very less, it must be stored efficiently. The issues that challenge the application of hydrogen vehicle imply to find a storage method or material that satisfies the following requirements [13, 14]:

- *High volumetric and gravimetric hydrogen density.*
- *The reversible hydrogen absorption/desorption at moderate temperatures in 60-120°C range to be compatible with the present generation of fuel cells.*
- *Favourable kinetics for hydrogen molecule absorption/desorption.*
- *Low cost and abundant resources*
- *Low toxicity, hazards and environmental impact.*

The United States Department of Energy (DOE) is in the research and development phase of achieving its targets for on-board applications. The aim is to provide onboard solutions, particularly for long-range passenger vehicles, reduced time for refueling, and ultimately, the overall performance of fuel cell vehicles.
The Table 1.2 summarizes the parameters and conditions, suggested by the US-DOE performance targets for on-board hydrogen storage systems in light-duty fuel cell vehicles which beginning from 2020 [15]. The ideal hydrogen tank should be able to store at least 2.2 $kWh.kg^{-1}$ and 1.7 $kWh.L^{-1}$, which is equivalent to gravimetric and volumetric capacity of 6.5% and 50 $g.L^{-1}$ respectively, at a cost of \$266/kgH_2 stored (\$8/kWh). The delivery temperature should be close to the room temperature (-40 to -85°C) and the filling time should be not more than 5 minutes.

Storage parameter	Unit	2020	2025	Ultimate
Storage capacities [15]				
Gravimetric capacity	$wt\%$	4.5%	5.5%	6.5%
Volumetric capacity	$g/L.H_2$	30	40	50
Storage system cost	\$/kWh net	10	9	8
(and fuel cost)	\$/$kg.H_2$	333	300	266
Durability/Operability				
Min/Max delivery temperature	$°C$	-40/85	-40/85	-40/85
Cycle life (1/4 tank to full)	cycles	1500	1500	1500
Min. delivery pressure from tank	bar	5	5	5
Max delivery pressure from tank	bar	12	12	12
Onboard efficiency	%	90 %	90 %	90 %
Charging/Discharging rate				
System fill time (for $4-10kg$)	min	3-5	3-5	3-5
Min full flow rate	$((g/s)/kW)$	0.02	0.02	0.02
Average flow rate	$((g/s)/kW)$	0.004	0.004	0.004
Fuel purity (H_2 from storage)	$\%H_2$	Meet or exceed applicable standards		

Table 1.2: Major U.S. Department of Energy (DOE) targets of on-board hydrogen storage for light-duty fuel cell vehicle.

Depending on these requirements, hydrogen can be stored in 4 main ways namely: **compressed gas**, **cryogenic liquid**, **cryo-compressed storage** and **solid-state compounds** which are at the focus of current scientific interests (Figure 1.2(left)). In contrast, Figure 1.2(right) depicts hydrogen storage systems with different densities, clearly showing that the complex hydride and metal storage materials have higher volumetric densities than other systems. Besides storage capacities, the methods (conventional or physical storage) also have other useful hydrogen storage properties which will be highlighted in next sections.

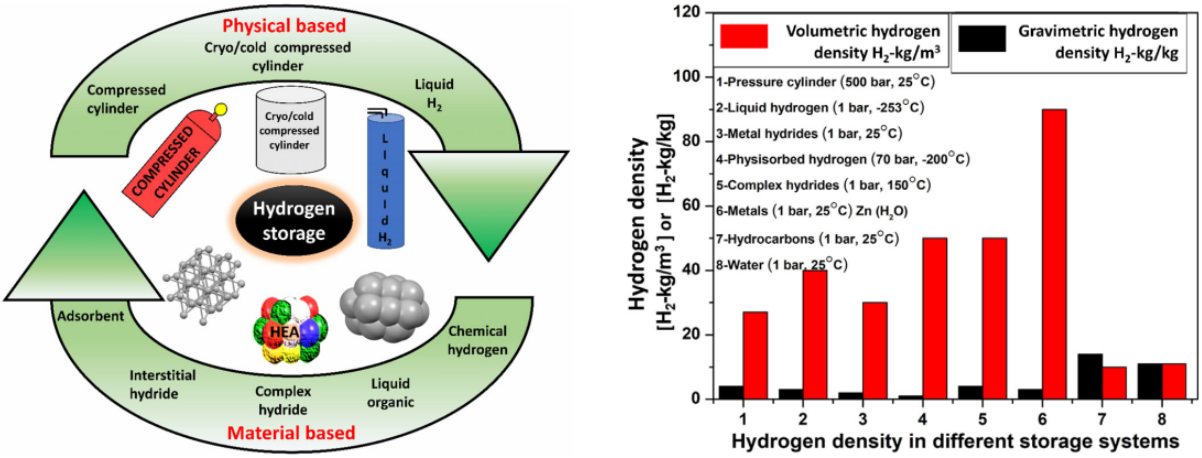


Figure 1.2: (left) Several hydrogen storage methods. (right) Comparison of gravimetric/volumetric density of different hydrogen technologies [4].

1.3.2 Compressed H_2 storage

High pressure gas cylinders are the most common storage systems used in today's world. In fact, due to the very low density of hydrogen ($0.089 kg.m^{-3}$) its storage requires high pressure between 350 and 700 bar at room temperature [16, 17]. A high compressive cost and a safety factor for storage medium are some of the main challenges for such storage technology. Currently, the compressed hydrogen can be stored in four different types of pressures vessel presented in Figure 1.3 [18, 19]. Metal pressure vessel is mostly used for industrial applications with pressure of 200-300 bar known as type (I). This type has a limitation in storage efficiency, it can only able to store about 1wt.% of H_2. Type (II) where the cylindrical part of the vessel is a thick composite tank wrapped with fiber resin. Type (III) is a composite vessel consisting of a metal shell to contain hydrogen and a continuous resin impregnated fiber envelope for mechanical holding. Type (IV) reservoir is a polymeric fully wrapped with fiber resin. It is the lightest storage vessel with a highest pressure resistance.

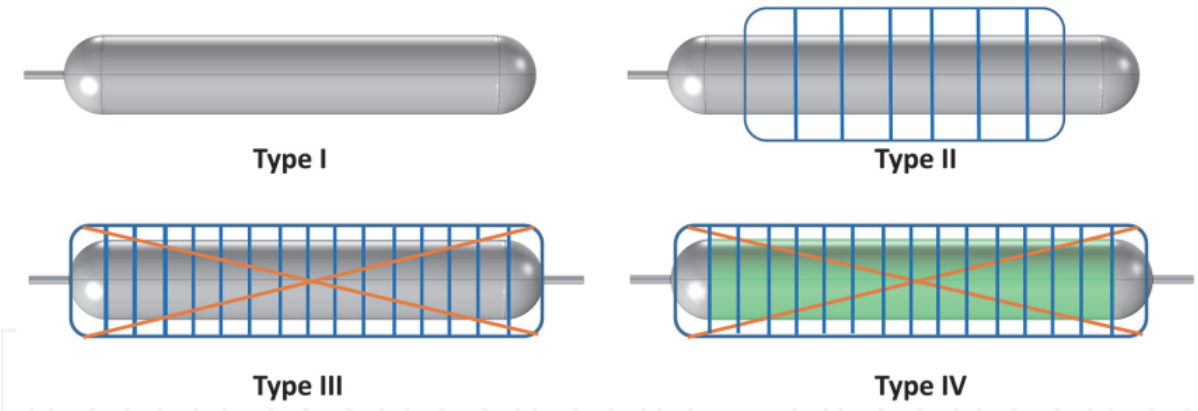


Figure 1.3: Vessel types of hydrogen compressed storage [19].

For industrial applications, Type (I) is the cost effective tank but their weight is the heaviest. Type (IV) storage tank can hold up to 700 bars with the lightest weight but the cost performance is two folds of Type (I). The table 1.3 presents the main characteristics of each tank type [20].

Type	**Maximum Pressure** (bar)	**Cost performance** ($/liter)	**Weight performance** (lb/liter)
(I)	200	5	3.0
(II)	263	5.5	0.9
(III) and (IV)	300 to 700	11	0.75 to 1

Table 1.3: Key characteristics of four types pressure vessels.

The compressed gas storage option can be considered as a promising hydrogen storage

technology if some drawbacks are achieved. These are low densities [21, 22], high operating pressures, hydrogen embrittlement, necessity for strict pressure controls and safety in densely populated areas. Therefore, advances in significantly increasing the hydrogen density and decreasing operating pressures within a tank or finding other ways to provide safety will turn into big milestones in compressed hydrogen gas storage.

1.3.3 Liquid/cryogenic H_2 storage

Space industry has used hydrogen as a fuel in liquid form for several years [23]. Hydrogen can be stored as a liquid at -253 °C (20 K) in super insulated vacuum tanks at ambient pressure with a high volumetric density of 71 $g.L^{-1}$ (see Figure 1.4). It also has the best and highest energy-to-weight ratio of all the fuels. However, liquid hydrogen has an extremely low boiling temperature of 20 K, which is actually the second lowest boiling temperature in nature after helium (He) [24]. Consequently, it requires very sophisticated insulation techniques to keep hydrogen in liquid form. Because of this problem, combined with high price of the cryogenic vessels, this technology has applications limited to the space programs, stationary storage and short-term onboard storing [23, 25, 26]. Further development of insulation technology and cooling systems may open this technology for wider mobile applications.

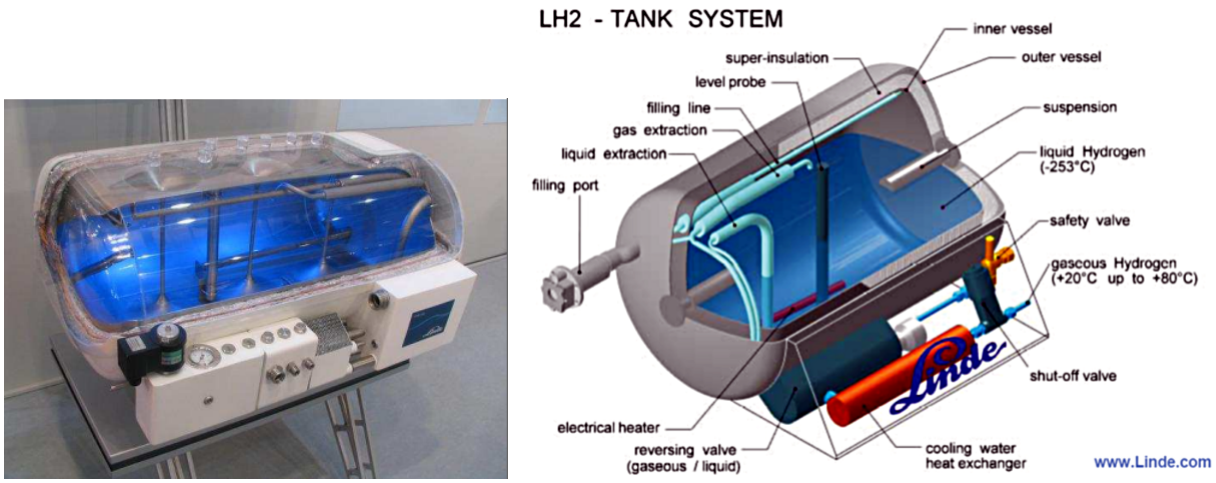


Figure 1.4: Schematic of a cryogenic tank for liquid H_2 storage.

1.3.4 Cryo-compressed H_2 storage

Cryo-compressed storage method was introduced to overcome the disadvantages of compressed gaseous hydrogen and cryogenic hydrogen storage by combining their main

characteristics. This method is used to minimize the boil-off rate of hydrogen and at the same time, maintain a high energy density. Hydrogen is stored in an insulated tank that can accept cryogenic temperatures and high pressure (at least 300 bar) at ambient temperature as presented in Figure 1.5 [27]. More compact and lighter cryogenic pressure vessels, therefore, provide better safety advantages than compressed hydrogen vessels. However, the persistent boil-off of hydrogen and too much energy required for liquefaction restrict the potential use of liquid hydrogen storage systems to applications that require high energy density as well as uses where hydrogen cost does not matter, and its consumption is within a short time, examples include air and space and automotive applications [19, 28, 29].

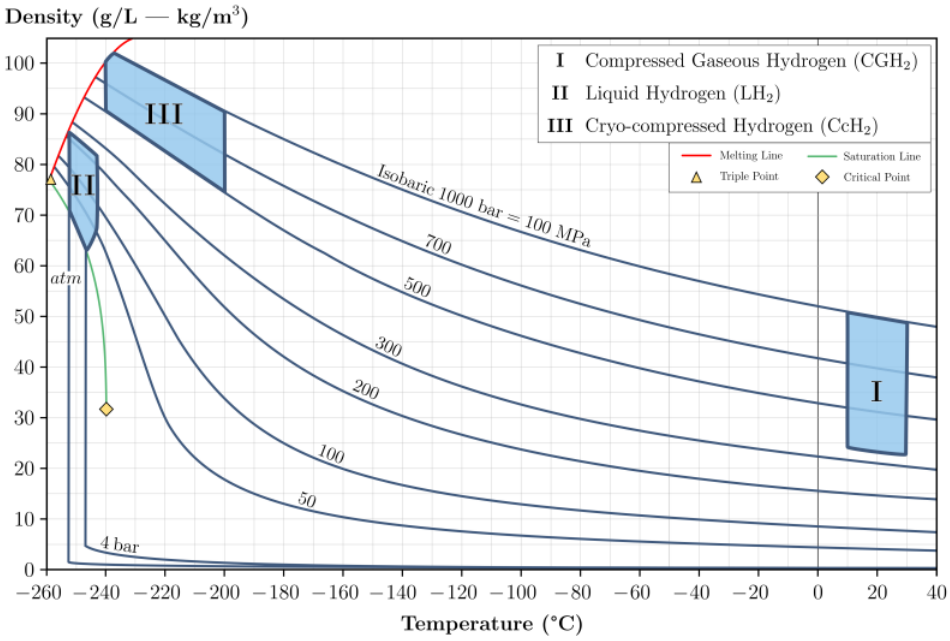


Figure 1.5: Hydrogen storage density under different pressure and temperature conditions.

1.3.5 Hydrogen in solid state materials

Conventional systems such as high pressure compressed gas storage or low temperature cryogenic gas storage present problems as they operate under extreme and unsafe conditions [30]. As a result, a variety of storage methods have been proposed and absobtion/adsorption of hydrogen on solid-state materials has received intense research focus [31]. Hydrogen storage materials could be divided into two categories depending on the mechanism of hydrogen sorption: materials where adsorption is due to chemical storage (chemisorption) or due to physical storage (physisorption) under diverse conditions of pressure and temperature.

1.3.5.1 Chemisorption storage

The name "*chemisorption*" is usually used for description of the group of materials with hydrogen bonded by strong covalent bonds. Chemisorption implies breaking bonds (hydrogen molecule dissociation) and making new ones with the substrate. This implies high energetic cost since chemisorption of molecular hydrogen presents high barriers around 1.5 eV. By suitable control of the thermodynamic conditions of gas pressure and temperature within the reservoir, it is possible to manage respectively the absorption and desorption of hydrogen. Lowering the cost, weight, and operating temperature,enhancing the charge-discharge kinetics and controlling formation of unwanted gases during desorption are the main remaining challenges facing the chemical sorption materials [32, 33]. These materials can be further categorized into two main groups depending on the type of bond with hydrogen: interstitial metal hydrides and complex hydrides.

a) Metal hydrides

Metal hydrides store atomic H inside their crystal structure by the mechanism of absorption. Molecular H_2 is attached onto the surface of the metal, where it dissociates into atomic H and then diffuses into the bulk of the metal by occupying interstitial sites of the crystal lattice [34]. This type exist within metals or alloys, they have physical properties which make them suitable for hydrogen storage such as; low absorption, high volumetric energy density, oxidation resistivity and some of them benefits of good reversibility [35]. The drawback of such storage method can be related to the cost of metal hydrides, metal hydrides being heavy and the reaction kinetic to release hydrogen is slow [36].
Depending on the thermodynamics of the reaction, different temperatures apply to different metal hydrides. A typical reversible interaction between metal/alloy and hydrogen can be written as:

$$M + \frac{x}{2} H_2 \longleftrightarrow MH_x + \Delta H \tag{1.1}$$

where M is a metal, an intermetallic alloy, or a solid solution; x is the mass concentration of hydrogen, MH_x is the formed hydride and ΔH is the heat of reaction. A simplified model of hydrogen storage in a metal hydride is given in Figure 1.6.

Nowadays, research is still ongoing to synthesize metal hydrides which will fulfill the targets for hydrogen storage systems set by the *DoE* for on-board vehicular applications, a brief summary was given in Table 1.2.
At present, the main alloying materials for metal hydrides are:

- Intermetallic compounds (AB_5, AB_2, AB, and A_2B), which has a hydrogen storage capacity of 1.5, 2.0, 1.8 and 3.0$wt.\%$, respectively. Solid solution alloys are also available such as vanadium-based solid solution alloys and Mg-based alloys, which

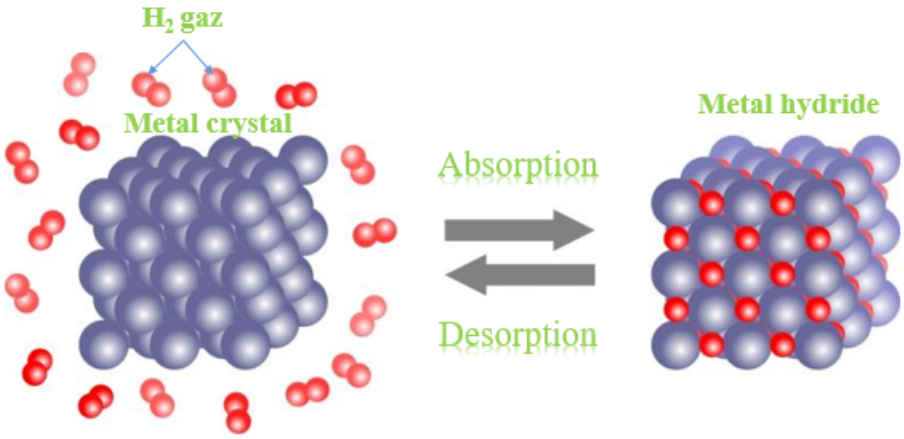


Figure 1.6: Chemisorption of metal crystal and hydrogen storage.

have a hydrogen storage capacity of approximately 2 and $5wt.\%$ respectively [37].

- Metallic hydrides (also called element hydrides or metal hydrides) composed of lightweight elements such lithium, boron, nitrogen, magnesium and aluminium have shown great potential for use as hydrogen storage materials [38].
- Complex hydrides which are the only group of metal hydrides having high volumetric and gravimetric hydrogen storage densities [39]. Some features of this type will be given in the next paragraph.

b) Complex hydrides

The main disadvantage of conventional metal hydrides such as intermetallic hydrides is their low H_2 storage capacities [40]. Complex hydrides composed of light elements such as lithium, bor and sodium have gained significance as hydrogen storage materials since conventional metal hydrides are mostly composed of heavy elements. Lightweight complex hydrides emerge as potential candidates for hydrogen storage applications due to their high hydrogen storage capacities (up to $18wt.\%H_2$ for $LiBH_4$), high hydrogen storage densities, as well as mild dehydrogenation pressures and temperatures [41]. The heat of formation, gravimetric storage capacity and dehydrogenation temperatures for some selected complex hydrides are shown in table 1.4.
Complex hydrides such as alanates and borohydrides are able to bond four hydrogen atoms with an alkali metal, ionic compound or partially covalent compound [47]. Even though complex hydrides have high energy densities, they are difficult to handle safely and they may decompose according the a cascade of reaction into highly stable elements, which are very challenging to refuel with hydrogen on board a motor vehicle [48].
However, these problems can be compensated to a certain extent by thermodynamic

Compound [42, 43, 44, 45, 46]	Heat of formation ($kJmol^{-1}.H_2$)	Desorption temperature T_D (°C)	Gravimetry (wt.%)
$LiBH_4$	-194	380	18.4
$NaBH_4$	-191	400	10.6
KBH_4	-229	500	7.4
$LiAlH_4$	-2	125	9.5
$NaAlH_4$	37	210	7.4
$KAlH_4$	-	270	5.7
$Mg(AlH_4)_2$	-18	140-200	9.3
$Ca(BH_4)_2$	-	320	11.5

Table 1.4: Hydrogen storage properties of some complex hydrides

destabilization, which involves the addition of a new element into the system by means of cation or anion substitution, or the addition of reactive hydride composites. Nano confinement or the addition of catalysts can also be used for thermodynamic destabilization [49].

1.3.5.2 Physisorption storage

The physisorption mechanism suggests adsoption of molecular hydrogen on a surface via relatively weak van der Waals bonding. Several characteristic features of physisorption can be noted. The adsorption process is fast, i.e. the saturation is achieved within minutes after hydrogen pressure is stabilized, and fully reversible. Hydrogen is released when pressure is lowered and is adsorbed when pressure is increased again. Surface area is the main factor which controls hydrogen adsorption capacity of the material. The more surface area which is accessible for sorbate molecules the more sorbate molecules will be adsorbed on the sorbent surface. The materials included in this category are:

a) Carbon materials

Hydrogen gets adsorbed on the surface of carbon through Van der Waals bonding (6 kJ/mol). There are many unique carbon structures with high surface area such as carbon foam, carbon nanotubes, carbon aero gels and activated carbon which possess a very low volumetric density while fullerenes require a very high surface area to achieve sufficiently high packing density, Figure 1.7.

b) Zeolites

Zeolites are crystalline materials composed of SiO_4 or AlO_4 building blocks (see Figure 1.8(a)). They contain an intra-crystalline system of channels and cages which

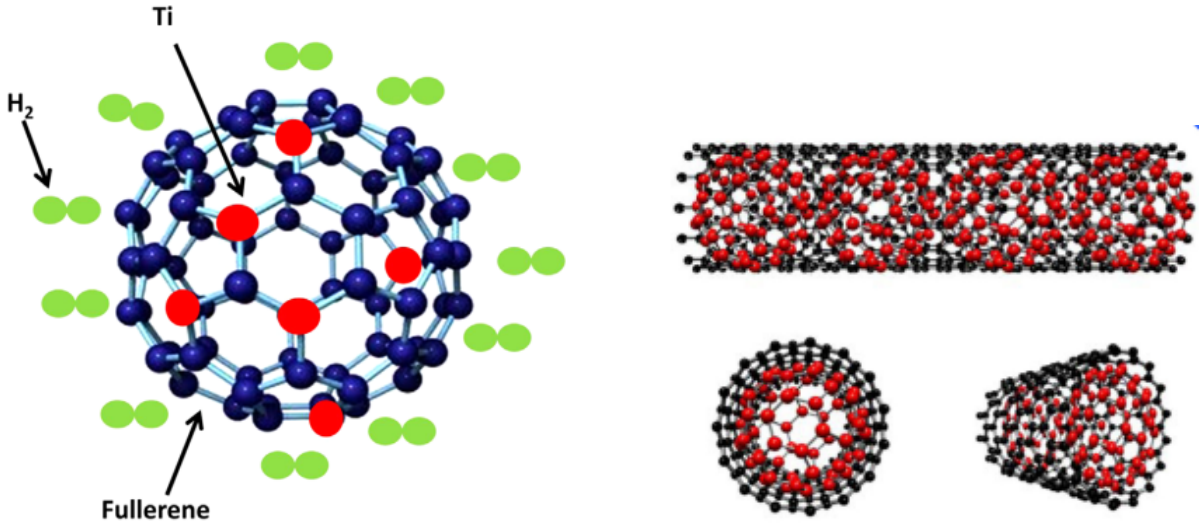


Figure 1.7: Structure of various carbon materials: fullerenes (left) and nanotubes (right).

can trap guest H_2 molecules. The adsorption capacity of system at 77 K is typically below 2 wt%. A theoretical capacity of 2.86 wt% has been suggested as being an intrinsic geometric constraint of zeolites [50]. Due to this low gravimetric density, zeolites are not typically considered feasible hydrogen storage materials. Isosteric heats on the order of 6-7 kJ/mol are typical for hydrogen zeolite systems [51].

c) Covalent Organic Frameworks (COFs)

Covalent organic frameworks are a class of crystalline porous organic polymers with permanent porosity and highly ordered structures, and without the disadvantages of the presence of heavy elements [52]. Their molecular frameworks are constructed of light atoms (C, O, B and H) that lower the relative weight of the structure (see Figure 1.8(b)). As one of the best COFs for hydrogen storage COF-8 exhibits an excess hydrogen uptake of 10wt.% at 77K and 100bar [53]. Moreover, the reported gravimetric uptake for COF-108 reached the value of 21wt% at 77K and 100 bar conditions and the very promising value of 4.5wt% in room temperature and 100 bar conditions [54]. These values are significantly higher than the highest values reported in MOFs (7wt.% in MOF-177), although the pressure employed is quite high at 77K [55].

d) Metal Organic Frameworks (MOFs)

Metal-Organic Frameworks(MOFs) are crystalline compounds consisting of metal ions or metal oxide clusters, coordinated with rigid organic molecules, forming regular 3D structures. MOFs were developed as a novel structure for getting a better hydrogen storage capacity via physisorption [56, 57]. These frameworks have higher surface areas,

more porosity, uniform size of pores, and distinct hydrogen cell location (see Figure 1.8(c)). Some of the rated networks (MOF-n=1-7, 8, 10, 12, 14, and 16) have been highlighted and the MOF-5 compounds were among the first to be studied for hydrogen storage (4.5 wt% at 77 K and 1 atm) [56]. Some features of these metal-organic frameworks will be given in next section.

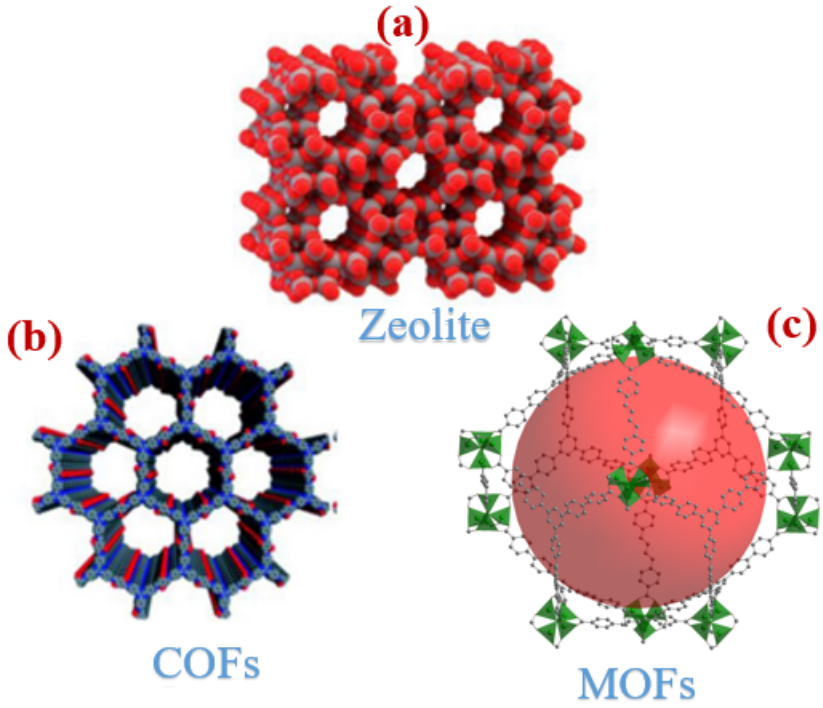


Figure 1.8: Structures of microporous materials: (a) zeolites, (b) covalent organic frameworks, and (c) metal organic frameworks.

1.4 Theoretical aspects of hydrogen storage in MOFs

1.4.1 A brief history of MOFs

One of the first reports of MOFs was in 1965 when Tomic formed *"coordination polymers"* via solvothermal synthesis [58]. They found that the thermal stability of the fabricated structures depends on the metal used, for example, metal ions less-able to change their ionic valency form more stable structures. There has been limited research in the decades following this preliminary work, largely due to difficulties associated with the synthesis of MOFs.

It was over 25 years since the work of Tomic that MOF research rapidly accelerated following pioneering work from Robson and co-workers [59]. The use of the term *"Metal-Organic Framework"* dates back to 1995 [60], and the systematic study of these materials

as a class in its own right misdates in the early 2000 years. By Yaghi et *al* In 1999, they used the molecular building block approach to synthesise one of the first MOFs to display permanent porosity, MOF-5 [61]. Their work showed that MOF-5 was highly porous after desolvation, with a pore volume of $0.6cm^3/cm^3$, and that MOF-5 undergoes reversible adsorption desorption, hence exhibits permanent porosity. Since, the number of publications on the synthesis, characterization and study of hybrid organic-inorganic materials has grown exponentially. So far, more than 90000 different MOF structures have been reported and the number grows daily [62].

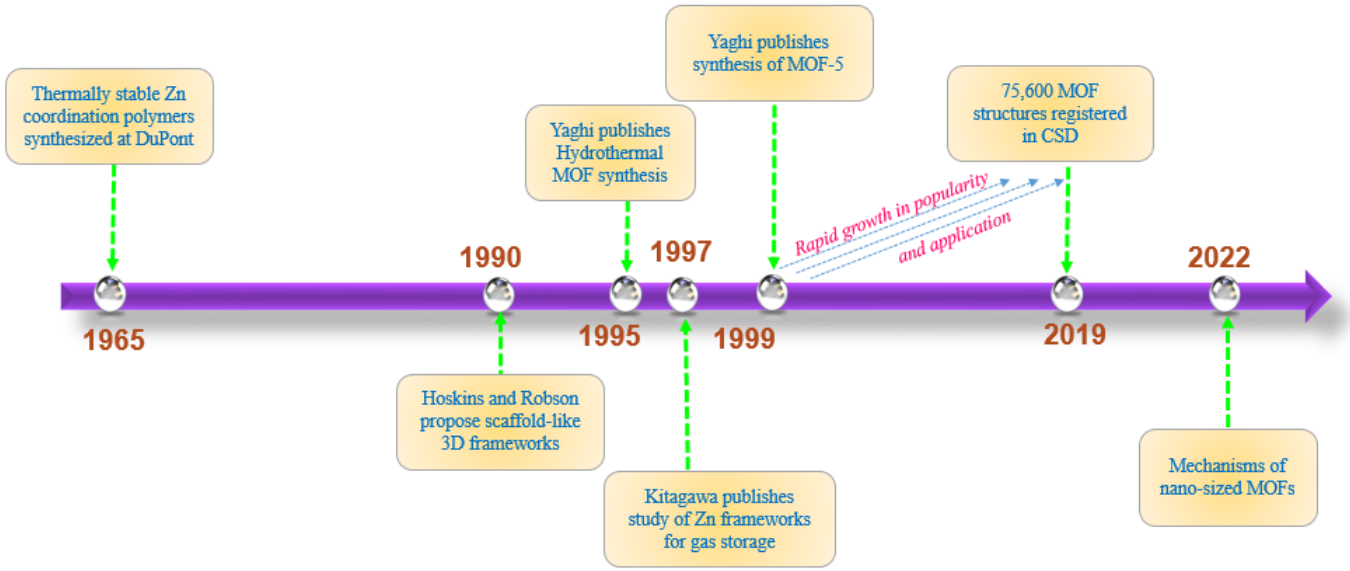


Figure 1.9: Historical developments in MOF synthesis.

1.4.2 MOFs synthesis

Energy is necessary for the breaking or formation of the bonds, and this process is valid for MOFs synthesis also because it includes the bonding of organic linker and metal ions. In general, -273.15-273.15 °C is the temperature range used for the synthesis of MOFs . Various types of synthesis methods were reported in the literature [63] such as classical hydro(solvo)thermal synthesis, microwave heating , diffusion, Conventional solution method, electrochemical synthesis, and more recently Iono-thermal process. However, conventional hydrothermal or solvothermal heating of organic, inorganic precursors dissolved in a suitable solvent system in closed vessels under autogeneous conditions was well studied for major MOF synthesis, as shown in Figure 1.10.
MOF-5 or IRMOF-1 consists of octahedral Zn_4O clusters linked by ditopic linear BDC with a chemical formula of $Zn_4O(BDC)_3 \cdot$ guest molecules using a diffusion synthesis method [61] at low yield. Diffusion of triethylamine into a solution of zinc nitrate and

H_2BDC in DMF/chlorobenzene resulted in the deprotonation of H_2BDC and reaction with Zn^{2+} ions. It is now replaced with a high-yield solvothermal method: an DEF (N,N-diethylformamide) solution mixture of $Zn(NO_3)_2 \cdot 4H_2O$ and the H_2BDC are heated at 105 °C in a closed vessel to give crystalline MOF-5 [64].

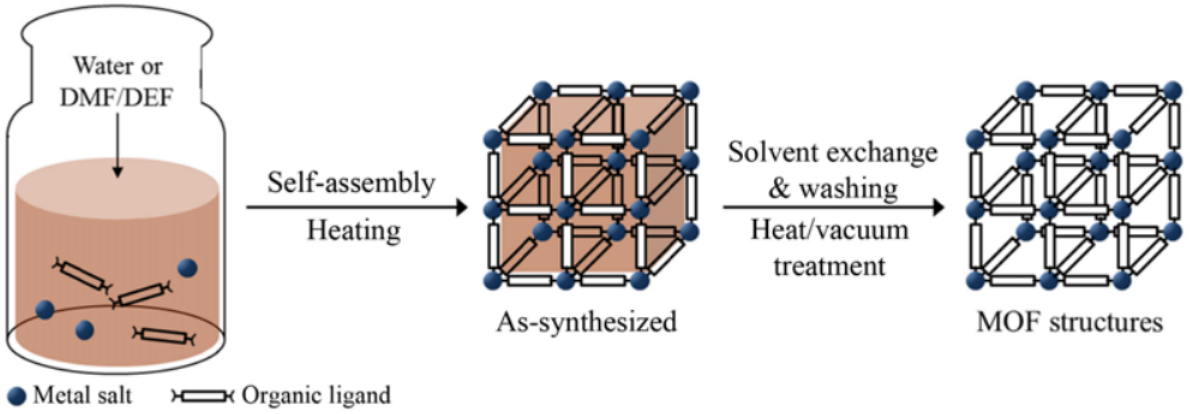


Figure 1.10: Conventional solvothermal synthesis of MOF structures

1.4.3 Size and morphology of MOF-5 crystal

One of the most widely researched MOFs compounds is MOF-5 (Figure 1.11), which has high gas selectivity and capacity [65]. MOF-5, namely $Zn_4O(BDC)_3$, is a three-dimensional cubic porous framework with $(Zn_4O)^{6+}$ clusters linked together through 1,4-benzenedicarboxylate BDC^{2-} ligands [66]. The large size (8.9 Å) and high connectivity of the SBUs in combination with the long BDC linker (6.9 Å) provide for an open porous structure with alternating inter-connected pores of 15.1 and 11.0 Å in diameter, and a pore aperture of 8.0 Å. These large cavities make up 61% of the unit cell volume and are filled with solvent molecules (DMF) in the as-synthesized material. One of the most striking features of the MOF-5 structure is that the pores have no walls. This provides for an unprecedented openness of the structure that allows guest molecules to move with great facility without clogging the pores. The different types of stability relevant to this MOF-5 below:

- **Chemical stability** is the ability of a given material to withstand chemical treatment without any significant change in its structure.
- **Thermal stability** is a very important property for practical applications. Nevertheless, most of the thermal stability of the crystal MOF-5 has been reported, which was about 350°C, less than 450°C [67].

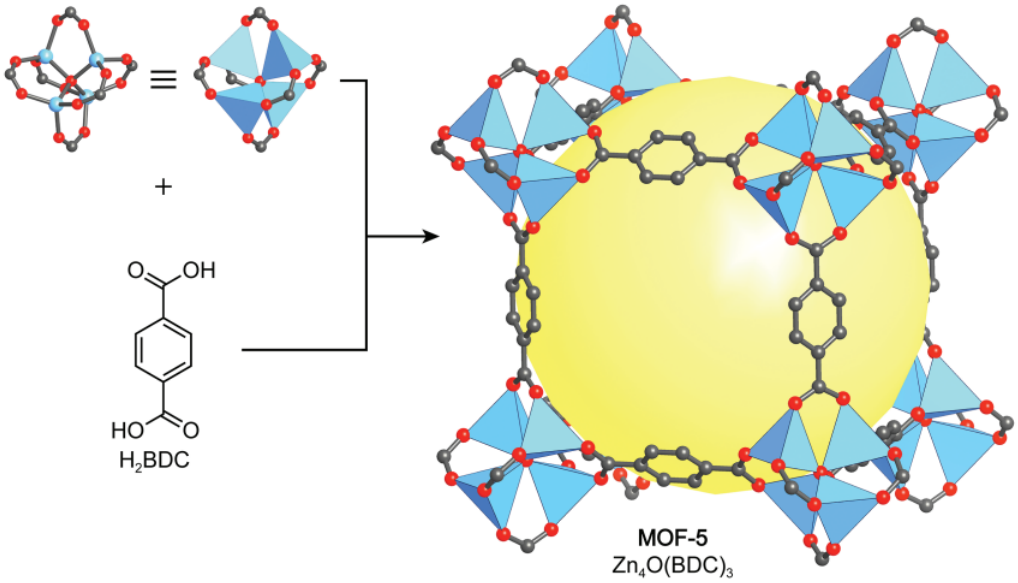


Figure 1.11: Crystal structure of MOF-5 (C, black; Zn, blue; O, red; gust molecule, yellow sphere and all H atoms have been omitted for clarity) [65].

- **Mechanical stability** is the ability of a given material to withstand external forces. Methods to determine the mechanical stability of MOFs are similar to those used in materials science such as pressurization, nano-indentation or determination of the tensile strength to name a few [68].
- **Architectural stability** is the ability of a framework compound to retain its structural integrity in the absence of guest molecules. This can be demonstrated by evacuation the solvent from the pores of the MOF and subsequent confirmation of its crystal structure and porosity.

1.4.4 Isoreticular series

To address the defects of microporous MOFs, several efforts have been made to create mesopores when designing new MOFs. In 2002, Yaghi and co-workers presented their results of a series of isoreticular MOF-structures (IRMOFs), based on the network topology of MOF-5 [61]. Cubic zinc-terephthalate framework structures linked by 16 different organic molecules varying in length and functionality are demonstrated in Figure 1.12 [64, 69]. The pore size of IRMOF-16 is as large as 2.88 nm. Unfortunately, the target products with extended linear bonds are mostly thermodynamically instable and tend to form an interpenetrated structure, which in turn reduces the pore sizes of the obtained MOFs.

Pore size modulation, a major determinant of affinity, is one of several ways to increase the adsorption affinity of MOFs, despite the incompatibility of extremely small pore sizes

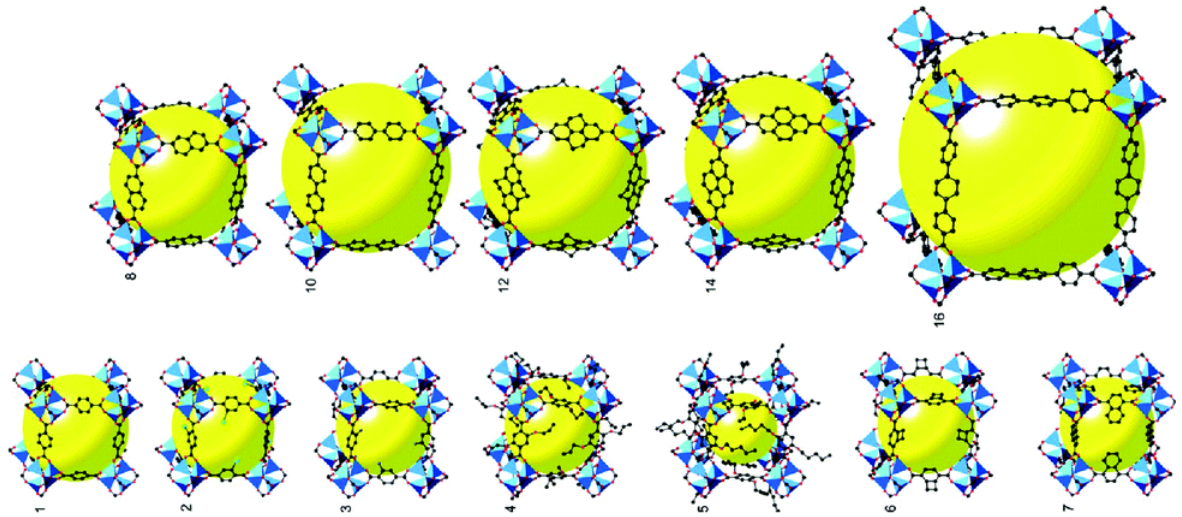


Figure 1.12: Series of isoreticular metal-organic frameworks (IRMOFs-n with n=1-8, 10, 12, 14, 16) based on MOF-5. Yellow spheres indicate the location of the cavities in the cubic cage.

with extensive surface areas in practical use. Application of unsaturated metal to the pore surfaces can significantly increase physical adsorption, but framework density is subsequently affected by such an increase in metal concentration.

1.4.5 IRMOFs for H_2 storage at low temperature

The critical factors that determine hydrogen adsorption and desorption are the large specific surface area of the adsorbents and the interaction between hydrogen and the solid surface. In the context of H_2 Storage, MOF-5 with a surface area of 3534 showed 4.5 wt% H_2 uptake at 78 K and 0.8 bar and it stored 1 wt% of H_2 at 298 K and 20 bar as schown Figure 1.13 (left) [56]. Although the H_2 uptake amount for MOF-5 at 77 K was reported again later as 1.3014 wt% at 1.01 bar (1 atm)[70] and 1.5115 wt% at 1.13 bar [71], the result was still exciting enough to motivate many researchers to study this topic.
In Figure 1.13(right), shows the trend of increasing gravimetric storage capacity with increasing Brunauer-Emmett-Teller (BET) surface area for MOFs. In general, the pore size is proportional to the specific surface area. Therefore, in order to increase the H_2 uptake capacities at 77 K, higher specific surface area and higher pore volume should be created in the MOF. For instance, MOF-200 and MOF-210 have the highest hydrogen excess uptake of 7,4 and 8.6 wt.%, respectively, ever reported for physisorption. The record high values of the total uptake which takes into account the amount of hydrogen pressurized inside voids of the MOF's structure was 17.6wt.% at 77K and 80bar [72]. Also, the excess gravimetric capacity of MOF-177 was found to be 11 wt.% of H_2, and 19.67wt.% in terms of absolute adsorption at 77K and 100 bar of hydrogen pressure [73].

So far, there are several proposed ideas on how to improve the strength of hydrogen

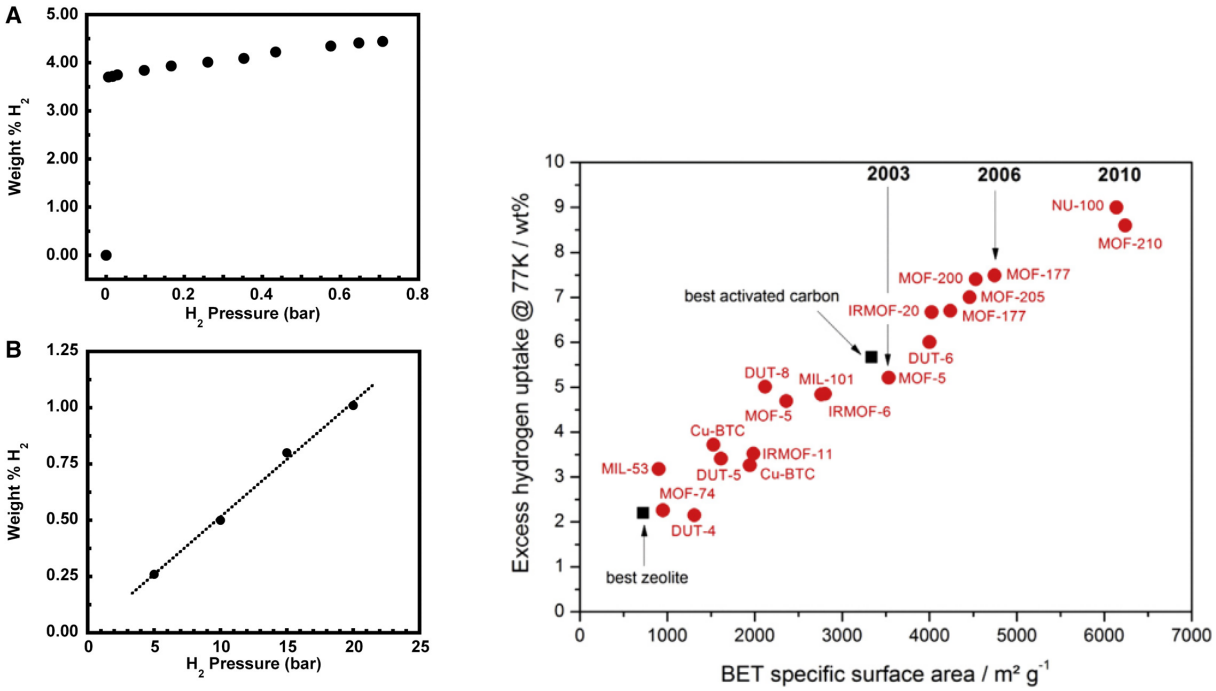


Figure 1.13: (left) Hydrogen gas sorption isotherm for MOF-5 at (A) 78K and (B) 298 K. (right) A plot between excess gravimetric H_2 uptake, measured at 77 K and 2 MPa or above, for various MOFs.

interaction with MOFs, such as reducing pore size [74], introducing unsaturated metal adsorption sites [75, 76], doping MOFs with alkali metals[77], changing organic ligands and metal clusters [78], and using the hydrogen spillover effect [79].

1.5 2D-materials: Recent advances in hydrogen storage

In recent years, a large number of two-dimensional materials (2D) has been isolated and started to be studied [80, 81, 82], greatly expanding possible novel phenomena to be explored and options for selecting the most suitable material for a given applications (Figure 1.14). The 2D materials are being investigated more interestingly due to their outstanding properties (structural diversity and large specific surface area), including the electrical, physicochemical, optical, micromechanical, and thermoelectric characteristics. Thus, offering a desirable pathway to integrate them into different applications [83, 84, 85, 86]. 2D-materials structures show profound efficiency in molecular hydrogen storage by providing large surface area and porosity, and thus avail additional adsorption sites to anchor or incorporate molecular hydrogen [87]. Nanoconfinement in 2D materials

and thin films provides a proficient approach to tune the interfacial properties of materials in hydrogen storage.

In these contexts, 2D material-based H_2 storage seems to be the most sustainable option

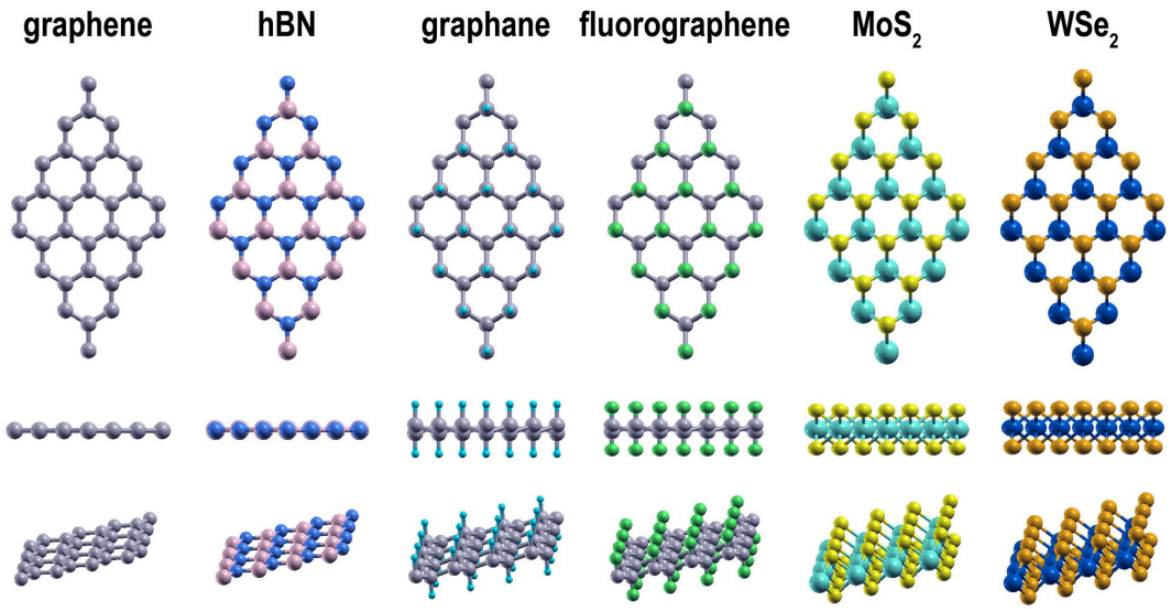


Figure 1.14: Examples of several 2D-materials, each containing different chemical elements and atomic configurations.

provided a suitable material is available, which meets the criteria proposed by US-DoE. The most important classes of two-dimensional materials (e.g. Graphene, Graphane, Graphyne, t-graphene, and Hexagonal boron nitride) employed for hydrogen storage applications are examined below.

1.5.1 2D-Graphene

As the first realized 2D material, graphene is composed of carbon atoms (C) in a hexagonal honeycomb lattice. Each atom has a covalent bond with three adjacent atoms and contributes with one electron to the common electronic system that dominates the optical and electrical properties of graphene. It is one of the systems with large specific surface area and an apt material with great potential for hydrogen storage being lightweight, chemically inert, and environmentally benign [88]. Incorporating metal species onto the surface of graphene is a well-known strategy to improve the hydrogen storage capacity. Based on the DFT method, in the case of Li, it was shown that each adsorbed Li on graphene and nanostructured graphene can adsorb up to four H_2 molecules amounting to a gravimetric density above 10 wt % [89]. The doping of graphene substrate with Bore (B) is also shown to have an increased hydrogen adsorption due to the creation of new

adsorption sites. Ab-initio calculations have shown that the storage capacity could reach up to 19.95 wt% when B-doped on both sides of the graphene [90].

1.5.2 2D-Graphane

One important development since the discovery of graphene is the discovery of the so-called graphane [91], has also been proposed for hydrogen storage. The improvement of hydrogen adsorption energy and gravimetric storage capacity of system have been extensively studied theoretically. MC simulations showed that the adsorption behaviour of graphane is similar to that of graphene monolayer [92]. DFT calculations and molecular dynamic studies on hydrogen adsorption by graphane modified with B atoms exhibited an increase in hydrogen binding energy from -35.56 to -81,52 meV [93]. The introduction of B atoms induced dipole moment which subsequently improved the electrostatic interaction between H_2 and graphane system. Although the stability of graphane has been demonstrated, up to now its application for hydrogen storage application is limited to theoretical studies only. Practical application has not yet been achieved.

1.5.3 2D-Graphyne

A new allotrope of carbon was predicted [94] by replacing one-third of -C-C- bonds in graphite by acetylene linkages constituting a 2D planar sheet with an equal number of sp^2 and sp carbon elements. In the context of H_2 storage, lithuim provides efficient binding of hydrogen to the graphyne surface, each Li can bind four H_2 molecules, corresponding to a hydrogen storage capacity of 15.15 wt% [95]. First principle calculations have shown that Sc can strongly bind to graphyne with improved binding energy due to additional in-plane pi states available in graphyne (-360 eV/H_2) with enhanced hydrogen storage capacity of 9.80 wt% [96]. Doping with heteroatoms like N, P, S, F, Al, B, As and Ga can also upgrade the adsorption of hydrogen on graphyne [97].

1.5.4 2D-t-graphene

t-graphene is sometimes also called the square-octagon [98]. Its crystal structure belongs to the plane group p4mm and each primitive cell contains four Carbon atoms. t-graphene was proposed to show several outstanding properties, such as Dirac-like fermions in the buckled form, excellent mechanical performance, and high critical-temperature superconductivity [99]. It is worth noticing that, t-graphene naturally has good thermal stability and very low elemental mass, which comfortably satisfy the requirements for hydrogen storage.
Thus, Ye et *al* [100] have studied in detail the H_2 adsorption properties of Li-decorated

system and reported that each Li-dopant can catch up to four H_2 molecules with an average binding energy of -0.144 eV per H_2 and a maximum gravimetric hydrogen storage capacity of 7.7 wt%. The studies on t-graphene are also limited to theoretical studies.

1.5.5 2D-Hexagonal boron nitride

The hexagonal structure in boron nitride nanomaterial is an isomorph of graphene system with the same crystalline structure; however, these materials exhibit different physicochemical properties. As carbon, BN displays a variety of structures, such as hexagonal (h-BN), cubic (c-BN), wurtzite (w-BN), tetragonal (t-BN) and amorphous phases.
In 2002 [101], h-BN was introduced as a promising candidate for hydrogen adsorption. Then, the experimental realization of hydrogen storage has been realised using oxygen doped BN with 2–6 atomic layers [102]. It was found that the hydrogen storage capacity increased to 5.7 wt% and 5 MPa at room temperature. Also, 89% of stored hydrogen could be released when the pressure was reduced to ambient conditions. Theoretical studies indicates that H_2 storage capacity is enhanced in defective and metal-doped BN system. For examples, the hydrogen storage capacity can reach 7.17 wt% if defective BN were decorated with metal Ti [103, 104]. Also, in all cases, doping/substitution or decoration is recommended rather than using pure BN. In the same frame, we investigated and illustrated the possibility of Li-decorated tetragonal boron nitride ($Li@t-BN$ or $Li@t-B_4N_4$) monolayer as a prospective medium for hydrogen storage using DFT calculations, more details in Chapter 5 .

1.6 Summary

The past few sections have discussed four very different ways to store hydrogen, especially in metal-organic frameworks (MOFs) and two-dimensional materials (2D). In fact, compressed hydrogen storage is beneficial for fuel purpose but requires a high pressure tank which limits their use while liquid hydrogen offers high volumetric energy density but fails as being an energy extensive method. Corrosion is another problem that occurs due to the formation of ice around the tank that leads to boil off.
On the other hand, hydrogen has been adsorbed on porous systems (physisorption) which possess high gravimetric capacity, fast hydrogen adsorption and desorption cycles. Problems like metal clustering, adsorption at low temperature or high pressure and weak interaction with the H_2 molecules limits their use. Also, metal hydrides (chemical storage) offer high gravimetric capacity but require high pressure and temperature for hydride formation and hydrogen release.
After more than 30 years of investigation of metal hydride and MOFs, extensive ad-

vances have been achieved on improving their hydrogenation characteristics, through two-dimensional (2D) materials due to their high surface area and remarkable chemical stability. In this context, we investigated and demonstrated the possibility of t-graphene, t-BN and Be_2C monolayer as a prospective medium for hydrogen storage applications using first principle ab initio calculations.

Chapter 2

Theoretical background: DFT and AIMD

2.1 Introduction

The research presented in this thesis was realized using the computational technique of *Density Functional Theory (DFT)* which allows for the atomic scale modelling of materials with the inclusion of the processes from macroscopic to microscopic scale. The DFT approach was used to calculate the ground state energies of systems, that is exact, are based on the approximation for the electron-electron interaction energy. These approaches are not only providing deeper understanding of molecular and crystal structures but also offering an economic and effective route to design new materials for various applications. The purpose of this chapter is to present the different tools used for modeling and studying the physical properties of the systems we suggested in the previous chapter. Since the DFT is based on of the **Schrödinger Equation**, we will briefly provide approximations and different methods to solve it.

2.2 Density Functional Theory (DFT)

The Schrodinger equation can fully describe the quantum state of a particular set of atoms. However, solving the partial differential equation for most systems is infeasible as the equation becomes a manybody problem with an enormous number of dimensions. Building on a number of approximations, DFT technique is able solve the non-relativistic time-independent Schrodinger equation by greatly reducing the number of dimensions and can reasonably predict the ground (lowest energy) state quantum properties for a wide variety of systems in a practical time frame. At the stationary state the energy of the system is constant over time. Thus, the Schrodinger equation that depends on the time

may be reduced to stationnary state Schrondinger equation:

$$\hat{H}\Psi_n = \xi_n \Psi_n \tag{2.1}$$

where Ψ_n is the many-body wave function of electrons, ξ_n is the total energy of solid, and $\hat{H}$ is the Hamiltonian operator for the whole system of electrons and nuclei, which is defined as:

$$\hat{H} = -\sum_i \frac{\hbar^2 \bigtriangledown_i^2}{2m_e} - \sum_I \frac{\hbar^2 \bigtriangledown_I^2}{2M_I} + \frac{1}{2}\sum_{i \neq j} \frac{e^2}{\mid r_i - rj \mid} + \frac{1}{2}\sum_{I \neq J} \frac{Z_I Z_J e^2}{\mid R_I - R_J \mid} - \sum_{i,I} \frac{Z_I e^2}{\mid r_i - R_I \mid} \tag{2.2}$$

where, $\hbar$ is Planck's constant devised by 2π, e and m_e denote the charge and the mass of a stationary electron, M_I and Z_I indicate respectively the mass and the charge (atomic number) of the nucleus (ion) and R_I and r_i stand for the positions of the nuclei and the electrons respectively.
In this expression, the first and the second terms correspond to the kinetic energies of the electrons ($\hat{T}_e$) and the nuclei ($\hat{T}_n$) while the reminder terms indicate, respectively, the Coulomb interactions of electron-electron (internal potential $\hat{V}_{e-e}$), nucleus-electron (external potential $\hat{V}_{n-e}$) and nucleus-nucleus ($\hat{V}_{n-n}$). So the Hamiltonian describing the solid simply reads as:

$$\hat{H} = \hat{T}_e + \hat{T}_n + \hat{V}_{e-e} + \hat{V}_{n-n} + \hat{V}_{n-e} \tag{2.3}$$

And the corresponding time independent Schrodinger equation with this Hamiltonian is given by:

$$\hat{H}\Psi(R_I, r_i) = \xi\Psi(R_I, r_i) \tag{2.4}$$

By solving exactly the last equation, all the macroscopic properties of the solid, in principle, would be determined. However, this kind of solution is a very hard task or even impossible for most cases. Indeed, this difficulty of solution is related, essentially, to the Coulomb many body terms $\hat{V}_{e-e}$ and $\hat{V}_{n-n}$. So, some approximations for this problem, depending on some physical considerations are required. Some of them will be briefly explained in next sections.

2.2.1 Born-Oppenheimer Approximation

Max Born and Robert Oppenheimer proposed an approximation to simplify the Schrödinger equation. This approach is today the basis of many calculations in the physics of matter. The Born-Oppenheimer approximation considers the position of atomic nuclei as fixed, from the simple observation that electrons are much lighter than nuclei [105]; their kinetic energy can therefore be neglected and the interaction term between nuclei

considered as a constant. Then we can decouple the nuclear and electronic movements, and the wave function of the system becomes:

$$\psi(R,r) = \psi_e(R,r)\psi_n(R) \tag{2.5}$$

However, the new equation obtained represents a N-body problem whose rigorous resolution can not be obtained analytically except in very simple cases like that of the hydrogen atom. Thus, the approximation of Born-Oppenheimer is important but still insufficient for solving the Schrodinger equation. Thus, other approximations should be introduced.

2.2.2 Hartree-Fock theory and the variational principle

After the Born-Oppenheimer approximation, the electronic wavefunction is still a function of the coordinates of all electrons in the system. The Hartree-Fock method seeks to approximately solve the electronic Schrödinger equation, and it assumes that the wavefunction can be approximated by a single Slater determinant made up of one spin orbital per electron. The objective of the HartreeFock method is to produce the best possible one-electron wavefunctions for use in approximating the exact wavefunction for a multi-electron system. In these models, we consider the H operator composed of the three operators (The kinetic operator, the interaction of an electron-nuclei and the interaction between all the electrons):

$$H = T_e + V_{e-e} + V_{e-n} \tag{2.6}$$

Hartree's approach

The Hartree approximation consists of replacing the interaction of each electron of the atom with all the others by the interaction with a mean field created by the nuclei and all the other electrons, that is to say that the electron moves independently in a middle field created by other electrons and nuclei [106, 107]. This makes it possible to replace the potential of the type $1/r_{ij}$ which depends on the coordinates of the two electrons by an expression defining the electronic interaction which depends on the coordinates of each isolated electron. Thus, within this approximation, the correlations are neglected allowing to write:

$$\psi_H(r) = \psi_1(r_1)\psi_2(r_2)...\psi_N(r_N) \tag{2.7}$$

Definition of Hartree Potential the potential of Hartree or Coulomb potential V_H is defined by [108]:

$$V_H(r) = \int \frac{n(r')}{\mid r - r' \mid} dr' \tag{2.8}$$

Which describes the interaction of an electron at a position r with an electronic cloud of density $n(r_0)$. We point out that, the equation Hartree's approximation ignores the antisymmetry of the wave function, as long as the electron is a fermion then the total wave function must be antisymmetric with respect to the exchange of any two particles that is neglected by Hartree.

Hartree-Fock theory

To overcome the shortcomings of Hartree approach, the introduction of anti symmetrise wavefunction was done within Hartree-Fock approximation. In this theorem, the many-body wavefunction is constructed in a Slater determinantal form.

$$\psi_{HF}(r_1...r_n) = \frac{1}{\sqrt{N!}} \begin{vmatrix} \psi_1(r_1) & \psi_1(r_2) & ... & \psi_1(r_n) \\ \psi_2(r_1) & \psi_2(r_2) & ... & \psi_2(r_n) \\ . & . & . & . \\ . & . & . & . \\ \psi_n(r_1) & \psi_n(r_2) & ... & \psi_n(r_n) \end{vmatrix} \tag{2.9}$$

With $\frac{1}{\sqrt{N!}}$ the normalization constant. This approximation leads to good results, particularly in molecular physics. Moreover, solving the system of (equation 2.9) remains difficult in the case of solids.

2.2.3 Hohenberg-Kohn theorem

In the year 1964, P. Hohenberg and W. Kohn [109] proved that the construction of the total energy of a physical system can be expressed in terms of the electronic density. The ideas are related to earlier propositions of Thomas and Fermi in 1927, where atoms were modeled as systems with a positive potential (the nucleus) located in a uniform electron gas [110, 111]. The two theorems can be stated as follows:

- **First Theorem**: The total energy of the fundamental state of the system is a single universal functional function of the electronic density for a given external potential; whether $E = E[\rho(r)]$. There are two classes of electrons, the spin-up electrons and the spin-down electrons. So the total energy is a functional (both electronic density of spin up and spindown $E = E[\rho_{up}(r), \rho_{dn}(r)]$. The general expression of the total energy is:

$$E[\rho(r)] = F_{HK}[\rho(r)] + \int \rho(r) V_{ext} dr \tag{2.10}$$

  In which $F_{HK}[\rho(r)]$ represents the universal functional of Hohenberg-Kohn.

- **Second Theorem**: A universal functional for the energy $E[n]$ in terms of the density $n_(r)$ can be defined, valid for any external potential $V_{ext}(r)$. For any particular $V_{ext}(r)$, the exact ground state energy of the system is the global minimum value of this functional and the density that minimizes the functional is the exact ground state density $n_0(r)$. This reduces the very complex problem of finding all ground state physical properties of a system to finding the minimum of the energy with respect to the electron density. The energy functional is as follows:

$$E_{HK}[n] = T[n] + E_{e-e}[n] + \int n(r)V_{ext}dr + E_{n-n} \tag{2.11}$$

where $E_{HK}[n]$ is the total energy functional, $T[n]$ its kinetic energy part, $E_{e-e}[n]$ the part coming from the electronic interactions and E_{n-n} is the energy of nuclei interaction. E_{n-n} does not depend on the density and is due to the nuclei-nuclei interaction. It should be noted that although the first Hohenberg-Kohn theorem requires a nondegenerate ground state, degenerate ground states are also allowed by the Levy formulation. It should also be noted that using the Hohenberg-Kohn formulation of DFT implies that we are working at T = 0K.

2.2.4 Kohn-Sham Formalism

In 1965, W. Kohn and L. Sham showed that there is a way to map the problem of solving equation 2.11 to the one of solving a system of non-interacting electrons moving in an effective potential from all the electrons. According to *Second Theorem*, the true electron density will minimize the total energy, but all means of finding it are valid. It could be guessed or, as suggested by Kohn and Sham, calculated from a reference system of non-interacting electrons moving in an effective potential. Thus, developing this variation with the full energy functional added (equation 2.11), under the condition that the sum of the density throughout the molecule or solid should be constant and equal to the number of electrons,

$$\int_V n(r)dr = n_e \tag{2.12}$$

finally gives the Schrödinger-like equations called the Kohn-Sham equations:

$$\left[-\frac{\nabla^2}{2} + V_{KS}(r)\right]\phi_i(r) = E_i\phi_i(r) \tag{2.13}$$

In which;

$$V_{KS}(r) = V_{ext}(r) + V_H(r) + V_{xc}(r), \tag{2.14}$$

in which $V_H(r)$ is the Hartree potential, written as

$$V_H(r) = \int \frac{n(r')}{\mid r - r' \mid} dr' \tag{2.15}$$

The term $V_{xc}(r)$ is the exchange-correlation potential, which is the partial derivative of the exchange-correlation energy E_{XC}, written as

$$V_{xc}(r) = \frac{\delta E_{XC}[n(r)]}{\delta[n(r)]} \tag{2.16}$$

Then the electron density of the ground state can be calculated by:

$$n(r) = \sum_{i}^{N} \mid \phi_i(r) \mid^2 \tag{2.17}$$

Then, we can calculate the total energy by the sum of the occupied eigenstate energy values. Now, the only thing left in the equation is the exchange-correlation energy term ($E_{XC}[n(r)]$), for which several efficient approximations have been proposed. In the next subsection, we will discuss two approximations for the exchange–correlation.

2.2.5 Exchange and Correlation Functionals

The Kohn–Sham equations provide the basis to calculate the kinetic energy correctly. However, the main challenge in DFT is to accurately calculate the exchange correlation energy. Clearly it is essential to find a good approximation of the exchange-correlation functional $E_{XC}[n(r)]$. In this section, the approximate expressions for exchange-correlation functional including LDA and GGA are briefly presented.

2.2.5.1 Local Density Approximation (LDA)

The first and simplest approximation for the exchange-correlation energy functional is the LDA approximation. In fact, the mean idea behind this approximation is revealed from a homogeneous electron gas. In the LDA approximation, it is assumed that the local exchange-correlation energy per electron depends on the local density, and this energy equals to the exchange-correlation energy per electron of a uniform electron gas having same density. The total exchange-correlation energy Exc can be then given by summing the contributions of each point in space as:

$$E_{XC}^{LDA}[n] = \int n(r) \xi_{XC}^{h}[n(r)] dr \tag{2.18}$$

In this equation, $\xi^h_{XC}[n(r)]$ stands for the exchange-correlation energy per electron of a homogeneous electron gas of density $n(r)$.
The LDA is more accurate for systems having slowly varying densities [112], as the assumed density is locally a constant.
The accuracy of this simple approximation almost leads to a correct picture of binding trends, structural parameters, vibrational energies, phonon spectra, bond lengths and other properties across the periodic table. Most of these properties are predicted correctly, or with a systematic deviation. However this approximation underestimates the band gap, and also overestimates the binding energy of solids and molecules which leads usually, to an underestimation of the bond lengths [113].

2.2.5.2 Generalized Gradient Approximation (GGA)

In LDA, one uses the knowledge of the density in a point r. In real systems the density varies in space. A logical improvement of the LDA approximation would be to include also information of this rate of change in the functional. This can be done by adding gradient terms. This approach is called the gradient-expansion approximation. In this class of approximation, one tries to systematically calculate gradient-corrections of the form $|\nabla n(r)|$,$|\nabla n(r)|^2$, $|\nabla^2 n(r)|$, etc., to the LDA. In practice, the inclusion of low-order gradient corrections almost never improves on the LDA, and often even worsens it. Moreover, higher-order corrections are exceedingly difficult to calculate and little is known about them. It was realized that instead of power-series like systematic gradient expansions one could experiment with more general functions of n(r) and $|\nabla n(r)|$ which needs not proceed order by order. Such functionals, of the general form:

$$E^{GGA}_{XC}[n] = \int \xi_{XC}(n, |\nabla n|, \nabla^2 n) dr \tag{2.19}$$

are known as generalized-gradient approximations. The current GGA seem to give reliable results for all main types of chemical bonds and are popular in computational chemistry. Overall, GGA type functionals, like PBE, are expected to be more accurate than LDA typefunctionals, meaning a GGA functional should give better results for a larger array of systems than an LDA functional. LDA functionals may perform better than GGA functionals for a particular system or a particular group of systems, but overall GGA functionals should give better result than LDA functional.

2.2.6 Plane wave pseudopotential method

Along with the proper handling of exchange-correlation functional, the solution of the Kohn-sham equation is feasible for the electronic systems. Moreover, for larger crys-

tals having a higher number of electrons, it becomes computationally expensive. One solution might be to decrease the number of effective electrons in the system. The reduction of electrons effectively introduces the concept of *pseudopotential*.
As illustrate in Figure 2.1, in the core region (the green part) the pseudopotential V^{ps} replaces the steep ionic potential V^{ae} with a much weaker effective potential. The corresponding wave functions Ψ^{ae} are replaced with pseudo wave functions Ψ^{ps}. Beyond the core region, the pseudopotential V^{ps} and the all-electron potential are identical, and thus corresponding pseudo wave functions and all-electron wave functions are also identical. In contrast to the wave functions of all electrons, the pseudo wave functions do not have nodal systems, making it possible to describe the pseudo wave functions with a small number of plane waves.

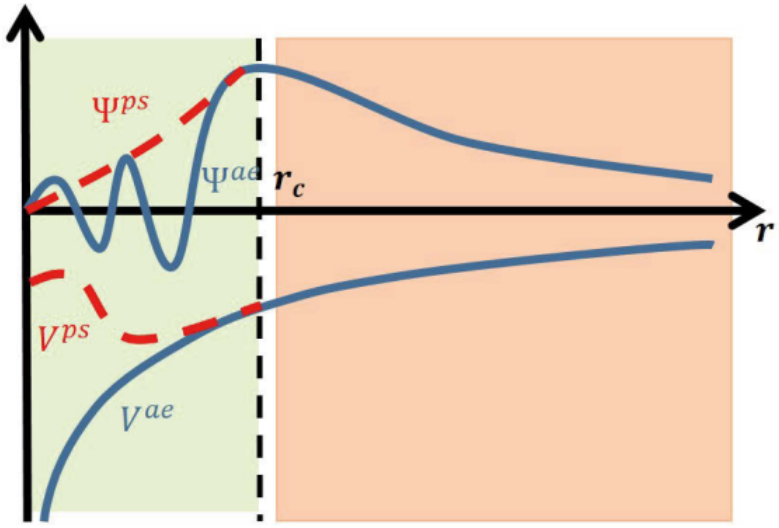


Figure 2.1: Illustration of the concept behind the pseudopotential and the pseudo wave function. The solid blue lines show the all-electron wave function Ψ^{ae} and the ionic potential V^{ae}. The dashed lines show the pseudo wave function Ψ^{ps} and pseudopotential V^{ps}. r is the distance from nuclear.

To understand the construction of the pseudopotential, let us first consider the exact core and valence states, as $\mid \phi_c >$ and $\mid \phi_v >$ and Schrödinger equation can be written as

$$H \mid \phi_i >= E_i \mid \phi_i > \tag{2.20}$$

where (i) defines both the valence and core states. We are interested to get smoother valence states in the core region. Defining a smooth pseudo-state $|\Psi^{ps} >$, we can write

$$\mid \phi_v >=\mid \Psi^{ps} > + \sum_c \mid \phi_c > \beta_{cv} \tag{2.21}$$

where $\beta_{cv} = - < \phi_c | \Psi^{ps} >$ defines that valence band has to be orthogonal to all of the core states. Further, using equations 2.20 and 2.21 one can get,

$$H \mid \Psi^{ps} > + \sum_c (E_v - E_c) \mid \phi_c >< \phi_c \mid \Psi^{ps} >= E_v \mid \Psi^{ps} > \tag{2.22}$$

And thus

$$H^{ps} \mid \Psi^{ps} >= E_v \mid \Psi^{ps} > \tag{2.23}$$

The last Eq. is analogous to the Schrödinger equation with a pseudo Hamiltonian and pseudopotential

$$H^{ps} = H + \sum_c (E_v - E_c) \mid \phi_c >< \phi_c \mid \tag{2.24}$$

$$V^{ps} = V_{eff} + \sum_c (E_v - E_c) \mid \phi_c >< \phi_c \mid \tag{2.25}$$

where V_{eff} describe the true potential, while the second term denotes the repulsive potential localized to the core region. Therefore, it cancels the strong attractive nuclear Coulomb potential and softens the fundamental potential (core). It results in a weaker pseudopotential and nodeless pseudo wave function.
Although the general ideas behind the pseudopotential approach are similar, there are several procedures to construct pseudopotentials, such as norm-conserving and ultrasoft. In this thesis, we make use of the pseudopotentials constructed using the Projector Augmented Wave (PAW) method as will be discussed in the next subsection.

2.2.6.1 Projector Augmented Waves: PAW

The projector augmented wave (PAW) [114] is a method for compute accurately the electronic properties of crystals. The PAW method combines features of the ultrasoft pseudopotential method [115] and the linear augmented plane wave method [116].
The wave function of the electrons varies greatly different depending on whether the electron is close to the nucleus or further away in the bonding region. Within an atomic centred sphere, the augmented region, the PAW method uses a partial–wave expansion to describe the electrons. This is done because it is computationally difficult to represent the wave function with plane waves in the fundamental region where the wave function oscillates rapidly. Outside the augmented region the electrons are described by plane waves or some other convenient basis set. Then the values and derivatives of the function are matched inside and outside the sphere.

2.2.7 Van der Waals Interactions

Van der Waals interactions or dispersion are due to electronic density fluctuations of distant regions in space. For overlapping charge distributions, the total potential energy between a pair of neutral atoms or molecules are approximated by Lennard Jones potential written as [117]

$$\chi(r) = -4\kappa \left[\left(\frac{\mu}{\rho}\right)^{6} - \left(\frac{\mu}{\rho}\right)^{12} \right] \tag{2.26}$$

where κ is the depth of the potential well, and μ is the distance at which interparticle potential is zero and ρ is the distance between particles. This potential has two terms, the attractive term which includes van der waals interactions with ρ^{-6} term and the repulsive term which is proportional to ρ^{-12}. The latter is associated with the Pauli exclusion principle which states that two fermions can not be in the same state. Van der Waals interaction, ρ^{-6} term on the other hand, arises from the long range interaction of electrons in the system. Quantum thermal fluctuations will always induce a dipole even in the neutral atom. The resulting electric field polarizes the other atom with the order of ρ^{-3}. The interaction is then in the order of ρ^{-6}. This correlation effect is also known as London dispersion and the resulting are attractive. In electronic structure simulations, this term has often been neglegted, however, in the range of physisorption as mentioned above, van der Waals interactions play an important role. Although it does not care with the sharing of electrons like in covalent bond or ionic bonds, the long-range effects of electrons are have also significant effects.

2.3 Quantum Espresso

The density functional theory calculations in my thesis are performed using the Quantum ESPRESSO package (QE) [118], which stands for *op**E**n **S**ource **P**ackage for **R**esearch in **E**lectronic **S**tructure, **S**imulation, and **O**ptimization.* It is a free software, released under the GNU General Public License. QE is designed to perform density functional theory calculations of the electronic structure. It uses plane wave basis sets and pseudopotential in its applications. The package includes functions such as self-consistent calculations and atomic relaxation (pw.x), atomic-projection (projwfc.x), post-processing (pp.x) and phonon calculation (ph.x). Quantum espresso code is written mostly in C, Fortran 95 and Fortran 77. Parallellization is also possible by MPI libraries which reduces computational cost considerably. The main advantages of QE over VASP in the context of this work are as follows: first, QE is able to characterize the vibrational frequencies into either Raman or infrared active modes. Secondly, QE assigns modes on the basis of the degeneracy of the vibrational frequencies (single, double or triple).

2.4 Nudged Elastic Band

A common and important problem in condensed matter is the identification of a lowest energy pathway for a rearrangement of a group of atoms from one stable configuration to another. ***The Nudged Elastic Band (NEB)*** method is essentially a method for finding the Minimum Energy Pathway (MEP) connecting two local minima on a potential energy surface [119]. The technique works by linearly interpolating a set of images between the initial and final states and minimizing the energy of this set of images. The images are forced to maintain their distance to neighboring images while energy minimization by adding spring forces between them along the path or band they form. The component of the potential force parallel to to the band is also removed from acting on the images, ensuring that only the spring forces act on images along the path and only potential forces act on the images perpendicular to the path. This prevents the images from relaxing to the minimum energy of the initial and final states. The Climbing Image (CI) implementation of NEB is a technique for finding the true saddle point along the MEP as normal NEB rarely has images present at this point [120]. In CI-NEB, the highest energy image is driven up to the saddle point by removing the spring forces acting on this image and inverting the true forces acting on this image along the tangent of the band. This results in the higher image moving toward the maximum surface of the potential energy in the direction of the band while decreasing its values on the surface of the potential energy in directions perpendicular to the band, bringing it to the definition of the saddle point.

2.5 Ab Initio Molecular Dynamics

So far we have assumed nuclei are fixed and focused on the ground state electronic properties in the static external potential generated by the nuclei. If one wants to consider nuclear motions, for example to investigate the effects of finite temperature, more complex methods are needed. An effective approach is to combine DFT electronic structure calculations with molecular dynamics simulations, named ***ab initio molecular dynamics*** or ***first principles molecular dynamics***.

Ab initio molecular dynamics simulations (AIMD), proposed by Car and Parrinello in 1985 [121], have led to a revolution in the development of computational physics. Exact forces can be derived from electronic structure calculations and used to determine the thermal motion of real, complex molecules, solids and liquids. Dynamical properties can be derived from AIMD. The Car-Parrinello approch marks the beginning of the AIMD era with a unified algorithm for electrons and ions. The conceptually simpler Born-Oppenheimer formalism became popular several years later [122].

This technique differs from classical molecular dynamics mainly in that it explicitly includes electronic effects separate from nuclei rather than considering the whole atom as a single solid sphere [123].

In general, molecular dynamics simulations can be performed in different thermodynamic frameworks. The most common groups are:

- *Microcanonical (NVE): the number of particles (N), the volume (V) and the total energy (E) are kept constant.*
- *Canonical (NVT): the number of particles (N), the volume (V) and the temperature (T) are kept constant. In this case we have to imagine the simulation box in thermal equilibrium with a heat bath. Here a thermostat algorithm is used. This modifies the Newton's equations of motion, rescaling the velocities of the particles, such that the distribution of the momenta corresponds to the Maxwell distribution. In this case, the energy is not conserved but fluctuates around a constant value, thus the configurations explored in a MD simulation do not have the same probability, like in the NVE ensemble.*
- *Isothermal isobaric (NPT): the number of particles (N), the pressure (P) and the temperature (T) are kept constant. We may see an isobaric system as coupled to a piston that is reproduced by a barostat algorithm. The barostat rescales the positions of the particles leading to a volume fluctuations, also in this case the total energy is not conserved but fluctuates around a constant value.*
- *Grand canonical (μVT): the chemical potential (μ), the volume (V) and the temperature (T) are kept constant. It permits fluctuations in the particle number at constant chemical potential, μ.*

Part I

Hydrogen Storage in Metal Organic Framework-5 (MOF-5)

Chapter 3

Modeling hydrogen adsorption in the MOF-5 connector

3.1 Motivation

As it is known, the high surface area, permanent porosity, tunable pore sizes, rigidity, structural flexibility and thermal stability make MOFs and especially Zn-MOF-5, able to bind hydrogen molecules in a non–dissociative manner [56, 64, 75, 61, 124]. Due to this feature, MOF-5 are promising candidates for application as hydrogen storage media. In these systems, unlike the magnesium hydride where the hydrogen is chemically bonded, the adsorption energy has to be decreased in order to be able to rise the storage temperature. Thus, the understanding of adsorption mechanisms is very important step towards optimizing and exploring new MOFs with good hydrogen storage properties at ambient conditions.
So, the connector crystal structure of MOF-5 in this work is used for the first time to determine the hydrogen storage properties of the whole structure of MOF-5. Thus, the results of the present chapter are devided in two parts. The first one is devoted to the presentation of the structural, electronic and thermodynamic properties of MOF-5 connector. The second part is reserved to treat the adsorption mechanism of hydrogen molecule with different orientations in multiple adsorption sites. Then, the diffusion of H_2 between the adsorption sites (metal, carboxylic and cyclic sites) is investigated according to the barrier energies for different paths.

3.2 Computational method

Calculations performed for our system are based on the density functional theory (DFT) using the pseudo potential method implemented in the Quantum espresso

code [118]. The parameterization of the exchange-correlation energy was done within the generalized gradient approximation (GGA)[125] of Perdew-Burke-Ernzerhof (PBE). The augmented projector wave method (PAW)[114] was used as well as the next valence electron configurations [Ar] $3d^{10}$ $4s^2$, [He] $2s^2$ $2p^4$, [He] $2s^2$ $2p^2$ and $1s^1$ for Zn, O, C and H, respectively. A value of 30 Ry of kinetic energy cutoff was considered for the use of wave function expansion. The self-coherent field cycle is selected to be 10^{-6} Ry for the structural energy convergence criteria with a Gaussian enlargement of 0.02 eV during structural relaxation. A mesh of 3×3×3 k-points was used in the irreducible part to sample the first Brillouin zone. The Visualization for Electronic and Structural Analysis (VESTA) and XcrysDen softwares were used for all post-treatment analyses [126, 127].

3.3 Results and discussion

3.3.1 Connector-MOF-5 geometry

The conventional structure of MOF-5 (see Figure 3.1(a)) has a cubic Fm-3m symmetry (no.225) with lattice constant 25.88 Å [61] and contains eight formula units of $Zn_4O(BDC)_3$ composed of 424 atoms whereas the primitive cell contains two formula (106 atoms in total) which is too expensive in time and requirements for computation. Thus, to avoid this computational inconvenient, we consider in this work the simplified system $Zn_4O(C_8H_4O_4)_3$ named **"connector"**, which is a side of the crystal structure of MOF-5. However, we explored all the properties in a single connector and a full periodic framework was included in all calculations of this work. The crystalline structure of the connector illustrated in Figure 3.1(b), has 12.36 Å as lattice parameter and contains 53 atoms: 4 Zn atoms, 13 O, 24 C and 12 Hydrogen atoms occupying 32f, 8c, 96k, 48g, 48g, 96k, and 96k Wyckoff positions, respectively.

The cell parameters and atomic positions were fully optimized. The obtained results of the relaxed lattice constants, inter-atomic distances and bond angles of the connector along with the experimental and theoretical data of MOF-5 are summarized in Table 3.1. From this table, we can notice that the optimized lattice parameter is slightly less than the experimental one and this difference is typical when using a GGA functionality. Furthermore, the bond length between two different atoms i.e. Zn-Zn, C-C and Zn-O and the angle of the O-C-O, Zn-O-C bonds are in good agreement with experimental and theoretical results (see Table 3.1) which confirms that the used model is able to simulate perfectly the properties of MOF-5 with an uncertainty lower than 1%.

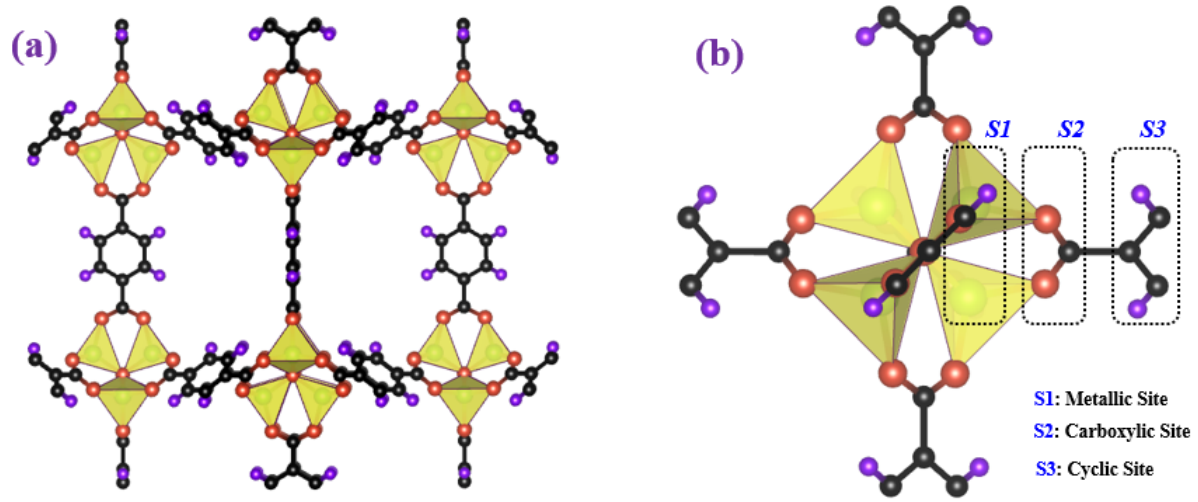


Figure 3.1: Representative schema of a) cubic MOF-5 structure, b) the simplified connector; zinc atoms are the yellow spheres, oxygen atoms are in red, carbon in black, and hydrogen is the purple one. The three adsorption positions: metallic site, carboxylic site and cyclic site are visualized in S1, S2 and S3 squares respectively.

	a_0(Å)	**Bond lengths**(Å)			**Angles**(°)	
		Zn-Zn	**C-C**	**Zn-O**	**O-C-O**	**Zn-O-C**
MOF-5 (Calculated)	24.29	3.15	1.41	1.93	126.50	134.50
MOF-5 (other works) [128, 129, 130]	26.13^a 26.14^b	3.22^a 3.20^b	1.40^a 1.42^b	1.90^c -	126.10^a 126.20^b	- -
Experimental [61]	25.88	3.18	1.40	1.91	125.80	133.80

Table 3.1: Experimental data and calculated values for the structural parameters of MOF-5

3.3.2 Connector stability: energy of formation and decomposition temperature

The energy of formation is a thermodynamic quantity which inform us on the stability of the connector and then is used to determine its decomposition temperature. The formation reaction of MOF-5 connector is:

$$4Zn + 13O + 24C + 6H_2 \longrightarrow Zn_4O(C_8H_4O_4)_3 \tag{3.1}$$

So, the formation energy is calculated by the following equation:

$$\Delta H_f = E_{tot}(Zn_4O(C_8H_4O_4)_3) - 4E_{tot}(Zn) - 13E_{tot}(O) - 24E_{tot}(C) - 6E_{tot}(H_2) \tag{3.2}$$

where, $E_{tot}(Zn_4O(C_8H_4O_4)_3)$ is the total energy of the connector, $E_{tot}(Zn)$, $E_{tot}(O)$, $E_{tot}(C)$, and $E_{tot}(H_2)$ are the total energy of zinc, oxygen, carbon and hydrogen molecule respectively computed for the ground-state structures with full geometry optimization. The obtained value of formation enthalpy of this system is -13.85 kJ/mol.H_2, that explains the stability of the connector. Furthermore, the decomposition temperature T_D is an important parameter for the classification of materials applied for hydrogen storage. The formation energy obtained above is used to determine the decomposition temperature of the studied connector using the following equation:

$$T_D = \frac{\Delta H_f}{\Delta S} \tag{3.3}$$

During the heating of the MOFs, the entropy change of solid materials is very small compared to the gas and this variation is primarily due to H_2 evolution so, the entropy change of organometallic materials is generally that of the Hydrogen $\Delta S = \Delta S(H_2) = 130(\pm 10) J.mol^{-1}K^{-1}$ [131]. Thus, the obtained value of the estimated decomposition temperature of the connector $T_D = 115.4$K indicates that the system has a very low temperature of decomposition, which is in good agreement with the experimental finding [132, 133].

Once assured of the validity of our model by determining the stability and the decomposition temperature of connector, we will begin the study of the hydrogen adsorption on the MOF-5's connector.

3.3.3 Hydrogen adsorption for the connector

To systematically understand H_2 adsorption in connector, first, the adsorption of a single molecule of hydrogen will be studied by considering different sites of adsorption at different orientations of H_2 molecule to determine the most stable both adsorption sites and orientation. The obtained results will then be used to calculate de coupling energy between two H_2 molecules, which allows us the adsorption study of several molecules and reach the maximum gravimetric and volumetric H_2 densities.

3.3.3.1 The first hydrogen adsorption sites and their energy

Modeling the interaction between hydrogen molecule and connector surface is a difficult task because a significant portion of the interaction may be caused by nonlocal electronic correlation. For this purpose, the most stable adsorption configuration must be determined very carefully by looking for the most stable adsorption site as well as the most favorable orientations. Thus, we consider three best-known adsorption sites [134] namely metallic site (between two Zn atoms), carboxylic site (between carbon and two

atoms of oxygen) and cyclic site (in the middle of the benzene) as shown in Figure 3.1(b). The first result of these investigations shows that the calculated link distance between H-H for an adsorbed hydrogen molecule is 0.748 and 0.749 Å depending on the site of adsorption and the orientation of H_2. This value is close to the experimental one of 0.75 Å for the hydrogen molecules [130], indicating that no dissociation of hydrogen occurred.

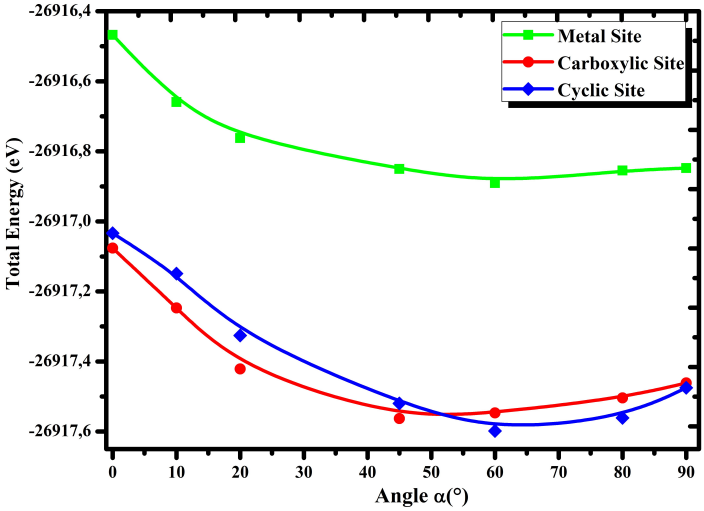


Figure 3.2: Energy as a function of the angle between the hydrogen molecule and the connector surface in the three adsorption sites

In addition, only 5 orientations of the molecule are stable. They are the horizontal (H), vertical (V) and sloping (S) orientations relative to the plane (x, y) with specific angles of inclination for each site that are 63 °, 45 °, 65 ° for S1, S2 and S3 sites, respectively as illustrated in Figure 3.2 that represents the energy optimization of the angle between the normal direction of hydrogen molecule and the connector surface in the three adsorption sites. Meanwhile, the corresponding adsorption energies (E_{ads})on the connector-MOF-5 were calculated by the following equation:

$$E_{ads} = [E_{Connector+nH_2} - E_{Connector} - nE_{H_2}]/n \tag{3.4}$$

where $E_{Connector+nH_2}$ corresponds to the total energy of combined system, $E_{Connector}$ the total energy of connector and E_{H_2} the total energy of H_2 molecule. n denotes the number of H_2 adsorbed on the system.

Due to the very small magnitude of adsorption energy and the lightness of hydrogen molecule, we take care to adopt exactly the same supercell, the same cutoff energy and the same k-points in the calculation of $E_{Connector+nH_2}$, $E_{Connector}$ and E_{H_2} to ensure maximum error cancellation [135]. The calculated results of the single H_2 adsorbed (n = 1) system, as shown in Figure 3.3.

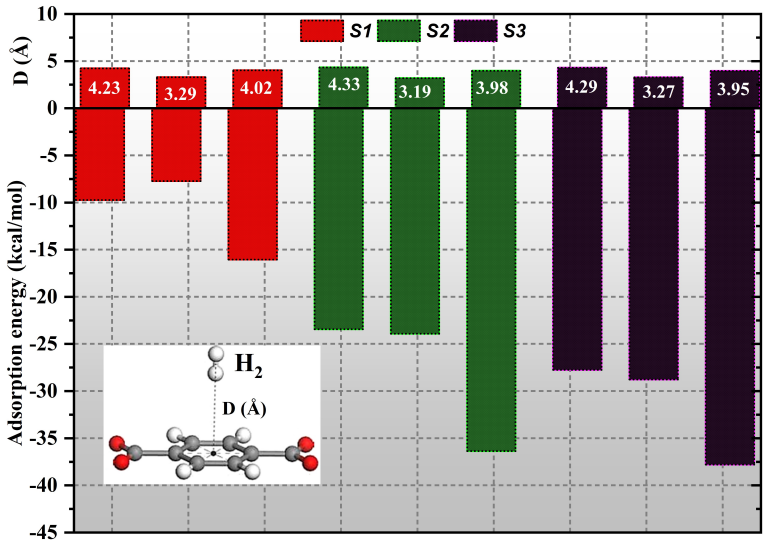


Figure 3.3: The first adsorption energy as a function of the adsorption site, orientation and adsorbate height in the connector of MOF-5

From Figure 3.3, we note that compared to the V and H orientations, the adsorption energy of one molecule of hydrogen is significantly stronger along a sloping orientation at the three sites of adsorption S1, S2 and S3 with adsorption distance varying between 3.95 Å and 4.02 Å. Moreover, among the different sites of adsorption, the cyclic one appears as the most favorable for adsorption of single hydrogen molecule with a value of -37.80 kcal/mol at a distance of 3.95 Å.

To discover the origin of the observed contraction of the structure during the H_2 loading, and understand the adsorption mechanism and the interaction between the connector and hydrogen molecules, we calculated the density of states, bonds and angles between atoms composing the connector and charge density before and after adsorption of H_2. Figure 3.4 shows the density of states (DOS) for each atom (Zn, O, C, H) without and with hydrogen adsorption; the Fermi level (E_f) is set to zero and used as a reference. From the PDOS of connector without H_2 adsorption (Figure 3.4(a)), we can notice that the valence band is mainly composed of strong hybridization between Zn-3d and O-2p, O-C states, additionally to moderately strong hybridizations between Zn and C states. However, there are weak hybridizations between the H-Zn, H-O and H-C states, leading to very weak interactions between H and the other atoms constituting the connector, resulting in weak bonds and therefore a low decomposition temperature which confirms the results of calculations in section of connector stability.

After H_2 adsorption (Figure 3.4(b)), in addition to the hybridization observed above, new hybridizations appear between H-O, H-C, H-Zn leading to a strong interaction between the adsorbed hydrogen and the other atoms, and therefore to an improve in the connector's both stability and desorption temperature. In the other hand, as we know that the

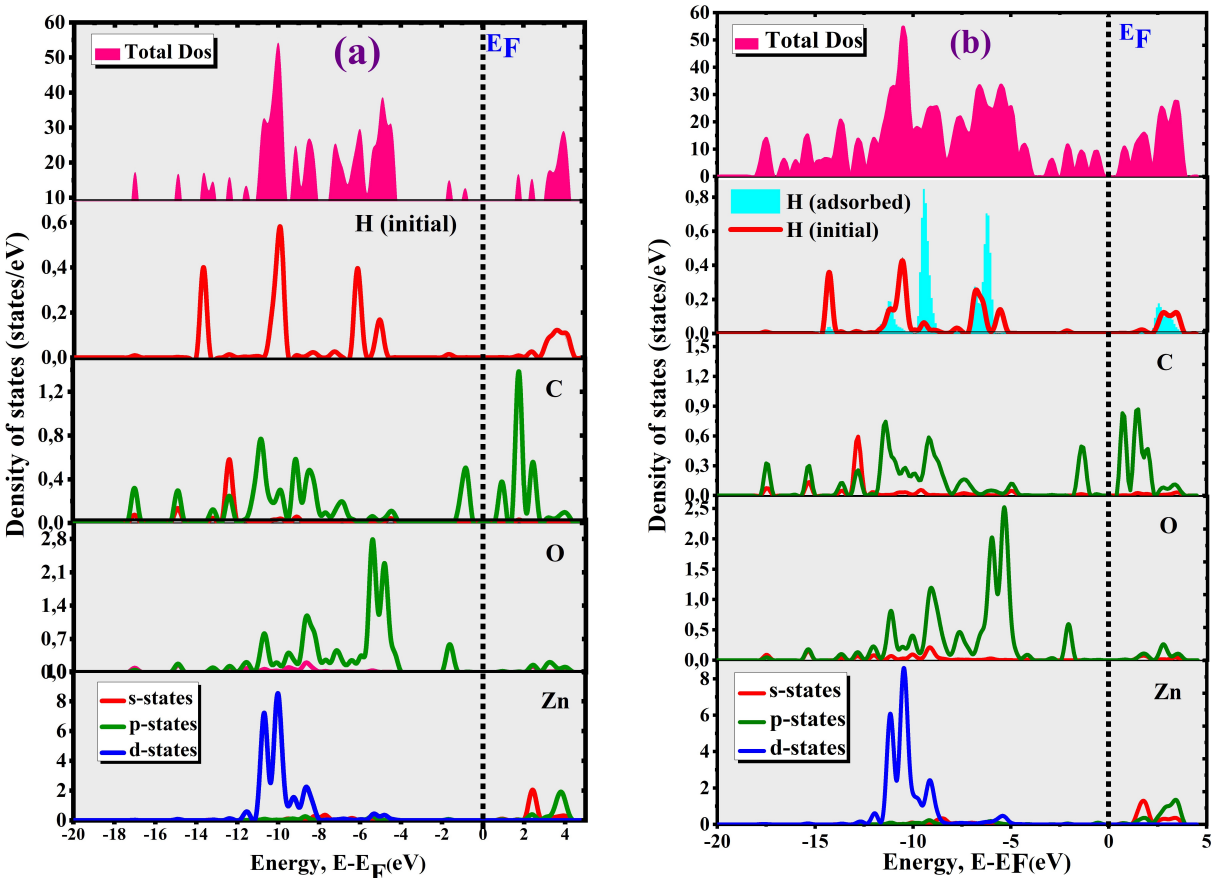


Figure 3.4: Calculated total and partial density of states for connector (a) without adsorption and (b) with adsorption of hydrogen molecule.

more the electronic states are towards the negative energies, the more the system is thermodynamically stable [136]. So, from the DOS, we notice a shift of atoms states towards the lowest energies as observed in ref [137].

For more details, we analyze the valence load density in the form of iso-energetic contours located in the plane (002) of the connector illustrated in Figure 3.5.

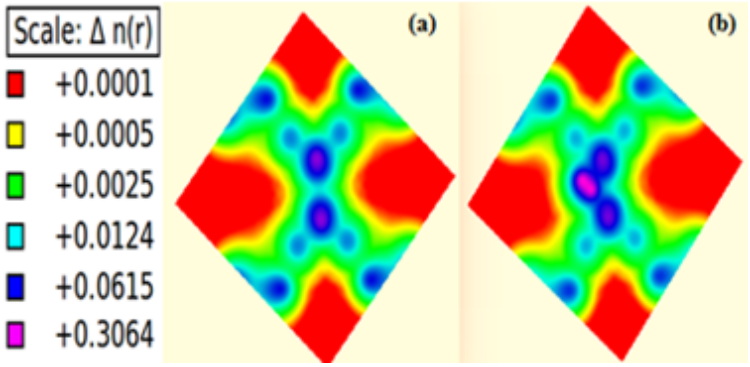


Figure 3.5: Density and transfer charge in this connector at plane (002) (a) without H_2 and (b) with H_2 adsorption

One can intuitively see in Figure 3.5(a) that the bonds in this connector of MOF-5 has a mixed nature. The Zn-C bond has a significant covalent character due to the charge sharing between Zn and C atoms. Obviously, the C-C, C-H and C-O atoms show covalent nature, while the bond between Zn and O is ionic due to the high electronegativity of the Zn that attracts the O atoms. After H_2 adsorption in the connector, we observe a decrease of the distance O-Zn and the bonds between Zn-Zn (Figure 3.5(b)) as well as a reduction of the Zn-O-C and O-C-O angles. On other hand, the nature of the interaction between the molecule H_2 and the connector surface that results from the loading of H_2 during the adsorption is attractive, which can invoke an electrostatic attraction (link dynamics). This electrostatic interaction is due to Madelung energy [138] which stipulates that the predominant long-distance interaction is the electrostatic interaction that is ensured by the electrostatic force between spheres of opposite charges.

3.3.3.2 Adsorption energy for two hydrogen molecules

Once the adsorption of a single H_2 on the zinc-based MOF-5 connector was investigated, we will now study the phenomenon of **co-action effect** [139] by considering the adsorption of two hydrogen molecules at the same time with three orientations, as shown in Figure 3.6.

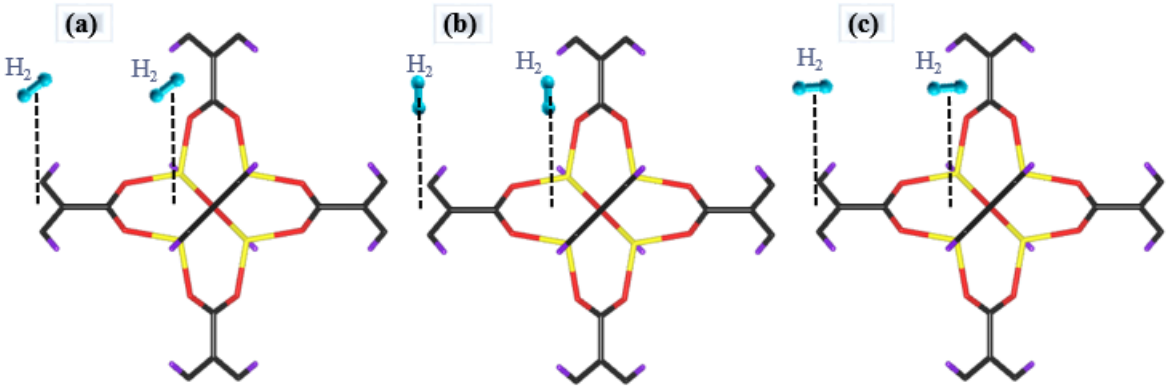


Figure 3.6: Sorption structures of two molecules of hydrogen on the S1-S3 site with: (a) S-S, (b) V-V, (c) H-H orientations of the two H_2

This phenomenon stipulates that a combination of two hydrogen molecules simultaneously produces a better result than that obtained of two H_2 individually. The aim of this part of study is to find the two most favorable sites for simultaneous adsorption of two molecules of hydrogen based on the coupling energy parameter. For that, we define the coupling energy (E_{Cp}) according to the following relation:

$$E_{Cp} = (E_{12})_{ij} - (E_1)_i - (E_2)_j \tag{3.5}$$

where $(E_1)_i$ is the adsorption energy of one single molecule of hydrogen at site (i), $(E_2)_j$ is the adsorption energy of the other single H_2 molecule at site (j), and $(E_{12})_{ij}$ is the adsorption energy of two molecules of hydrogen at the same time at both sites (i) and (j). According to several coupling energy calculations, the results indicate that among the different possible configurations of orientation, the two simultaneous molecules of hydrogen prefer to be adsorbed along the same orientation namely S-S, V-V and H-H orientations (Figure 3.6(a-b)). The obtained results for the coupling energy are summarized in Table 3.2.

Adsorption site	$E_{Cp}(kcal/mol)$		
	H	**V**	**S**
S1-S2	-2.53	-2.30	-4.52
S1-S3	-5.48	-6.50	-5.56
S2-S3	-2.01	-3.45	-1.02

Table 3.2: Coupling energies of two molecules of hydrogen in the system

It is evident from Table 3.2 that E_{Cp} have high negative values, means that the simultaneous adsorption of two molecules of H_2 is more favorable than the individual adsorption of two molecules of hydrogen. In other words, the first molecule of hydrogen helps the second one to be adsorbed more easily as evoked by the authors of ref [140]. In general, the calculations show that the S1-S3 site is more favorable in all orientations than the S1-S2 and S2-S3 sites and more precisely with a vertical orientation of the two molecules -6.50 kcal/mol. These results indicate that a pair of vertical hydrogen molecules adsorbed at same time at the S1-S3 sites is located in the non-repulsive distance to avoid the interaction effects between H_2 molecules that may destabilize the structure.

3.3.3.3 High-coverage of H_2 adsorption and storage capacities

Using previously mentioned, we will study the multiple adsorption of several molecules on the connector and subsequently determine their effect on storage capacities. The strategy followed is to adsorb several molecules of hydrogen on two sites at the same time according to the coupling energy results in order to reach saturation for this connector. In this case, many molecules of hydrogen can be adsorbed in the connector according to three orientations of the hydrogen molecule, at two different sites namely the S1 and the S3 one, as shown in Figure 3.6. In addition to the coupling energy, the loading of H_2 in the system was done by respecting two criteria: the filling by H_2 was stopped once a structural deformation is observed or if the energy of the adsorption was too high. The obtained results of the adsorption energies of the several H_2 molecules and the average distance separating them from the substrate are compiled in Table 3.3.

	H		S		V	
nH_2	$E_{ads}(kcal/mol)$	D(Å)	$E_{ads}(kcal/mol)$	D(Å)	$E_{ads}(kcal/mol)$	D(Å)
n=2	-9.31	3.60	-7.10	3.90	-23.57	3.20
n=4	-13.11	3.60	-8.15	3.90	-24.25	3.20
n=6	-14.22	3.60	-10.10	3.92	-24.23	3.30
n=8	-15.20	3.60	-9.80	3.92	-22.57	3.30
n=9	-15.10	3.74	-7.63	3.96	-19.89	3.30
n=10	-14.20	3.74	-5.50	3.96	-16.56	3.30
n=11	-13.70	3.80	-5.23	4.02	-	-
n=12	-10.23	3.80	-5.05	4.02	-	-

Table 3.3: Calculated adsorption energies of nH_2 molecules on connector and average height between H_2 and substrate

As shown in Table 3.3, for horizontal and inclined orientations, the number of adsorbed molecules is important up to 12 molecules with a distance separating the adsorption plane and the H_2 molecules ranging from 3.60 Å to 4.02 Å. While for the vertical orientation, the connector can adsorb only 10 molecules of hydrogen before the deformation of this system. This quantitative difference is due to the fact that adsorption energies are much lower in the case of the vertical orientation ranging from -24.25 to -16.56 kcal/mol than the case of horizontal and inclined orientations which range between -15.20 and -5.05 kcal/mol.

Before investigating the effect of hydrogen molecule adsorption on the connector storage capacity, the connector has an initial gravimetric capacity of 1.57 wt.% (before the adsorption of the molecule), since it contains hydrogen atoms, which corresponds to 29.35 $g.L^{-1}.H_2$ in terms of volumetric capacity. The obtained values are in good agreement with those obtained previously in [70, 141].

Once the hydrogen molecules are adsorbed, the gravimetric capacity increases rapidly with the number of hydrogen molecules to reach 4.57wt.% in the case of horizontal and inclined orientations and 4.09wt.% for vertical one. The obtained values are in good agreement with the results found experimentally in [56, 141, 142], namely maximum capacities of 4.50-5.20wt.% for the MOF-5 with cubic three-dimensional expanded porous structure [143, 144]. Thus, we may consider that the followed method is very efficient for estimating the hydrogen capacity that can be adsorbed in the system.

3.3.3.4 Assessment of hydrogenation on connector properties

To get more inside, we studied the variation of the connector's lattice parameter and the desorption temperature as function of increasing hydrogen molecule number as shown in Figure 3.7.

Initially, the calculated lattice parameter is 12.36 Å which decreases almost linearly during

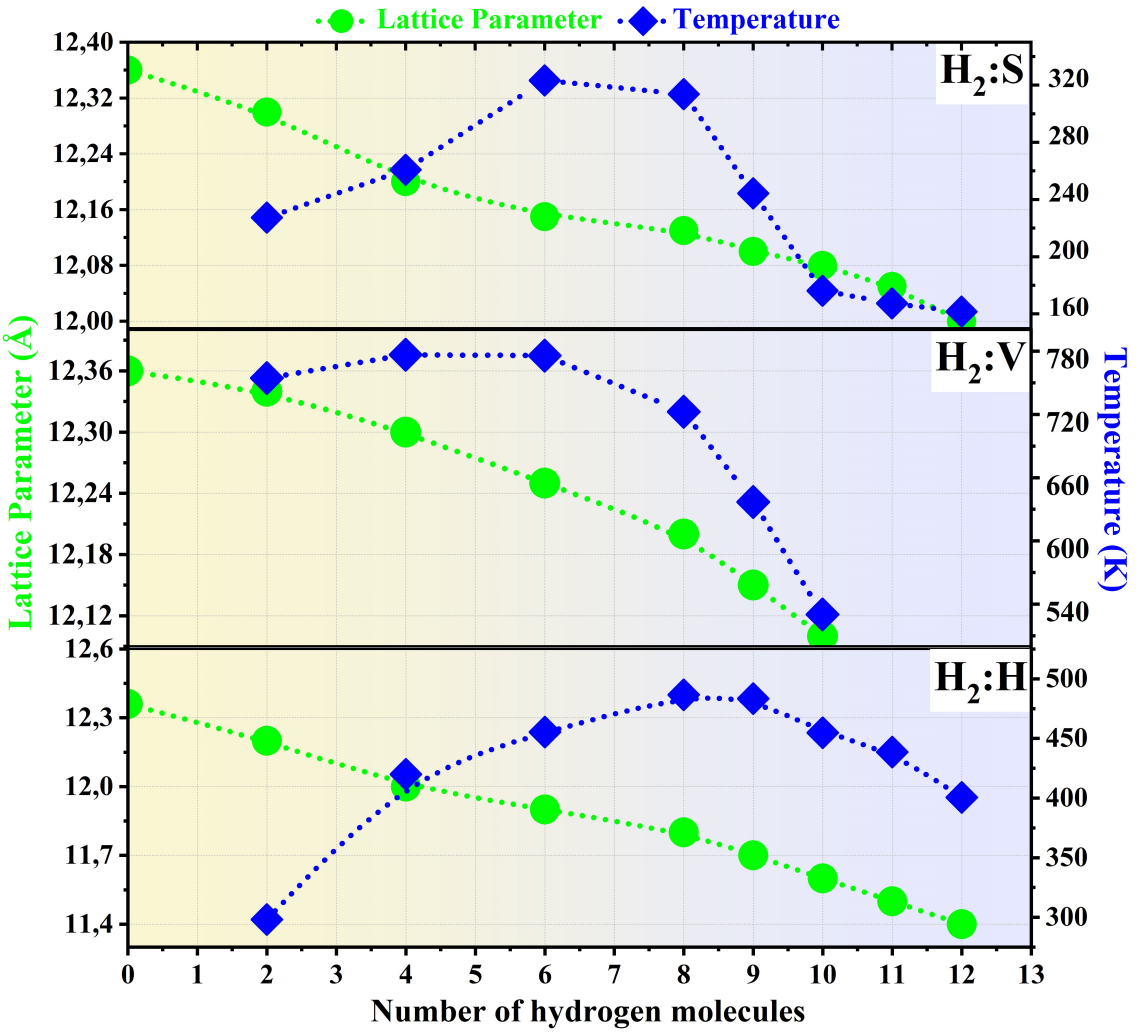


Figure 3.7: Variation of lattice parameters of connector as a function number of H_2 molecules adsorbed with desorption temperature for three orientations

the loading of molecules for the three orientations. For example, for sloping (Figure 3.7(a)) and vertical (Figure 3.7(b)) orientations the lattice parameters changes between 12.36 Å and 12 Å, while for the horizontal H_2 the parameter varies between 12.36 Å to 11.50 Å (Figure 3.7(c)). This trend indicates that the connector volume decreases as the gas loading increases, which confirms the trend observed by Yilidrim et *al.*[76]. In addition, the temperature of the connector calculated using the adsorption energy (Table 3.3) according to the equation 3.3, increases to a maximum equal to 780 K for 6 vertical H_2 molecules adsorbed, 470K for n=9 (H_2: horizontal orientation) and to reach 320K for 8 sloping molecules; see Figure 3.7. After that, the temperature decreases for the three orientations but remains higher than that of the case without adsorption (115K). It must be concluded when the system tends towards deformation, automatically the desorption temperature decreases.

3.3.3.5 H_2 molecular diffusion inside connector

The performance of hydrogen storage of a metal organic framework material depends also on the diffusion of hydrogen molecules inside it and plays a crucial role in its kinetic and stability [145].Therefore, we simulated the diffusion of a hydrogen molecule H_2 via the connector in two paths between the S1-S2 and S2-S3 sites. The H_2 diffusion barriers were calculated as the difference energy between the initial physisorption state and the transition state along three possible orientations, using the Nudge Elastic Band method [146] as described in Figure 3.8.
As Figure 3.8 shows, The energy profiles along the two diffusion paths with three orientations are plotted in Figure 10b. It is found that the migration barriers to H_2 molecule along S1-S2 paths are 21.73, 56.02 and 75.39 Kcal/mol, respectively. From S2-S3 path with H, V and S orientations are 0.24, 24.10 and 37.83 Kcal/mol, respectively, indicating that H_2 molecule diffusion is mainly along the S2-S3 with horizontal orientation, which is consistent with the previously calculated results [147] .
It can also be noted that the hydrogen molecule in sloping orientation are higher than that of diffusion along horizontal or vertical orientations. Finally, the barriers of migration of the hydrogen molecule in sloping orientation are higher than that of diffusion along horizontal or vertical orientations.

3.3.4 Summary and conclusion

Overall, our systematic investigation of hydrogen adsorption on the connector led to three important results. The first one is that due to the interaction of H_2 molecule with the surface of the Zn-based connector at three sites, the H_2 molecule is strongly adsorbed at the cyclic site and in particular along an sloping orientation with -37.80 $Kcal.mol^{-1}$ as adsorption energy. The second one is that the calculation of the coupling energies shows that in the multiple adsorption, the H_2 molecules are trapped more stably at S1 and S3 sites simultaneously and therefore this system can adsorb up to 12 molecules of hydrogen without structural deformation and reach a value of 4.57 wt.% as gravimetric capacity. The last one is that the desorption temperature is improved significantly and is much higher than 77K.

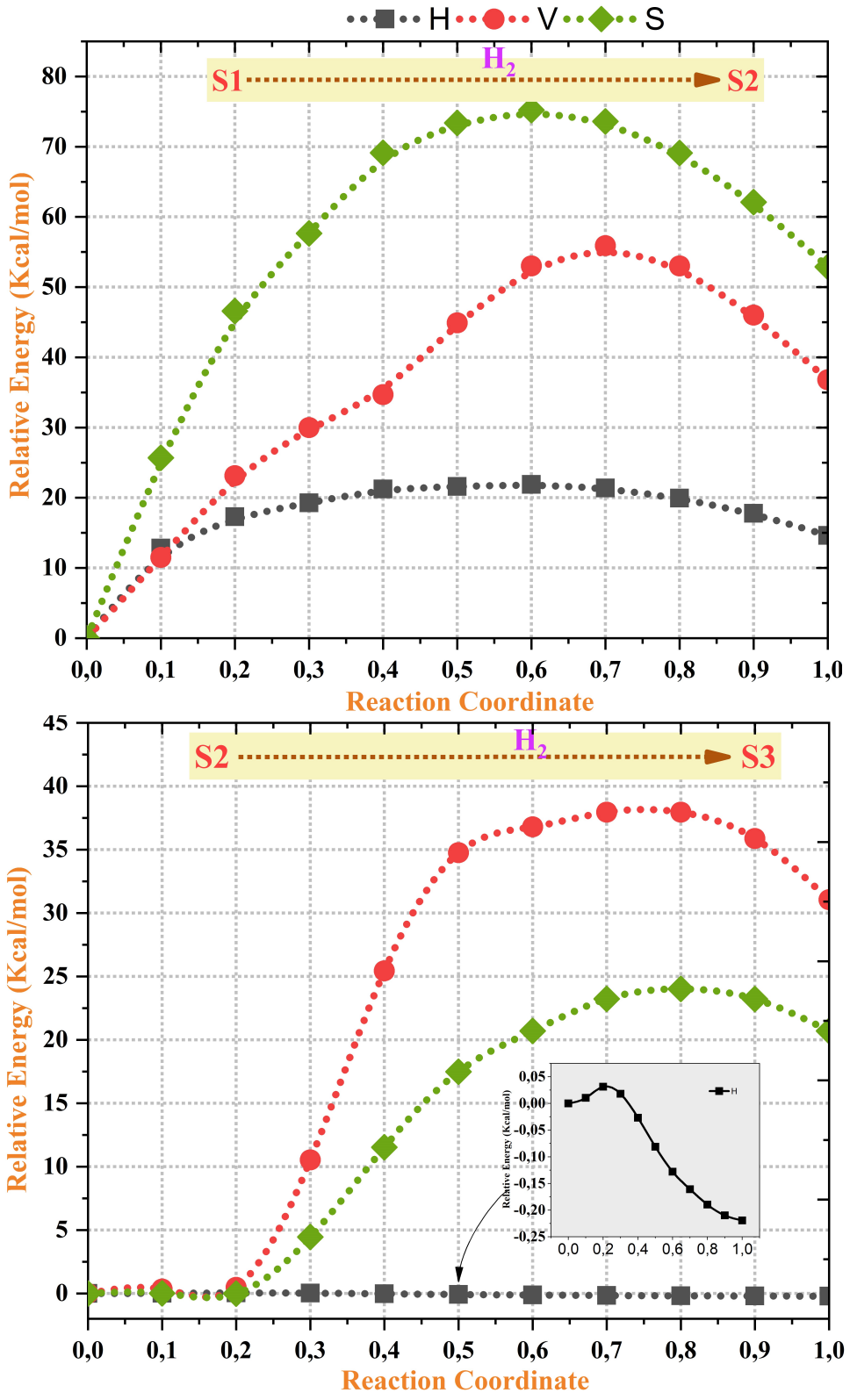


Figure 3.8: Corresponding energy profiles of H_2 migration in the $Zn_4O(C_8H_4O_4)_3$ system

Chapter 4

Lightweight metal decorating of M-MOF-5: Implications for hydrogen storage

4.1 Motivation

In order to improve the conditions of the hydrogen storage, we have to conceive new MOF-5 type materials having additionally to their suitable pore sizes and their large empty volumes, strong adsorption sites. This can be done by incorporating some elements on the surface of the material, such as Li, Ca, Sc ... [148, 149, 150, 77]. Moreover, one can conclude from different studies that the center, which is occupied by the metal M in M-MOF-5 (M = Zn, Cd, Mg ...) has a crucial role in adsorption of hydrogen molecules [151, 152, 153]. Recently, decoration of several elements has been carried out to improve the storage capacity of MOF-5 via both experimental and theoretical means [154, 128].

Here, the first part is devoted on the one hand to the structural, electronic and thermodynamic properties of the unit cell of Zn-MOF-5 on the other hand to the adsorption energies of a single hydrogen molecule in the three adsorption sites and three different H_2 orientations at the system surface. In the second part, the effects of the decoration by Li, Be and Na elements in the cyclic site on the adsorption energy, the capacity and the desorption temperature, with and without the substitution of Zn by Mg and Cd have been studied and the maximum of corresponding desorption temperatures were estimated. Finally, we give a conclusion about the different results.

4.2 Methodology and models

Our first-principles calculations were performed within the plane-wave technique of the local density approximation to density functional theory in the Quantum Espresso package [118]. The exchange and correlation potential of Kohn-Sham was treated using GGA-Perdew-Burke-Ernzerhof functional with Projector Augmented Waves (PAW)[125, 114]. To account for van der Waals interactions, important for hydrogen adsorption energies estimation, we used vdW-DF2 approach [155] throughout all calculations. A 40 Ry defined as plane-wave basis sets and 400 Ry as charge density grids are used as a cutoffs Energy. The residual forces are considered less than 0.01 eV $Å^{-1}$ per atom for all calculations and system optimizations during all relaxations. The Brillouin zone integration was performed with Gaussian widening and was applied by Monkhorst-Pack scheme [156] of a mesh of 3×3×3 k-point. For optimization of the primitive cell of MOF-5 the crystal structural parameters of metal-organic framework-5 were taken from experimental work [61].

The typical framework material chosen for this study consisted of 106 atoms, a mixture of organic 1,4-benzenedicarboxylate (BDC) and octahedral groups based on inorganic Zn. The crystal structure of the double connector is illustrated in Figure 4.1, contains: 8 atoms of Zn, 26 O, 48 C and 24 atoms of hydrogen occupying 32f, 8c, 96 k, 48 g, 48 g, 96 k and 96 k Wyckoff, respectively.

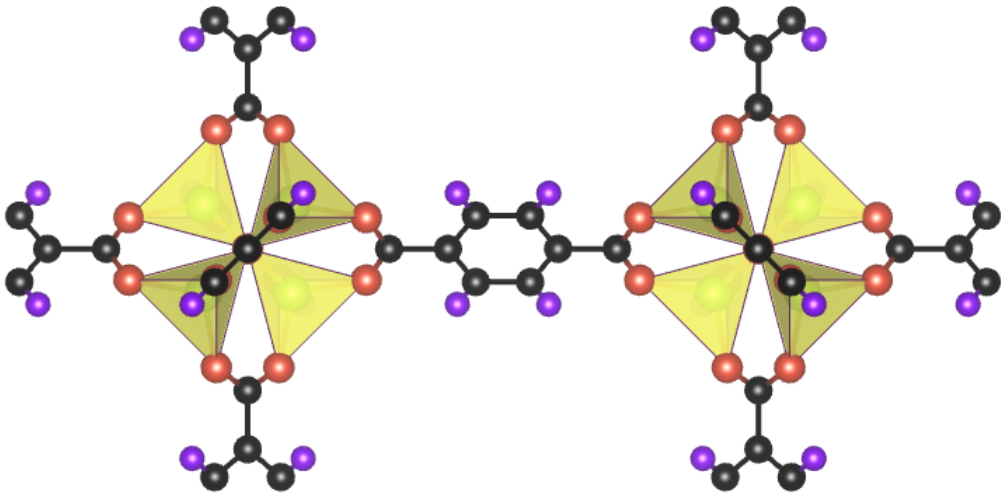


Figure 4.1: Unit cell of the double connector of Zn-MOF-5 crystal.

4.3 Results and discussions

4.3.1 Energy of formation considerations

Data on formation enthalpies constitute an excellent means to establish whether theoretically predicted phases are likely to be stable and also such data might serve as a guide to evaluate possible synthesis routes. The enthalpy of formation may be used also to determine the decomposition temperature of the following reaction:

$$8Zn + 13O_2 + 48C + 12H_2 \longrightarrow Zn_8O_{26}C_{48}H_{24} \tag{4.1}$$

From equation 4.1, we subtract the total energy difference between the products and the reactants of the system to calculate the formation energy by the following equation:

$$\Delta H = E_{tot}(Zn_8O_{26}C_{48}H_{24}) - 8E_{tot}(Zn) - 13E_{tot}(O_2) - 48E_{tot}(C) - 12E_{tot}(H_2) \tag{4.2}$$

where, $E_{tot}(Zn_8O_{26}C_{48}H_{24})$ is the total energy of unit cell-MOF-5, $E_{tot}(Zn)$, $E_{tot}(O_2)$, $E_{tot}(C)$, and $E_{tot}(H_2)$ are the total energy of zinc, oxygen, carbon and hydrogen molecule respectively.
So, the obtained value is -38.91 $kJmol^{-1}.H_2$ which is close to the typical one of MOF-5's full-structure (-46.02 $kJmol^{-1}.H_2$) [151, 157].
Since the standard Gibbs energy vanishes at the decomposition temperature, this can be estimated using:

$$T_D = \frac{\Delta H}{\Delta S} \tag{4.3}$$

where ΔH and ΔS are respectively the enthalpy and the entropy variations of the dehydrogenation reaction [158]. The entropy variation for MOFs is that of hydrogen which is of 130($\pm$10) $Jmol^{-1}K^{-1}$ [131]. Thus, the hydrogen decomposition temperature of the system at the initial state is 300 K.

4.3.2 Adsorption of one hydrogen molecule in Zn-MOF-5

Herein we begin with the optimization of the adsorption of a single hydrogen molecule in the primitive cell of MOF-5. Thus, we consider three most favorable sites of adsorption of an H_2 molecule, namely the metal, the carboxylic and the cyclic sites, with three orientations of the adsorbed hydrogen molecule (horizontal, vertical and sloping) in each adsorption site as shown in Figure 4.2
The optimised structure was used to calculate the adsorption energy for one H_2 molecule

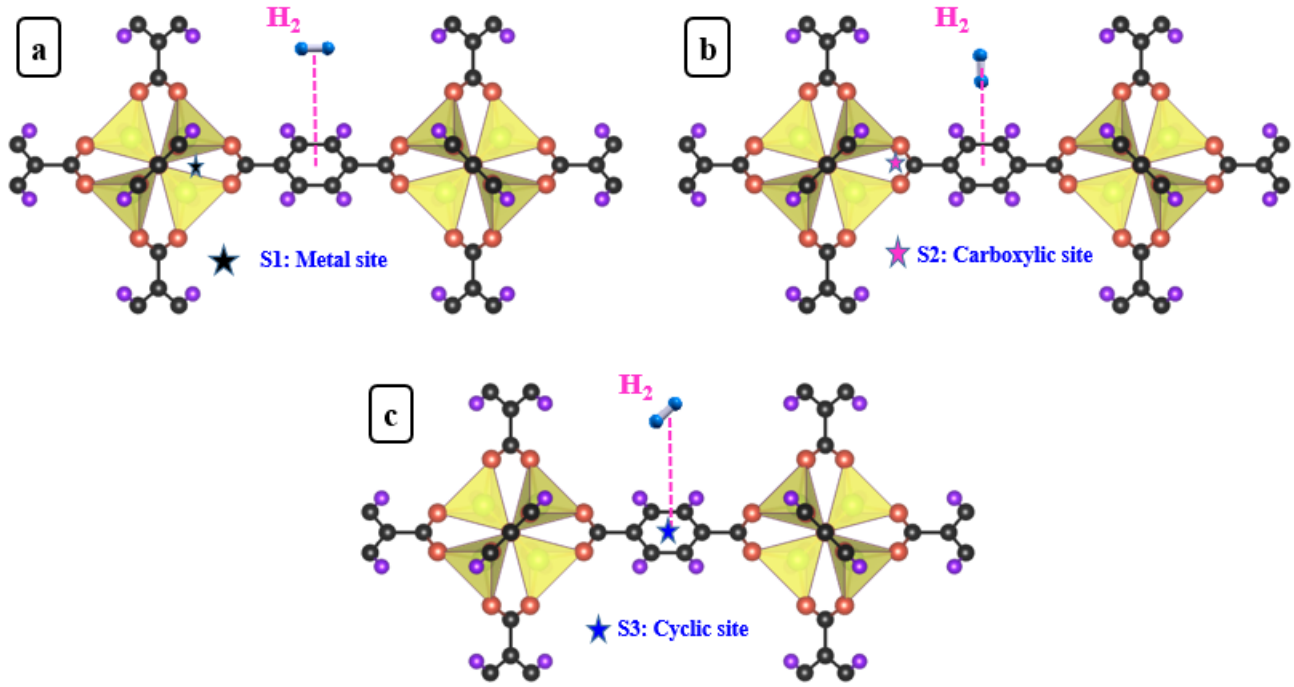


Figure 4.2: Hydrogen molecule adsorption in appropriate adsorption sites and along three orientations: (a) horizontal, (b) vertical and (c) sloping orientation.

at different zones and orientations on the unit cell-MOF-5 surface using equation 4.4:

$$E_{ads} = E_{MOF-5+H_2} - E_{MOF-5} - E_{H_2} \tag{4.4}$$

where $E_{MOF-5+H_2}$ is the energy of the unit cell-MOF-5 interacting with H_2, E_{MOF-5} is the energy of the unit cell-MOF-5 and E_{H_2} is the energy of hydrogen molecule. Thus, the different results are given in Table 4.1.

Adsorption site	**Orientation**	E_{ads}**(kcal/mol)**	**Adsorbat height(Å)**
Metallic site	H	-4.35	3.71
	V	-6.61	3.83
	S(63°)	-9.06	3.70
Carboxylic site	H	-1.81	3.46
	V	-3.08	3.63
	S(45°)	-3.65	3.83
Cyclic site	H	-12.91	3.59
	V	-14.21	3.75
	S(65°)	-15.17	4.10

Table 4.1: The adsorption energy for the three sites and their orientations vs the hydrogen molecule distance at the unit cell surface: (a) Horizontal, (b) Vertical and (c) Sloping

In Table 4.1, the examination of adsorption energies calculated at different sites and along

different orientations shows that the calculated E_{ads} for the sloping orientations of the H_2 molecule have the most favorable values in the three sites. i.e. -9.06 kcal/mol at 3.7 Å for metal site and for the carboxylic site is -3.65 kcal/mol at 3.83 Å. In addition, among the various strongly adsorbed sites, the cyclic appears to be the most favorable along the three orientations. In particular, the inclined orientation with specific inclination angles between the hydrogen molecule and the Zn-MOF-5 surface along the z-axis for each site that are 63°, 45°, 65° for metallic, carboxylic and cyclic sites, respectively gives the lowest adsorption energy value of -15.17 kcal/mol at a, distance of 4.10 Å.

To assess the mechanisms of interaction between molecular hydrogen and the unit cell-MOF-5, we have studied their electronic structure through total and partial density of states before as well as after the adsorption of H_2.

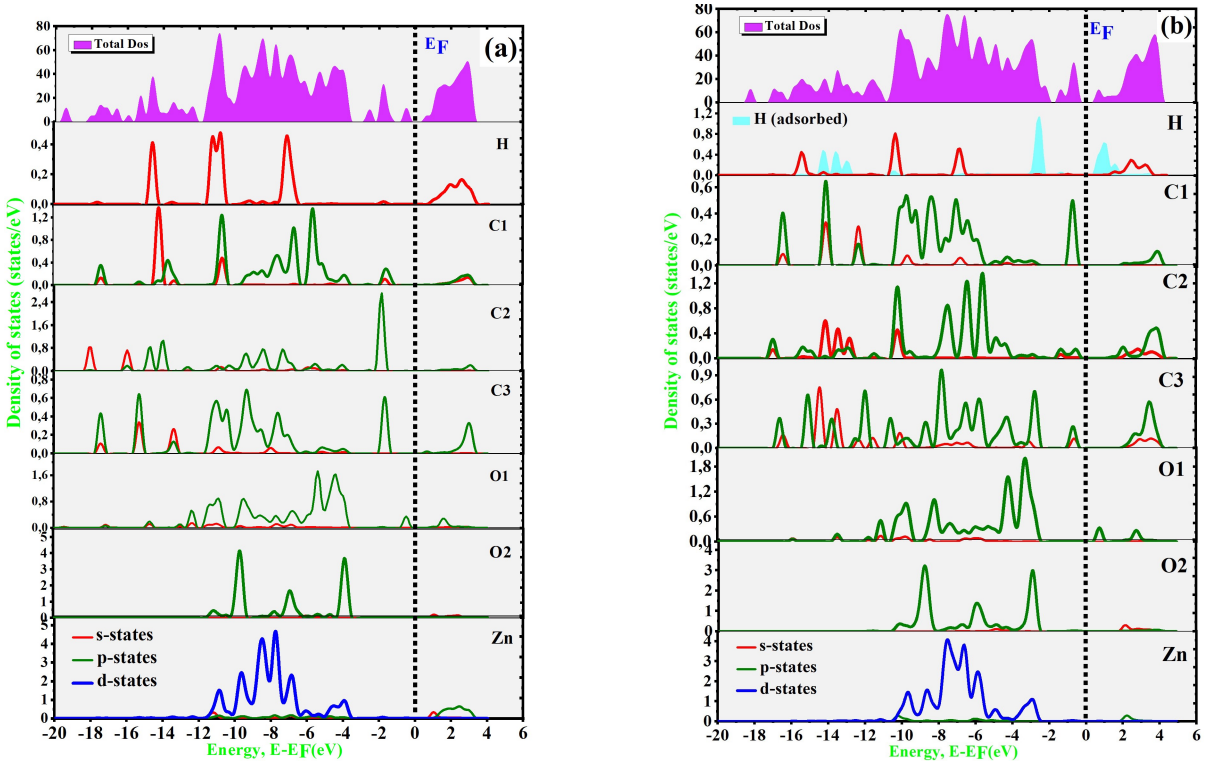


Figure 4.3: The total density of states (T-DOS) and partial density of states (P-DOS) for unit cell-MOF-5 based Zn before (a) and after (b) adsorption of single H_2

From Figure 4.3(a), before adsorption of hydrogen, the initial H atoms are weakly hybridized whit Zn, O1 and O2 while there is a strong hybridization between H-C1. After H_2 adsorption (see Figure 4.3(a)), in addition to the mentioned hybridizations, new strong ones appear between H-C2, H-C3, H-O1 and H-O2. Furthermore, as we know that the more the system is stable dynamically, the more his electronic states are oriented towards negative energies [159]. Therefore, from partial states of Hydrogen, we observe a shift in the states of H atoms towards lower energy after adsorption. Thus, we expect that it

would affect the adsorption mechanism of H_2 molecules in unit cell-MOF-5.
Additionally, the adsorption study of several hydrogen molecules shows that material can adsorb up $20H_2$ molecules before the deformation of the system occurs. Consequently, the hydrogen gravimetric capacity of this system is about 4.09 wt.% [141, 142]. However, the H_2 storage capacity remains less than 5.5 wt.%, a target proposed by the US-DoE to be met by 2025 [160]. Thus, to increase the hydrogen storage capacity of MOF-5, we propose two different strategies. The first one consists on substituting the Zn atom by Cd and Mg elements. In addition to the substitution, we will, in the second strategy, investigate the effect of the decoration by three elements namely Z=Li, Be and Na atoms in the most favorable adsorbed site which is the cyclic one.

4.3.3 Nature of M@MOF-5-Z and H_2-Z interactions

To examine the effect of Z doping on hydrogen adsorption, we first investigated the adsorption energy of doping Z atom on the carbon ring (C_6H_4 units) unit of M-MOF-5. The optimized configuration of the M-MOF-5:Z_2 primitive cell is shown in Figure 4.4.

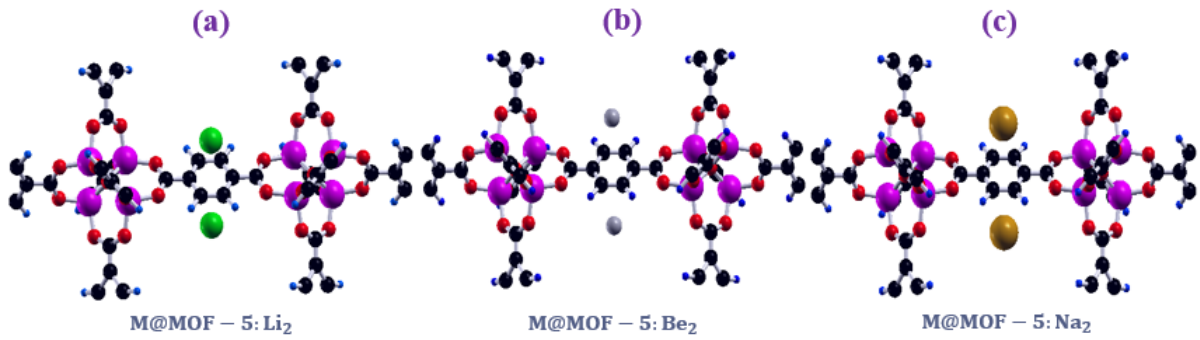


Figure 4.4: Z-decorated primitive cells of M-MOF-5. Gray, red, black and blue atoms represent the metal M = Zn, Cd and Mg, oxygen, carbon and hydrogen respectively

By completely optimizing structures, we can notice that the system can be decorated by two atoms simultaneously at cyclic site with adsorption energies values of the of Z= Li, Be and Na in MOF-5 based Zn are -37.12, -8.30 and -26.05 kcal/mol, respectively. The optimized distances between BDC and the decorated atoms are: 1.75 Å, 1.60 Å and 1.79 Å, for Li, Be and Na, respectively which represents an excellent agreement with the results of previous works [161, 129, 149]. These distances are not affected by the substitution of Zn by Mg and Cd because the cyclic site where the decorative elements are adsorbed is far away from the substitution's site.
After optimization of unit cell-MOF-5 M-based including Li, Be and Na atoms, we studied the effect of these atoms on the adsorption of a single hydrogen molecule in the most adsorbed site with three orientations according to results of section 4.3.2. Based on

the interaction between the Z-functionalized system and the H_2 molecule the adsorption energy can be defined by the following equation:

$$E_{ads} = [E_{system+nH_2} - E_{system} - nE_{H_2}]/n \tag{4.5}$$

where $E_{system+nH_2}$ and E_{system} are the total energy of the M-MOF-5:Z_2 system with and without hydrogen molecule respectively, while E_{H_2} represents the total energy of the hydrogen molecule, and n is the number of H_2 molecules. The resulting adsorption energies of a single hydrogen molecule on a unit cell of M-MOF-5 functionalized by Z_2 are shown in Figure 4.5.

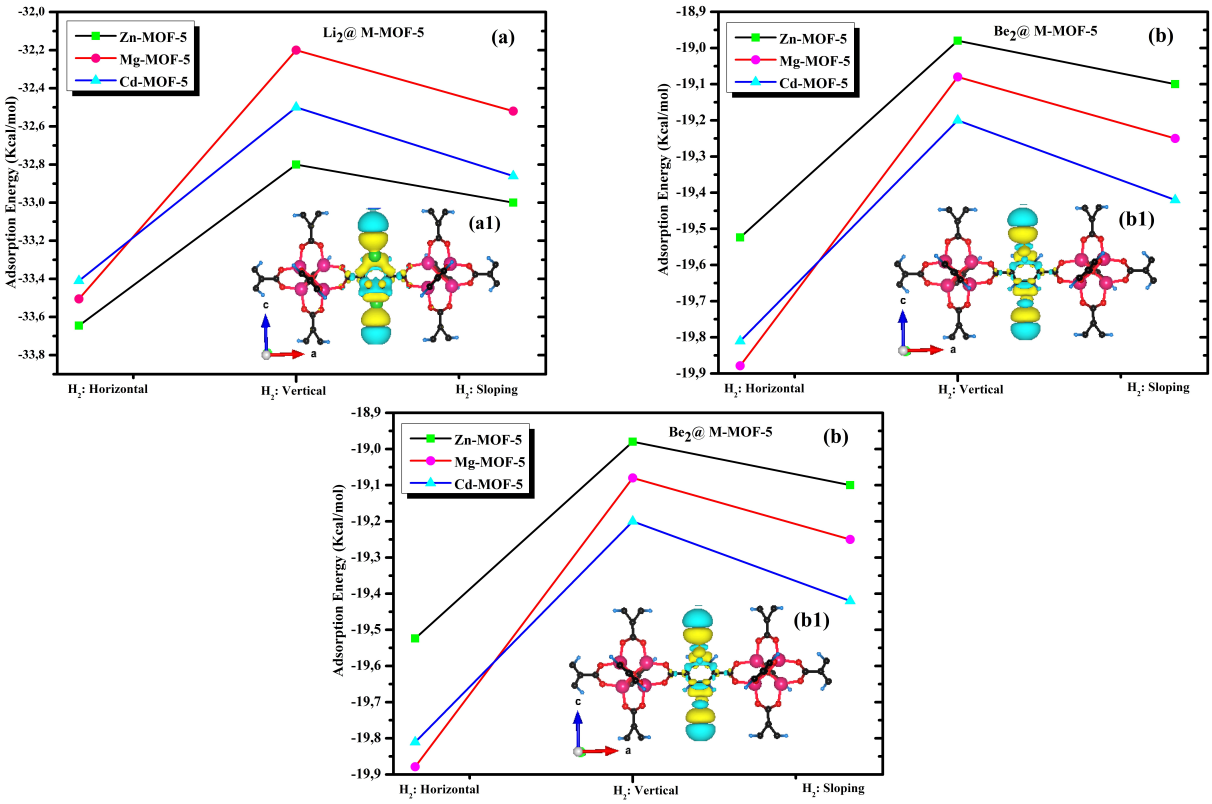


Figure 4.5: Adsorption energies for the three orientations of the adsorbed H_2 at the unit cell of M-MOF-5:Z_2 systems, where Z = Li (a), Be (b) and Na (c). (a1), (b1) and (c1) present the analysis of the charge density between H_2 and Z

In the case of Z-functionalized M-MOF-5, a reduction of the adsorption energies is observed compared to the system without decoration for the three orientations (see Figure 4.5). It is obvious that the horizontal orientation of the adsorbed hydrogen molecule is more adsorbent than vertical and inclined ones. As an example the most stable adsorption energies are for Zn-MOF-5:Li_2 with a value up to -33.65 kcal/mol, compared to -19.87 and -19.96 kcal/mol for Mg-MOF-5:Be_2 and Zn-MOF:Na_2, respectively. Consequently, the functionalization of Li_2 with dicarboxylic benzene (dilithium 1,4-benzenedicarboxylate)

gives better results compared to the other functionalization in M-MOF-5 [151, 162]. Thus, we expect an increase in storage capacities, especially with decoration by Li_2.

To gain insight into the H_2 adsorption mechanisms,we determined the difference in spatial charge distribution between the hydrogen molecule and the system decorated with Z_2. Thus, the spatial charge differences was calculated and plotted in Figure 4.5 (a1, b1 and c1) by using the following equation:

$$\Delta\rho = \rho_{system@H_2} - \rho_{system} - \rho_{H_2} \tag{4.6}$$

Herein $\rho_{system@H_2}$, ρ_{system} and ρ_{H_2} are the charge densities of the system decorated with Z after adsorption of the hydrogen molecule, the decorated system before adsorption of H_2 and hydrogen adsorbed molecule, respectively.
Figure 4.5 (a1, b1 and c1) depicts the charge density differences (CDD) plots of this M-MOF-5:Z_2 after hydrogen adsorption. We observe that the different systems exhibit the same behavior where there are evident zones of charge accumulation (yellow color) and depletion (blue color) on either side of BDC with the hydrogen molecule, indicating a strong polarization of hydrogen with the elements of Z-decoration. Therefore, there is a net charge transfer between the decorated system and the adsorbed hydrogen.

To further examine the type of bonding between the H_2 and the M-MOF-5:Z_2, the charge transfer mechanism was studied using a Bader analysis [163]. The self-coherent charge density revealed that the atoms of Li, Be and Na respectively carry a charge of 0.90, 0.43 and 0.86 e [77]. Thus, the difference in the electronegativity between M-MOF-5:Z_2 and H_2 is large enough to produce the desired ionic state of the atoms in the cyclic site, which is beneficial for increasing the adsorption affinity with hydrogen H_2. It is also important to assess the rate of hydrogen molecules that a decorative elements Z = Li, Be and Na can contain, we add the H_2 molecules one by one until the distance separating Li/Na/Be and H_2 becomes very large such that H_2 leaves the area in the vicinity of Z or the adsorption energy becomes very high as shown in Figure 4.6.
By following this method, we obtain 6 molecules of hydrogen in quasi molecular form in the cyclic site for the case of Li and Na as decorative elements. The obtained result is in good agreement with in Ref [161]. Moreover, Be_2 element can adsorb 5 molecules as a maximum quantity of hydrogen per BDC unit. Therefore, in the next step, we performed a study of multiple hydrogen molecules adsorption in the favorable sites of H_2 (metallic an cyclic sites) in M-MOF-5:Z_2.

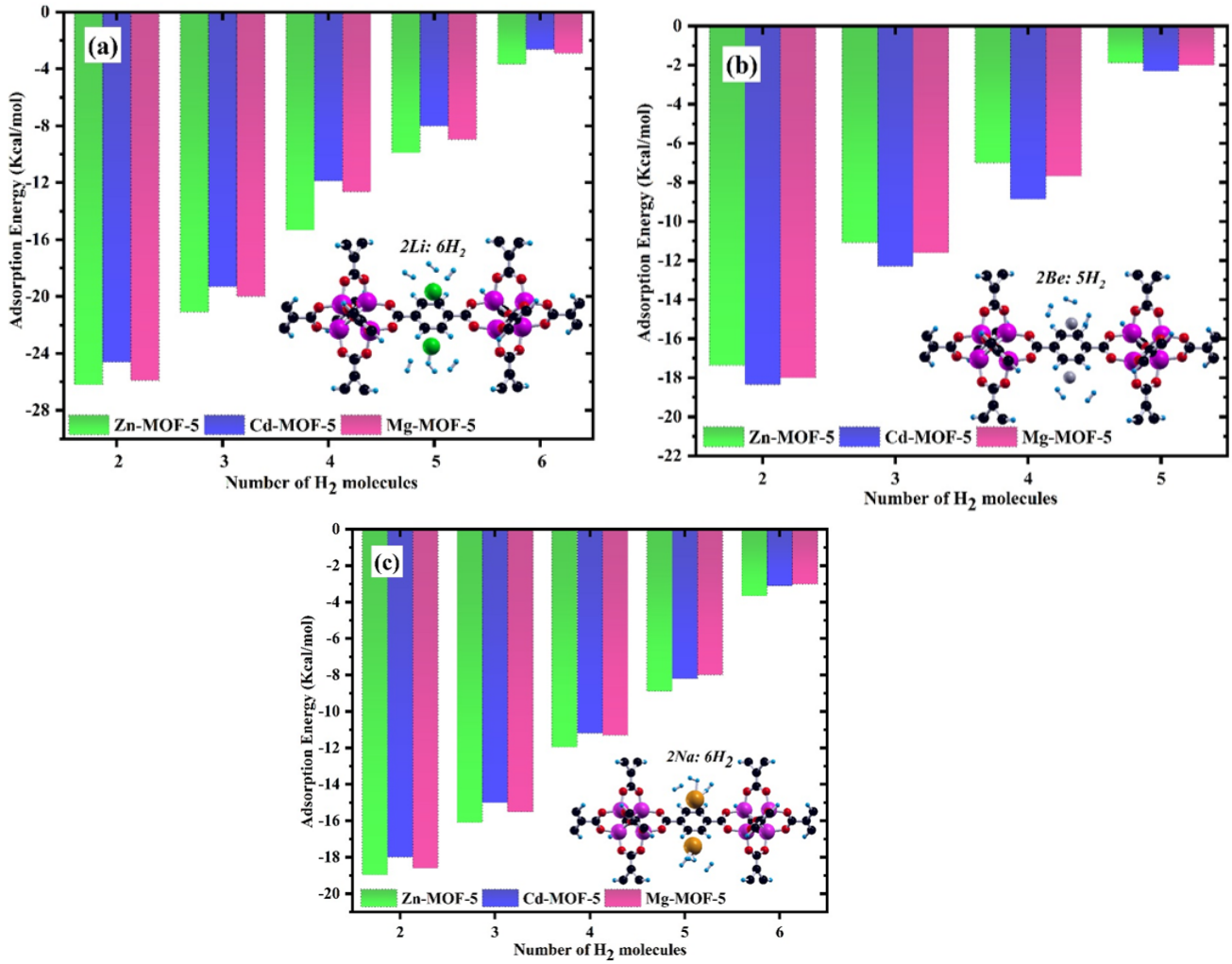


Figure 4.6: Adsorption energy as a function of adsorbed hydrogen molecules number at the cyclic site of M-MOF-5:Li_2 (a), M-MOF-5:Be_2 (b) and M-MOF-5:Na_2 (c)

4.3.4 Gravimetric storage and desorption temperature

The complete results for the average adsorption energies per H_2, the bond length between H-H, the distance between Z-H_2, as well as the storage capacities and desorption temperature in unit cell of M-MOF-5:Z_2 are given in Table 4.2.

From Table 4.2, it can be observed that the substitution Zn by Cd and Mg do not affect much the distance between the decoration elements and the hydrogen molecules in this system, as well as the inter-atomic distances H-H which are comprised between 0.740 and 0.751 Å. But on the other hand, there is a change in the adsorption energy with respect to Li, Be and Na. For example, The average adsorption energies varied from -9.45 to -15.96 kcal/mol for M-MOF-5:Li_2, from -9.72 to -13.72 kcal/mol for M-MOF-5:Na_2 and from -8.63 to -12.73 kcal/mol for M-MOF-5:Be_2. Thus, lithium-decorated Mg-MOF-5 is more stable compared to the other systems. In addition, the desorption temperature of

system		E_{ads}	D_{H-H}(Å)	D_{Z-H_2}(Å)	C_g (wt.%)	T_{des} (K)
Zn-MOF-5		-14.39	0.741	2.541	4.78	463.32
Cd-MOF-5	Li_2	-11.06	0.749	2.547	4.45	356.02
Mg-MOF-5		-15.96	0.751	2.540	5.41	513.70
Zn-MOF-5		-11.91	0.740	2.676	4.68	383.39
Cd-MOF-5	Na_2	-9.72	0.741	2.670	4.38	312.87
Mg-MOF-5		-13.72	0.749	2.669	5.27	441.75
Zn-MOF-5		-12.03	0.745	1.952	4.64	387.21
Cd-MOF-5	Be_2	-8.63	0.740	1.950	4.35	277.84
Mg-MOF-5		-12.73	0.750	1.951	5.24	409.83

Table 4.2: The average adsorption energies (kcal/mol), the bond length of H_2 and the adatom distance between Z and H_2, as well as the storage capacities and desorption temperature in unit cell of M-MOF-5:Z_2.

the Z_2-decorated unit cell, calculated from the average adsorption energy by using the equation 4.5, increases to an apogee equal to 513 K for Mg-MOF-5:Li_2 and 463 K for Zn-MOF-5:Li_2 , as shown in Table 4.2. It can be concluded that desorption temperature of the decorated and substituted systems far exceeds the initial decomposition temperature of Zn-MOF-5.

Among the obtained gravimetric densities of hydrogen, we have 5.41, 4.78 and 4.45 wt.% for Li_2-decorated Mg-MOF-5, Li_2-decorated Zn-MOF-5 and Li_2-decorated Cd-MOF-5, respectively. These values concord with the results found in Refs [160, 129, 164].

4.4 Summary and conclusion

In this chapter, different strategies have been applied, in the framework of a unit cell approach, to improve the hydrogen storage properties in MOF-5. The study was carried out using the first principles of density functional theory. The most important results of this work can be summarized as follows: In the first part, we presented a study of adsorption of a hydrogen molecule on MOF-5 based Zn in three sites (metallic, carboxylic and cyclic) with three different orientations. The Zn-MOF-5 has an initial storage capacity of 1.57 wt.% which can increase up to 4.09 wt.% by adsorbing several H_2 molecules. This value doesn't fulfill the targets for hydrogen storage systems set by the US-DoE for on-board vehicular applications, so we have proposed two methods which allowed us to enhance the hydrogen storage properties of this material. Namely i) substitution of Zn by Cd and Mg and ii) decoration by Li, Be and Na. The results show for Li_2-decorated in Mg-MOF-5 an excellent storage capacity up to 5.41wt.% which meet the US-DoE requirement for 2025, with a remarkable improve in the desorption temperature.

Part II

Hydrogen Storage in two-dimensional materials

Chapter 5

2D-boron nitride for improved hydrogen storage applications

5.1 Motivation

Recently, a new 2D carbon monolayer known as t-graphene with a tetragonal symmetry has been predicted through the first-principles calculations. This symmetry is derived from the splitting of two adjacent layers of carbon atoms in bcc C8 or bct C4 along oz-direction [165, 99, 166]. Gu et *al.*, by using C_4K compound as the medium, proposed two novel synthetic routes to achieve planar t-graphene [167], which accelerates the experimental synthesis of this 2D material.
In an interesting study, Majidi [168] have shown that t-graphene-like C–BN and BN sheets exhibit semiconducting properties, where the system stability increases by increasing the number of boron and nitride atoms. In this context, a novel 2D-boron nitride sheet (t-B_4N_4) with a structure similar to t-graphene which is t-B_4N_4 inspired us to study the hydrogen storage properties of this material. t-B_4N_4 is well known for its excellent thermal, dynamical and mechanical stability and has been used for optoelectronic devices such as transparent electrodes [169].

In the first part, we explore the stability of decorated t-graphene by M = Li, Na, K, Ca and Sc atoms at different sites in addition to the adsorption properties of H_2 molecules and its hydrogen storage capacities. In the second part, the stability, electronic and storage properties of H_2 on metal-decorated t-B_4N_4 were investigated. Then, the maximum hydrogen storage capacity and desorption temperature are given by using the van't Hoff equation and results of AIMD simulations. Finally, we compare the H_2 diffusion performance of t-graphene with that of t-B_4N_4 monolayers. The relevant results have been summarized in the conclusion.

5.2 Computational methods and physical quantities

All calculations in this chapter are carried out using the Quantum ESPRESSO package [118], which is based on the density functional theory (DFT). The exchange-correlation potentials in the Kohn-Sham equations were adopted within the generalized gradient approximation (GGA) using the Perdew–Burke–Ernzerhof (PBE) parameterization with projector augmented wave (PAW)[125, 114]. However, the description of the dispersion component of van der Waals interaction, which arises as the electron response to instantaneous charge fluctuation, is missing. For this reason and to improve the chemical accuracy in our calculations, we considered the corrected energy of dispersion by adopting Grimme's approach [170]. The interlayer distance was set to 25 Å in the z-direction, which is enough to minimize the interlayer interactions. An energy cut-off of 40 Ry was used for the plane-wave expansion of the wave function and 400 Ry for the expansion of the augmented charge. All structures were optimized until the residual forces were less than 0.01 eV $Å^{-1}$ per atom. A mesh of 15*15*1 K-points was used via the Monkhorst–Pack scheme [171]. The CI-NEB was applied to determine the minimum energy of a reaction pathway and the energy barrier for both dissociation-chemisorption and desorption processes [146].
Furthermore, ab initio molecular dynamics (AIMD) simulations of the canonical ensemble (NVT) were performed to investigate the thermal stability and desorption processes with a total calculation time of 5 ps and an integration step of 2 fs at temperature ranging from 100 K to 300 K. The calculated thermal stability is valid within the simulated time scale, which is far away from the experimental time scale.
To evaluate the energy stability of our systems, the cohesive energy given as the difference between the sum of the energies of the isolated atoms and the energy of this crystal was computed as follows:

$$E_{coh} = (E_{sheet} - \sum n_X E_X)/\sum n_X \tag{5.1}$$

Where E_{sheet} is the total energy of t-graphene or t-B_4N_4, E_X and n_X are the energy and the number of an isolated atom of type X (X=B, C and N), respectively. The most stable adsorption sites of Li-, Na-, K-, Ca- and Sc-decorated t-graphene and Li-decorated t-B_4N_4 were determined based on the resulting binding energies, which are calculated according to the following equation:

$$E_b = (E_{M+system} - E_{system} - mE_M)/m \tag{5.2}$$

Here, $E_{system+M}$ is the total energy of the decorated t-graphene or t-B_4N_4, m the number of decorative atoms, E_{system} is the total energy of pristine t-graphene or t-B_4N_4, and E_M is the total energy of an isolated metal atom M (M=Li, Na, K, Ca and Sc).

For clear view and more detailed understanding of the adsorption process, we studied the charge density difference of the decorated elements adsorbed at the most favorable site on the monolayer systems, according to equation 5.3:

$$\Delta\rho = \rho_{M@system} - \rho_{system} - \rho_{M} \tag{5.3}$$

where, ρ_{system} and $\rho_{M@system}$ are the electron charge densities of t-graphene or t-B_4N_4 before and after the decoration with M elements, respectively. ρ_M represents the electron charge density of isolated M-atoms in the system by keeping the same lattice parameters obtained after an optimization calculation of the whole M@system. The average adsorption energy (eV/H_2) of hydrogen molecules on M-decorated systems is obtained using the following equation:

$$E_{ads} = (E_{nH_2+mM@system} - E_{mM@system} - nE_{H_2})/n \tag{5.4}$$

Here, $E_{nH_2/mM@system}$ describes to the total energies of mM@sytem monolayer with nH_2 adsorbed molecules, $E_{mM@system}$ is the total energy of metal-functionalized systems, and E_{H_2} is the total energy of an isolated H_2 molecule. m and n denote the number of decorative M-atoms and the number of hydrogen molecules adsorbed in the substrate, respectively. The hydrogen desorption temperature (T_{des}) is crucial and important to release the hydrogen molecules fully from the host systems. Therefore, we used the van't Hoff formula [172] to estimate this quantity:

$$T_{des}(K) = \frac{E_a \times R}{K_B(\Delta S - RlnP)} \tag{5.5}$$

where E_a is the average adsorption energy, R = 8.31 J K^{-1} mol^{-1} is the gas constant, K_B = 1.38 $\times$ 10^{-23} J K^{-1} is Boltzmann constant, ΔS = 130 J $K^{-1}mol^{-1}$ [173] represents the variation of hydrogen entropy from molecular gas to dissolved solid hydrogen and P=1 atm is the equilibrium pressure.

5.3 Results and discussion

5.3.1 Evaluating the stability of M on t-graphene

Due to the role that the metal dopant can play in order to capture hydrogen molecules efficiently, the simulation of decoration by the vdW-DF2 functional was started by the geometry optimization for the adsorption of Li, Na, K, Ca and Sc in different configurations on the t-graphene monolayer. To find the most suitable site for a strong

bond of the M atom with the surface, we considered four possible binding sites such as the center of octal shape (H-1), the hollow-2 site of the square form (H-2), the top of one carbon atom (T) and the top of a C–C bond (B), as shown in Figure 5.1.

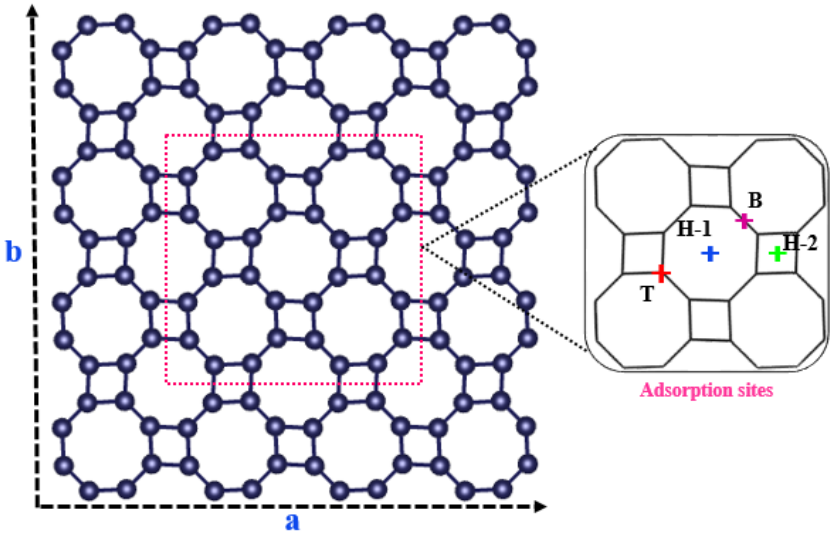


Figure 5.1: Top view of a t-graphene monolayer (4 × 4 supercell) and the studied adsorption sites (denoted as H-1, H-2, B and T).

After optimizing the geometry, we noticed that all the metals decorated on the t-graphene surface choose to be adsorbed onto top of the hollow (H-1), which is the center of the octal shape formed by carbons (see Figure 5.1). We calculated the binding energies of the single atom Li, Na, K, Ca and Sc adsorbed on the favorable site; see Table 5.1.

M@t-graphene	**M=Li**	**M=Na**	**M=K**	**M=Ca**	**M=Sc**
Binding energy (eV)	-2.37	-1.26	-1.69	-2.21	-3.09
cohesive energy Bulk (experimental) [174, 175]	-1.63	-1.11	-0.93	-1.84	-3.90
Distance (Å)	1.77	1.98	2.23	2.11	1.66
Charge (|q|)	0.89	0.87	0.88	1.16	1.35

Table 5.1: Binding energies of M-decorated t-graphene system at the most preferable adsorption site together with those corresponding to the experimental cohesive energies of bulk metals. The optimized distances separating the M atom from substrate and Bader charge acquired by metals.

According to the results of Table 5.1, the obtained values of binding energies -2.37, -1.26, -1.69, -2.21 and -3.09 eV for Li, Na, K, Ca and Sc, respectively are smaller than the corresponding cohesive energies relative to the bulk metal of Li (-1.63 eV), Na (-1.11 eV), K (-0.93 eV) and Ca (-1.84 eV) except for the case of Sc that has a binding energy higher than the experimental cohesive energy of -3.9 eV [176]. These results show that

the agglomeration do not occur in the case of Li, Na, K, Ca@t-graphene. Moreover, our calculated E_b results for the studied materials are larger than those of single-layer biphenylene, and germanium carbide (GeC-MLs) [177, 178].

Since the binding energy of Sc on t-graphene is higher than the experimental cohesive energy of Sc, the possibility of Metal–Metal clustering is not negligible in the Sc-decorated t-graphene system. To be able to verify this possibility, we calculated the energy barriers for the diffusion of the scandium atom from the most preferable adsorption site to other ones using a CI-NEB approach, as shown in Figure 5.2. We found that the diffusion energy barriers for the Sc atom are 0.75 eV, 0.65 eV and 0.67 eV for path 1(a–b), path 2(c) and path 3(d), respectively. Zhang et *al.*[99] reported 0.62 eV, 0.44 eV and 0.51 eV diffusion energy barriers for the Li-decorated t-graphene monolayer for similar pathways. Therefore, the presence of a high diffusion energy barrier can restrict the transition of metal atoms and prevent the system from clustering.

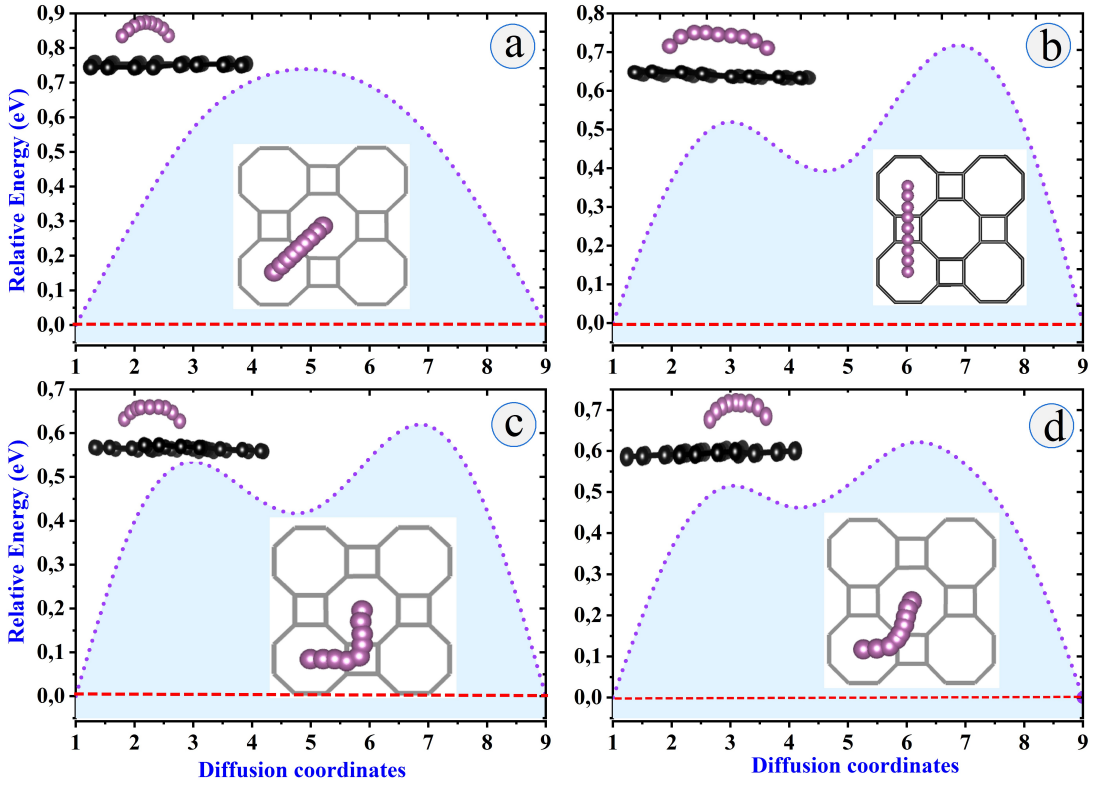


Figure 5.2: (a–d) Relative energy profile for the movement of the Sc atom along four different pathways.

Similarly, we analyzed the charge distribution using the Bader charge algorithm [163]. The results indicate that over the H-1-site, the charged states of Li, Na, K, Ca and Sc atoms are +0.89 |e|, +0.87 |e|, +0.88 |e|, +1.16 |e| and +1.35 |e|, respectively (see Table 5.1). Such electron redistribution conduces to the ionization of M and nearby carbon atoms. The positive charge state of M is beneficial for its anchoring on t-graphene by

means of electrostatic attraction and, in turn, contributes to maintain their dispersive distribution by coulombic repulsion between each other preventing the emergence of agglomeration. The accumulation and depletion of charges are displayed in Figure 5.3(a–e) by plotting the isosurface charge densities for Li, Na, K, Ca and Sc-decorated t-graphene at the most favorable binding site on both sides. We observe a considerable amount of charge transfer from the M-atom to t-graphene, in which the loss and gain of the charge are confirmed, respectively, by the presence of the cyan and yellow color charge density around the M atom and t-graphene substrates. This type of charge transfer phenomena is quite reasonable based on the electronegativity difference between the M atom and the t-graphene monolayer.

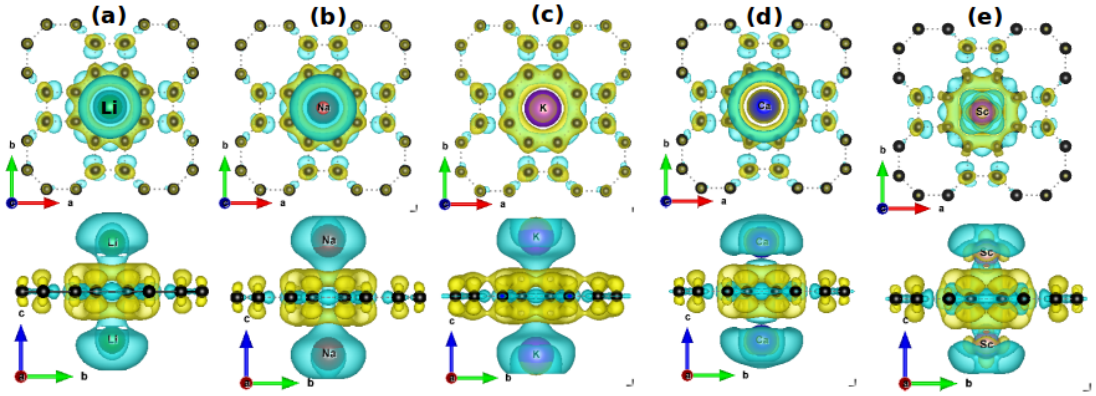


Figure 5.3: Top and side views of isosurface charge densities of M@t-graphene: (a) 2Li, (b) 2Na, (c) 2K, (d) 2Ca and (e) 2Sc. Yellow and cyan indicate the accumulation and depletion of charge, respectively. The chosen isovalue was 0.0023 e/Å^3

Due to its large substrate area, the t-graphene monolayer is expected to be capable of binding a large number of metals, which would result into a high H_2 gravimetric density. In the case of maximum metal atoms on both side (8M@t-graphene), the metals were initially placed on H-1 sites while maintaining a reasonably distance between the two adjacent metal atoms, and then the structures were allowed to fully optimize (see Figure 5.4). By increasing the metal size up to 8M, the E_{bind} values we found for Li, Na, K, Ca, and Sc are -1.73, -1.16, -1.09, -1.90, and -2.57 eV, respectively. Moreover, the distance between nearest neighbour metals in this case was found to be 4.89, 4.87, 4.90, 4.91 and 4.94 Å for 8Li, 8Na, 8K, 8Ca and 8Sc respectively. Although the binding energy increases while increasing the number of metal atoms, the decorated elements are still dispersed on the t-graphene without clustering. This is due to anchoring of M atoms on t-graphene and their mutual repulsive interaction.

After establishing the optimized systems, charge transfer mechanism, and binding energy of the metal-decorated t-graphene monolayer, we now further discuss the adsorption mechanism of H_2 molecules on M-decorated systems. Using equation 5.4, the average

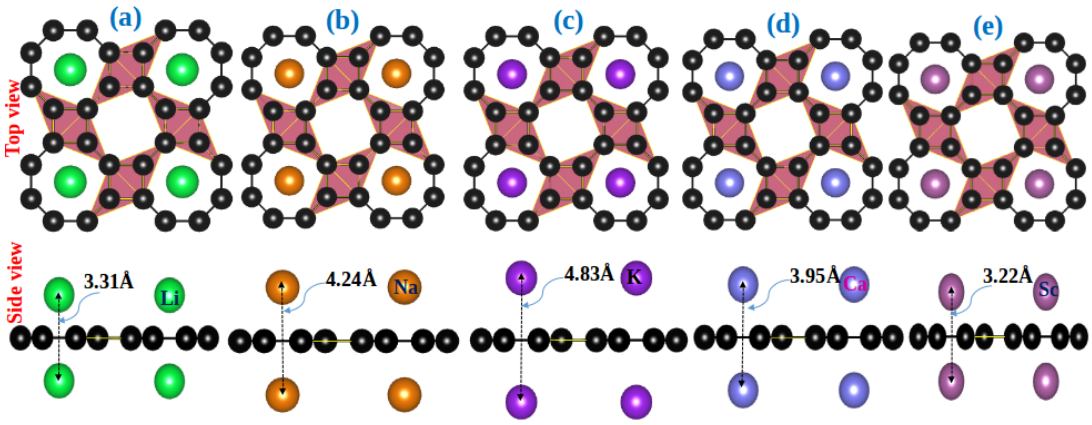


Figure 5.4: Top and side views of the optimized structures of (a) 8Li@t-graphene, (b) 8Na@t-graphene, (c) 8K@t-graphene, (d) 8Ca@t-graphene, and (e) 8Sc@t-graphene. Black, green, orange, magenta, light blue and orchid balls represent C, Li, Na, K, Ca, and Sc atoms, respectively

adsorption energies of hydrogen molecule are listed in Table 5.2 along with the distance between the H_2 molecule and the nearest metal (M), the H-H bond length and the gravimetric capacities for all hydrogenated systems in their optimized geometries.

mM-nH_2	E_{ads} **(eV/H_2)**	d_{H-H}	D_{M-H_2}	C_g**(wt.%)**	T_{des}**(K)**
1Li-3H_2	-0.161	0.751	2.26	1.52	119.47
8Li-20H_2	-0.192	0.756	2.49	8.41	142.48
1Na-4H_2	-0.156	0.761	2.18	1.94	115.76
8Na-20H_2	-0.172	0.768	2.53	6.63	127.63
1K-3H_2	-0.154	0.758	2.23	1.41	114.28
8K-20H_2	-0.166	0.760	2.47	5.47	123.18
1Ca-3H_2	-0.159	0.759	2.51	1.40	118.01
8Ca-20H_2	-0.181	0.763	2.76	5.42	134.31
1Sc-4H_2	-0.153	0.760	2.63	1.84	113.53
8Sc-19H_2	-0.165	0.767	3.19	4.90	122.44

Table 5.2: The results of the average adsorption energies of nH_2/mM@t-graphene, the H-H bond length, the distance between M and the hydrogen molecules H_2 and a hydrogen gravimetric density (wt.%)

By adding H_2 one by one for adsorption on the M-decorated system, we found that one atom of Na or Sc can adsorb a maximum of four molecules of hydrogen while three molecules H_2 can be adsorbed by one atom of Li, K or Ca with reasonable average energies (see Table 5.2). Once this maximum is exceeded, the extra hydrogen molecules moved away from the metal elements. In case of the highest Li/Na/K/Ca concentration on both sides, the systems could adsorb up to 20 H_2 molecules within adsorption energies located in the desired range for H_2 storage [179, 180]. For the case of 8Sc@t-graphene, the system reaches saturation for 19 H_2 hydrogen molecules, while remaining stable without

observing any structural deformation. The maximum gravimetric capacities for the 8Li-, 8Na-, 8K-, 8Ca@t-graphene and 8Sc@t-graphene systems are 8.41, 6.63, 5.47, 5.42 wt.% and 4.90 wt.%, respectively. These estimated results, especially for the case of 8Li@t-graphene, are greater compared to ones of the decorated 2D materials studied previously for hydrogen storage [100, 181, 182].

Compared to the computational work previously carried out and the rapid development of the exploration of the 2D structure, we found that this monolayer t-graphene does not exhibit adequate hydrogen storage properties, in particular the desorption temperature. However, it has recently been observed that structures with B and N atoms are energetically more favorable. Meanwhile, extensive research on the h-BN monolayer, graphitic carbon nitride and boron carbide monolayer as potential reversible systems for hydrogen storage mobile applications [183, 184, 185] motivated us to study the t-B_4N_4 system with a structure similar to t-graphene for the next generation as a potential substrate candidate for hydrogen storage.

5.3.2 Stability/Adsorption of Li on t-B_4N_4 monolayers

Before assessing the stability of the Li-decorated t-B_4N_4 system. it is important to start by geometrical optimization to get the most stable structure of the t-B_4N_4 monolayer, as shown in Figure 5.5. This system is composed of 32 atoms of which the unit cell of t-B_4N_4 contains four boron (B) and four nitride (N) atoms. Our t-B_4N_4 monolayer, which is a (2×2×1)-super cell, is made up of four- and eight-membered rings. The four-membered rings have B–N bond lengths of 1.47 Å and bond angles of 83.261° and 96.731°, while the eight-membered rings consist of two types of B–N bonds with bond lengths of 1.49 and 1.39 Å and bond angles of 140.121° and 129.171°, respectively.
The relaxed lattice constant of the monolayer t-B_4N_4 are a=b=4.9442 Å, which is in accordance with the previous reported works [168, 169]. According to our simulation, the cohesive energies of -7.02 eV/atom and -5.87 eV/atom have been defined for t-B_4N_4 and t-graphene structures respectively [168]. Although the mentioned two structures are stable, by comparing their cohesive energies, we can see that the network between B and N atoms is strongly correlated. This finding underpins our rationale in selecting a t-B_4N_4 monolayer to improve the decoration process and hydrogen storage properties compared to the t-graphene system.
According to what has been mentioned before and due to its light weight, we first start by optimizing the adsorption of a Li atom onto the surface of t-B_4N_4 which is a prime candidate for the surface decoration of 2D materials used for hydrogen storage. Geometric relaxation reveals that the optimal position of Li adsorption turns out to be the hollow site (H-1) above the center of octagon, as shown in Figure 5.5.

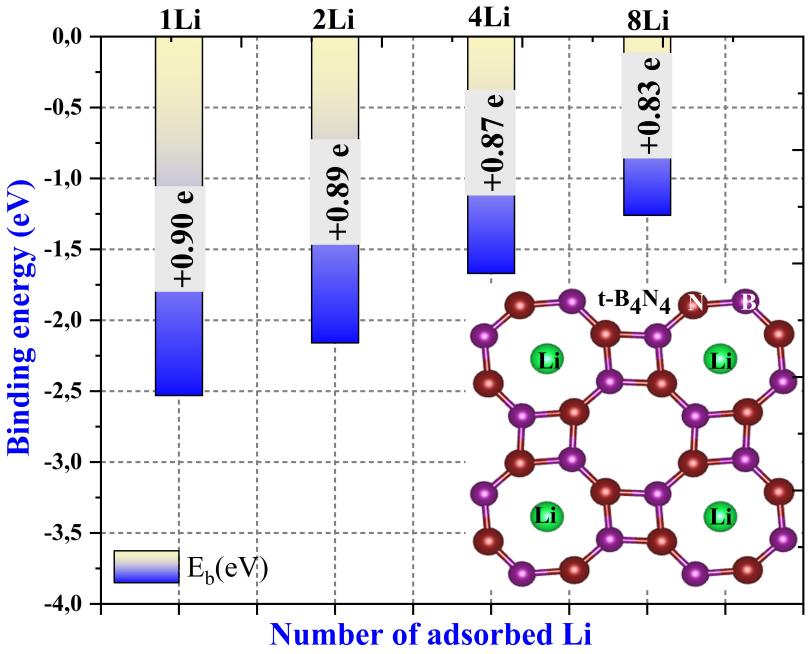


Figure 5.5: The variation in the calculated binding energy of adsorbed nLi@t-B_4N_4 monolayer.

The calculated binding energy of a single Li atom on the system was obtained as -2.53 eV with a distance separating the Li atom from the t-B_4N_4 surface of 1.64 Å (see Figure 5.5). Hence, the binding strength for a Li atom on t-B_4N_4 is stronger than that on t-graphene (-2.37 eV per Li), carbon nitride (-1.54 eV per Li) and $B_{16}N_{16}$ (-0.67 eV per Li)[100, 185, 186].

As indicated in the first part, to obtain a high gravimetric density with an improved affinity for hydrogen molecules, we dope the substrate with Li metals for different concentrations. Four doping concentrations to both sides of the H-1 site have been considered, which are as follows: one, two, four and eight Li atoms adsorbed on both sides of the t-B_4N_4 monolayer. The nearest Li–Li distance is about 4.93 Å, which is larger than that on the other 2D materials [187, 89]. It is obvious that by increasing the number of Li atoms, the charge transfer monotonically decreases from 0.90 to 0.83 e (see Figure 5.5). The binding energy results show a significant increase to -1.26 eV for the case of 8Li@t-B_4N_4, as shown in Figure 5.5 due to the repulsive interaction between positively charged lithium atoms [100].

To gain a deeper understanding of the interactions between Li atoms and the t-B_4N_4 monolayer, the distribution charge density differences of the optimized Li adsorption on the most favorable site of t-B_4N_4 are shown in Figure 5.6(c). The green and pink zones represent the charge accumulation and depletion around the Li atoms adsorbed onto the t-B_4N_4 substrate, respectively. Meanwhile, the charge transferred from the first Li decreases from 0.90 to 0.83 e leading to a weakening of the electrostatic attraction with the

host material, which is in accordance with the trend of the binding energies previously found.

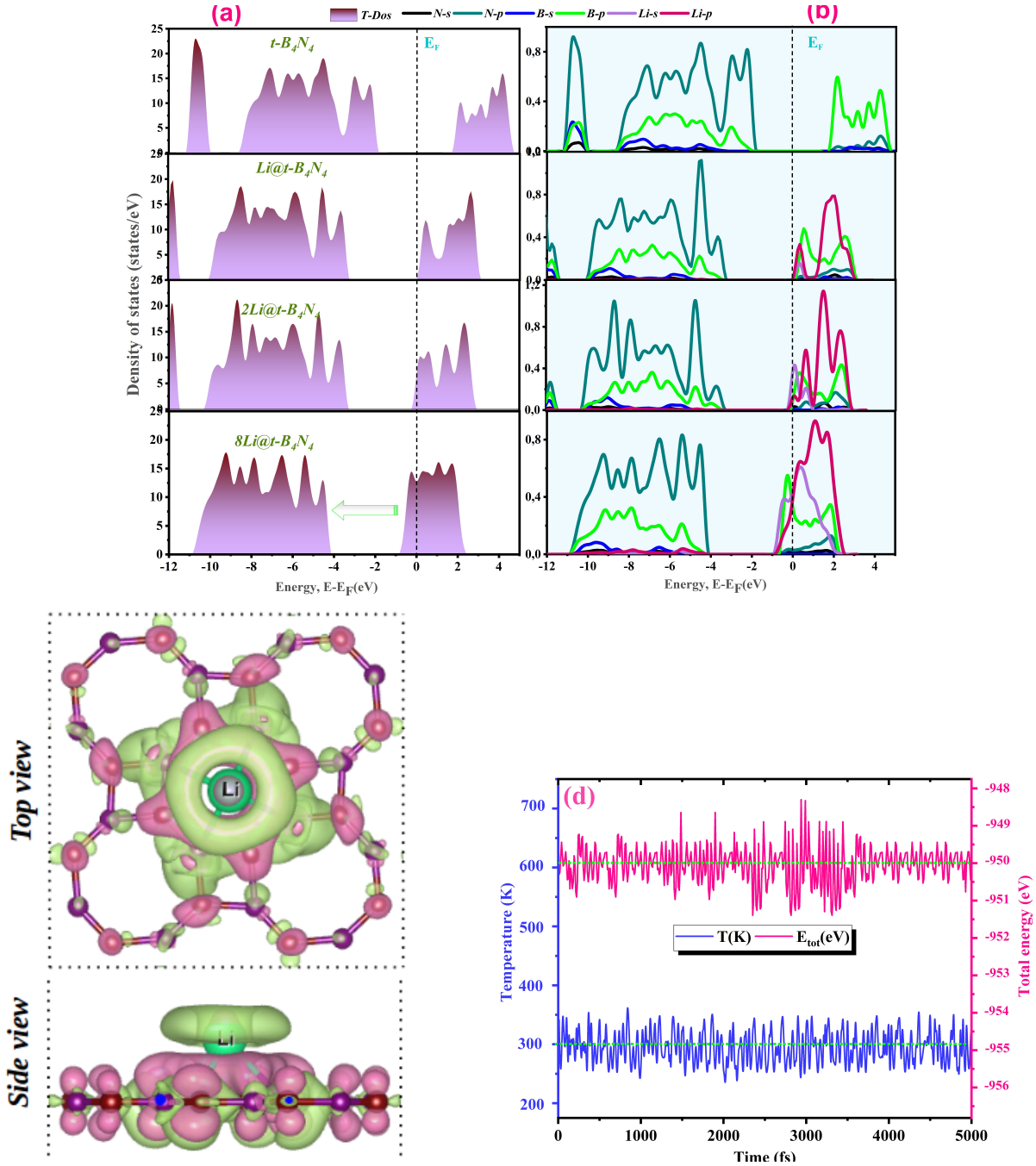


Figure 5.6: T-DOS (a) and P-DOS (b) of t-B_4N_4 monolayer, Li@t-B_4N_4, 2Li@t-B_4N_4 and 8Li@t-B_4N_4. (c) Top and side views of the isosurface charge density plot for the Li-functionalized t-B_4N_4 sheet. The isosurface level was set to 0.0039 $e/Å^3$. (d) MD simulations of the Li atoms functionalized systems.

The density of state for t-B_4N_4 before and after Li atom adsorption is shown in Figure 5.6(a and b). We point out that the clean t-B_4N_4 system exhibits a semiconductor behaviour with an electronic band gap of 3.89 eV, similar to the t-BN, c-BN and h-BN

monolayers,[183, 169, 188] while after the incorporation of Li atoms, the material has gained a metallic character. Based on the PDOS of the clean t-B_4N_4 system, it can be clearly seen that the major contribution to VBM and CBM comes from the p-orbitals of B and N atoms. After decoration, the peaks of hybridized orbits between Li-p and B-p are mainly located at about 1 eV above the Fermi energy and result in Li atoms strongly bound with t-B_4N_4. In the interval of -1.0 to 0.0 eV, the peaks of the orbits of B-p and Li-s atoms also overlap, meaning that the strong interaction occurs between B and Li atoms.

After verifying the binding mechanism of the lithium dopant on the t-B_4N_4 surface, we have performed ab initio molecular dynamics (MD) simulations at 300 K to study and confirm the structural stability of our system (see Figure 5.6(d)). As shown in Figure 5.6(d), we can see that there are small variations in the total energy of the 8Li@t-B_4N_4 system at room temperature,which implies the thermal stability of the decorated system throughout the MD calculations. Overall, the introduction of Li atoms causes only a small distortion of the geometric structure without breaking bonds in the system.

To sum up, the results of Li-adsorption phenomena can be summarized as follows: (i) Li atoms can adsorb onto the t-B_4N_4 monolayer with a strong binding energy and (ii) the system has very good thermal stability at 300 K even at high Li-doping concentrations.

5.3.3 Hydrogenation of nLi@t-B_4N_4 system

As indicated previously, the decoration of lithium atoms at different concentrations on the surface of the system remains among the successful methods for enhancing the adsorption of H_2 molecules by the polarization process [189, 190]. Thus, we start first by optimizing the adsorption of hydrogen molecules near the Li atoms on the t-B_4N_4 monolayer. According to our simulation, Figure 5.7(a–c) displays the optimized geometries of the H_2 molecules adsorbed on Li@t-B_4N_4 for different concentrations of Li.

First, the adsorption energy is -0.308 eV for the first hydrogen adsorbed on Li@t-B_4N_4 with an inter-distance between H_2 and the substrate of 2.17 Å. By adding additional H_2 molecules, we can see that the system can adsorb up to four H_2 molecules in the vicinity of the single Li atom in its stable position with an acceptable average energy of -0.157 eV (see Fig 5.7(a)). However, it is evident that the average adsorption energy decreases as the number of H_2 increases from 1 to 4 in the Li@t-B_4N_4 system with a corresponding gravimetric capacity of about 1.95 wt%. Then, for double-sided Li (2Li@t-B_4N_4), the average adsorption energies varied between -0.294 and -0.163 eV for the system with a gravimetric density of 3.77 wt%, as shown in Figure 5.8(b). At last, to estimate the maximal storage gravimetric density of this system, we have filled all the available stable sites with Li atoms (8Li@t-B_4N_4) to catch as many hydrogen molecules as possible.

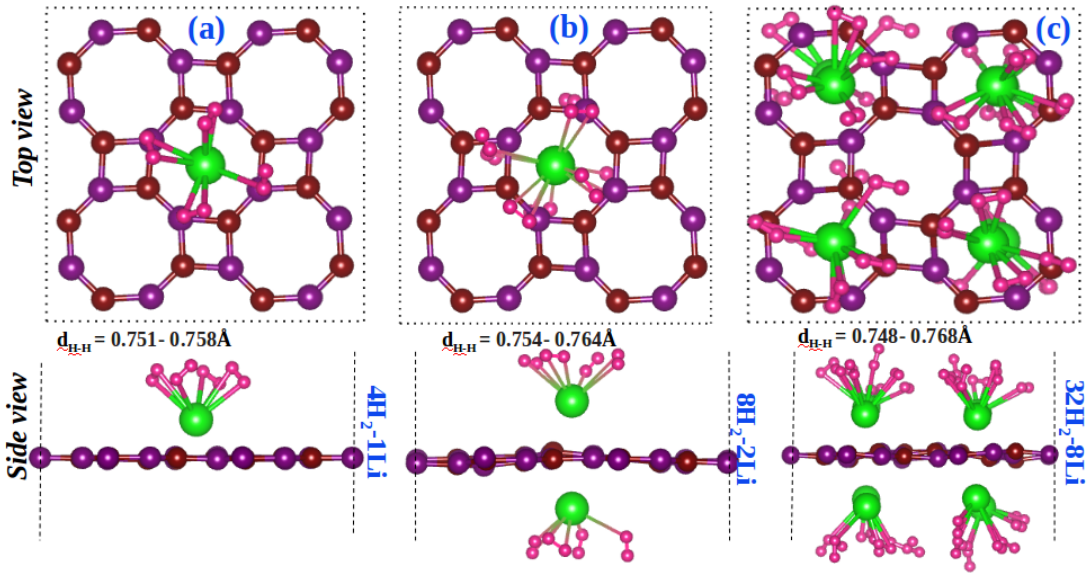


Figure 5.7: (a-c) Top and side views the hydrogen adsorption at different concentrations of Li on t-B_4N_4 system.

From Figure 5.8(c), it was found that the system can adsorb up to $32H_2$ before the deformation of the system with average H_2 adsorption energies in the range beteween -0.386 and -0.217 eV [191, 192, 182]. Once the system 8Li@t-B_4N_4 reaches the saturation, the resulting gravimetric capacity reaches 12.47 wt%, and this value is higher than that of many typical 2D materials such as Li@t-graphene (7.7 wt%), Li@$B_{16}N_{16}$ (9.15 wt%) and Li@boron hydride (11.57 wt%).

In what follows, we discuss the desorption temperature of the most promising system $32H_2$/8Li@t-B_4N_4 using equation 5.5. Overall, T_{des} plays an important role in determining the thermal stability of the $32H_2$/8Li@t-B_4N_4 system regarding the charge/release process of H_2 molecules. By using an equilibrium pressure of 1 atm and the average adsorption energy, the maximal desorption temperature is equal to 161.03 K for 8Li-decorated t-B_4N_4 monolayer [193, 194, 195]. This value is twice higher than the boiling point of liquid nitrogen (77 K), and higher than the desorption temperature of Li@t-graphene T_{des} = 142.48, as obtained in *section*5.3.1.

5.3.4 Thermodynamical stability

AIMD simulations were performed for the hydrogenated 8Li@t-B_4N_4 system with the highest gravimetric capacity (see Fig 5.7 (c)) to verify the desorption temperature estimations at different temperatures T = 100, 200 and 300 K, as shown in Figure 5.9. Figure 5.9 show the side views of the structures containing hydrogen molecules after the AIMD simulation with effective bonds between Li-atoms and H_2. The Li-H_2 distances greater than 2.5 Å are represented in dark blue color and distances less than 2.5 Å are

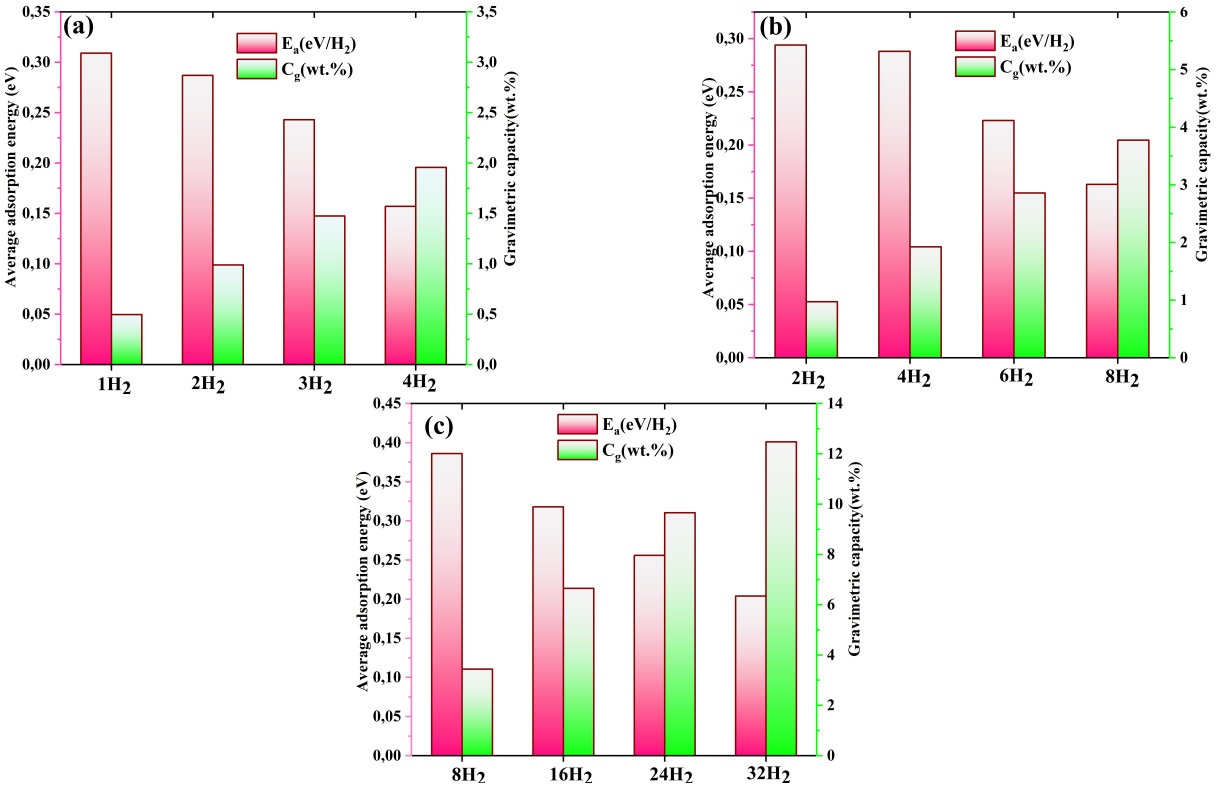


Figure 5.8: Average adsorption energy ($|E_{ads}|$) and hydrogen gravimetric density in t-boron nitride systems with different Li concentrations: (a) 1Li@t-B_4N_4, (b) 2Li@t-B_4N_4, and (c) 8Li@t-B_4N_4

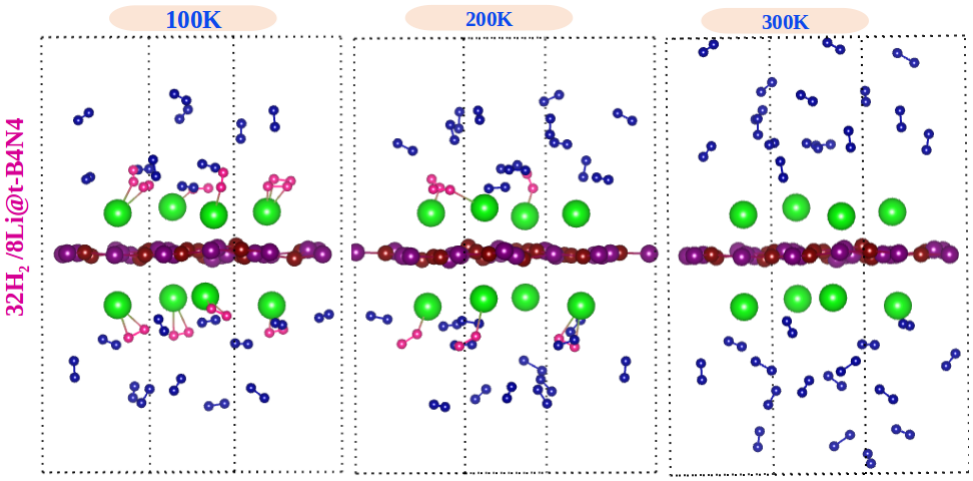


Figure 5.9: 32H_2/8Li@t-B_4N_4 system as obtained at the end of 5000 fs AIMD simulations at different values of temperatures: (a) 100 K; (b) 200 K; (c) 300 K. B, N and Li are represented by brown, purple and green balls respectively. Light pink and dark blue represent H_2 molecules with a distance from the Li atom less than and more than 2.5 Å, respectively.

colored in light pink. We first start simulations at T= 0 K, showing that all the hydrogen molecules remain near 8Li@t-B_4N_4. Once the temperature rises, hydrogen molecules

begin to migrate noticeably far away from Li-atoms and t-B_4N_4 sheets. Then, at 300 K, a maximum number of hydrogen molecules have moved far enough away from the t-B_4N_4 monolayer decorated with Li.

5.3.5 Single H_2 molecular diffusion

Apart from the high gravimetric density, the fast diffusion of hydrogen molecules in two-dimensional materials moving across the surface is crucial for the development of next generation energy storage devices. The H_2 kinetics was investigated by calculating the activation barriers using the CI-NEB method.

As is known, to get the activation barriers or to determine the most optimal diffusion path of the hydrogen molecule on the surface of t-graphene and t-B_4N_4 monolayers, the CI-NEB method is an important and efficient method, which is used to determine the minimum energy path (MEP) between the initial physisorption state and a given final transition state, as described pictorially in Figure 5.10.

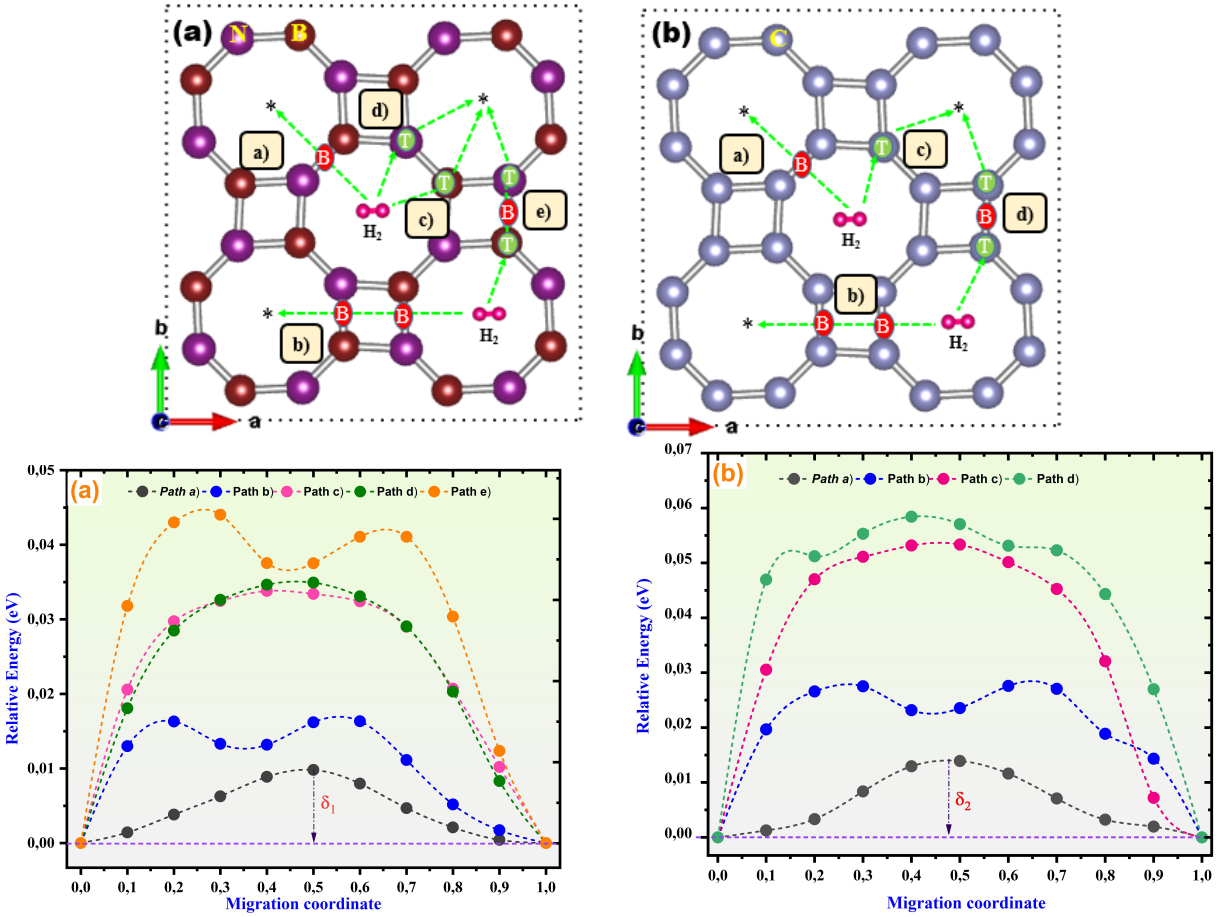


Figure 5.10: Single hydrogen molecule migration pathways and the corresponding barrier energies on the systems: (a) t-B_4N_4 and (b) t-graphene.

The obtained results of diffusion energy by different typical H_2 diffusion paths for t-B_4N_4

and t-graphene are shown in Figure 5.10(a) and (b), respectively. We can observe in both systems that the hydrogen molecule diffuses easily via pathway "a". The minimum diffusion barrier is $\delta_1 = 0.0098$ eV for t-B_4N_4 and $\delta_2 = 0.0136$ eV for t-graphene. For comparison purposes, our result for the barrier energies (δ_1 and δ_1) of path 'a' that are illustrated in Figure 5.10 are rather low compared with the value of 0.014 eV in 2D-graphene reported by Arellano et al.[196]. It is worthwhile to mention that although we have only considered path (a), the same trend is observed for the other paths. Finally, we may deduce that according to the evaluation of the kinetics performance of H_2 molecules on t-graphene and t-B_4N_4 monolayers, the surface of t-B_4N_4 is more favorable for hydrogen molecule diffusion than that of t-graphene.

5.4 Summary and conclusion

In this chapter, a novel two-dimensional t-graphene-like boron nitride monolayer has been studied for hydrogen storage applications due to its interesting properties. Via DFT-based calculations, first, the structural, electronic, metal binding and hydrogen adsorption characteristics of Li-, Na-,K-, Ca- and Sc-decorated t-graphene were analyzed. Then, a t-graphene-like t-B_4N_4 sheet was constructed by replacing half of carbon atoms with B atoms and the rest with N atoms. Our results indicated that the t-B_4N_4 monolayer combines three important advantages. The first one is that the Li atom adsorbed at the center of the octagon on the t-B_4N_4 monolayer has a strong binding energy of -2.53 eV and excellent thermal stability even for a high Li-doping concentration at 300 K, as verified using ab initio molecular dynamics simulations. The second one is that the Li-decorated t-B_4N_4 monolayer adsorption energy is higher than that of the Li@t-graphene material, and the resulting system can adsorb up to 32 hydrogen molecules H_2 to reach a maximum hydrogen storage capacity of 12.47 wt%. The last one concerns the H_2-molecule diffusion kinetics, the diffusion barriers of which are 0.0098 and 0.0136 eV for t-B_4N_4 and t-graphene, respectively, showing that the hydrogen molecule can diffuse easily through the t-B_4N_4 surface compared to t-graphene.

Chapter 6

Design of 2D-Be_2C as high capacity and reversible hydrogen storage media

6.1 Motivation

Among different storage routes, 2D material-based H_2 storage seems to be the most sustainable option provided a suitable material is available, which meets the criteria proposed by US Department of Energy.

2D beryllium carbide (Be_2C) monolayer, which has been studied in several applications [197, 198, 199, 200] and initially inspired by its 2D-BeB_2 counterpart [201], is expected to hold much higher gravimetric hydrogen density because of its lower relative atomic size, and its multiple active sites to uptake hydrogen according to previously conducted computational study[202]. On the other hand, Long Chen et al.[203] demonstrated by using first-principles calculations that H_2 molecules adsorb more strongly on Li-decorated Be_3C_2 monolayer due to the polarization of H_2 molecules induced by the electric field produced by the Li@Be_2C monolayer dipole. As a result, Li@Be_2C can store up to 14 hydrogen molecules (H_2) with an average adsorption energy of (-0.20; -0.26 eV)/H_2, resulting in a maximum gravimetric hydrogen density of 10.79$wt.\%$.

In this chapter, we have performed a comprehensive study to explore the structural and thermal stability of Be_2C system using ab-initio molecular dynamics (AIMD) simulations. The decoration effect of the alkali (Li, Na, and K) and alkaline-earth (Mg) elements on the adsorption mechanism of H_2 molecules on the surface of 2D-Be_2C has been investigated. Finally, a high coverage adsorption of H_2 molecules on the M-decorated structures is carried out predicting a high hydrogen gravimetric density. In addition, we estimated the H_2 desorption temperatures by using the van't Hoff equation and AIMD calculations

to explore the reversibility of adsorbed hydrogen at the range of temperature.

6.2 Models and simulation details

All the steps of these calculations were performed using Density Functional Theory (DFT)and the projector-augmented wave (PAW) method as implemented in the simulation code Quantum Espresso[118].The exchange-correlation potential was treated within the generalized gradient approximation (GGA) due to Perdew-Burke-Ernzerhof (PBE)[125, 114]. The van der Waals (vdW)method with the self-consistent correction scheme of vdW-DF-ob86 has been used for a better description mechanism of interaction between the substrate and the hydrogen molecules. The wave functions are expanded in a plane wave basis, the size of which is defined by the kinetic energy cut-off of 560 eV, 15×15×1 k-points set for the unit cell and 10×10×1 k-points set for the (3×3)-cell system, and the total energy convergence criteria in the self-consistent field iteration of 10^{-8} eV with the forces energy a 0.01 eV/Å.
For DFT simulations, we considered a Be_2C unit cell, which contained three atoms (1 C and 2 Be), and a (3×3×1) supercell, which contained 27 atoms (9 C and 18 Be). The Be_2C structure was decorated with metal dopants Li, Na, Mg and K. The optimal vacuum space along the z-direction is found to be as large as 20 Å to avoid interactions between imaginary images. Further increasing of the vacuum was found to have only negligible consequences on the results but with greater computation expenses. Finally, ab-initio molecular dynamic (AIMD) simulations of 20 ps with a time step of 1 fs at 298 K within the canonical ensemble (NVT) were employed to examine the thermal stability of the Be_2C system.

6.3 Results and discussion

6.3.1 Crystalline and electronic properties of monolayer Be_2C

We first start by discussing the structural properties of the optimized Be_2C monolayer as shown in Figure 6.1(a). From side view, Be_2C monolayer crystallizes within the P-3m1 space group in the form of a hexagonal structure similar to that of graphene but with three atomic layers along the z direction, the upper and lower layers are Be atoms, and the middle one layer is C atoms. According to the DFT/vdW-DF-ob86 approximation, the calculated interlayer distance between the two Be layers is d= 0.91 Å while the lattice constants are found to be a=b= 2.98 Å, in agreement with previous studies [200]. Each C atom is bonded with six Be atoms while each Be atom is bonded with three C atoms. The optimized Be-Be and Be-C bond lengths are 1.98 and 1.73 Å, respectively.

As for its structural stability, the cohesive energy of pristine Be_2C was evaluated using the following equation:

$$E_{coh} = (E_{Be_2C} - nE_C - 2nE_{Be})/3n \tag{6.1}$$

where E_{Be_2C} is the total energy of a Be_2C sheet, E_{Be}, E_C and n are the energy and number of individual C and Be atoms, respectively. According to our computations, Be_2C monolayer (Figure 6.1(a)) has a cohesive energy of -5.78 eV/atom, indicating the energetic stability of the Be_2C structure. This is in alignment with other 2D materials such as graphene [204], BeC monolayer [205], silicene [206] and phosphorene [207] where the cohesive energies are of -7.95, -6.67, -4.57 and -3.71 eV/atom, respectively. We have further calculated the phonon spectrum in order to justify the dynamical stability of the considered monolayer.

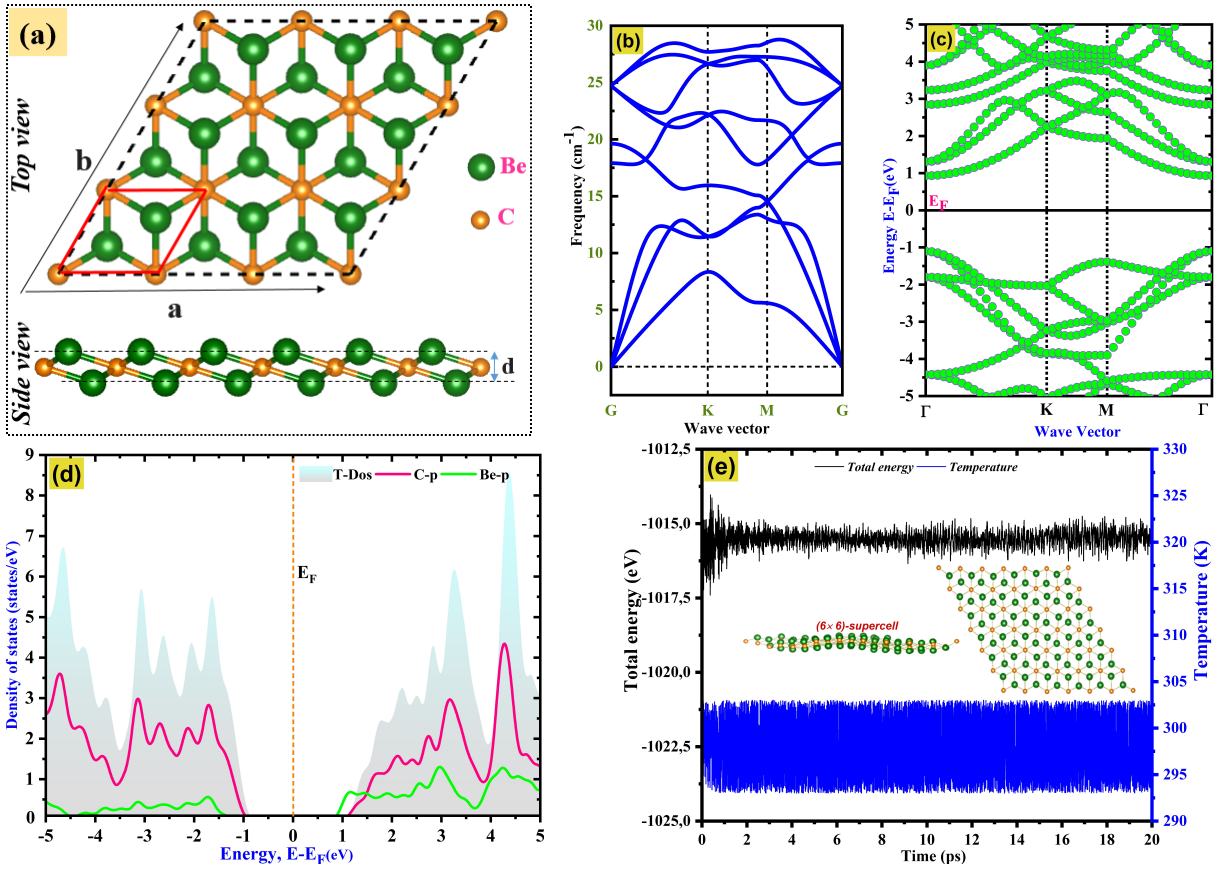


Figure 6.1: (a) Top and side views of relaxed Be_2C monolayer, (b) the phonon spectra, (c) band structure, (d) total and partial density of state, and (e) variation of the total-energy and temperature between 0 and 20 ps during AIMD simulations at 298 K and the corresponding top and side snapshots of 2D Be_2C monolayer.

As illustrated in Figure 6.1(b), it is clearly seen that there are no imaginary modes in the phonon spectra which confirms the dynamical stability of Be_2C. The electronic band

structure in Figure 6.1(c) demonstrates that monolayer Be_2C exhibits a semiconducting behavior with a direct band gap of around 1.76 eV with the valence band maxima (VBM) and the conduction band minima (CBM) located at center of the Brillouin zone (point). These results are in agreement with previous studies [200]. Furthermore, the projected density of states (P-DOS) in Figure 6.1(d) shows that near the Fermi level, VB and CB of the Be_2C monolayer mainly consist of the C-p and Be-p orbitals. Especially, the p states of C atom are strongly hybridized in both bands of Be_2C monolayer. Prior to study the hydrogen adsorption, it is essential to validate the thermal stability of the host material. For that, we employ AIMD calculations to evaluate the thermal stability of a (6*6) Be_2C monolayer supercell at room temperature of 298 K through a run of 20 ps. The snapshot in Figure 6.1(e) shows that the Be_2C monolayer does not break throughout the simulation with only small fluctuations in the vertical direction of the sheet, thus, confirming that monolayer Be_2C has very good thermal stability.

6.3.2 H_2 adsorption on pristine Be_2C monolayer

To better advance in our study, it is important to investigate single adsorption of a hydrogen molecule on the surface of Be_2C monolayer. Six adsorption sites are identified in this system as shown in Figure 6.2(a), namely: TBe1-site (top of the upper Be atom), TC-site (top of the C atom), B-site (bridge formed between C and lower Be atoms), H1-site (triangle formed between the upper and lower Be and C atoms), H_2-site (bridge formed between the upper and lower Be atoms; not to confuse with H_2 molecule) and TBe2-site (top of the lower Be atom). The adsorption sites are similar to what has been identified in the literature [202]. Accordingly, we calculated the adsorption energy (E_{ads}) of a single H_2 molecule adsorbed on the most favorable adsorption sites (B, TC and TBe1/2) of a Be_2C surface by taking into account a distance variation between the substrate and the mass center of the H_2 molecule (from 2.40 to 4.00 Å as marked in Figure 6.1(b) until we get the lowest E_{ads} of the H_2-surface distance). The average and successive adsorption energy per H_2 molecule were calculated as follows:

$$E_{ads} = (E_{nH_2+Be_2C} - E_{Be_2C} - nE_{H_2})/n \tag{6.2}$$

$$E_s = E_{nH_2+Be_2C} - E_{(n-1)H_2+Be_2C} - E_{H_2} \tag{6.3}$$

Here, n is the number of H_2 molecules, $E_{nH_2+Be_2C}$, E_{H_2}, $E_{(n-1)H_2+Be_2C}$, and E_{Be_2C} are the total energies of nH_2 molecules adsorbed on Be_2C structure, single H_2 molecule, (n-1)H_2 molecules adsorbed on Be_2C monolayer, and pure Be_2C system, respectively. The E_{ads} of a single H_2 molecule using the vdW-DF-ob86 correction is calculated and presented in

Figure 6.2.

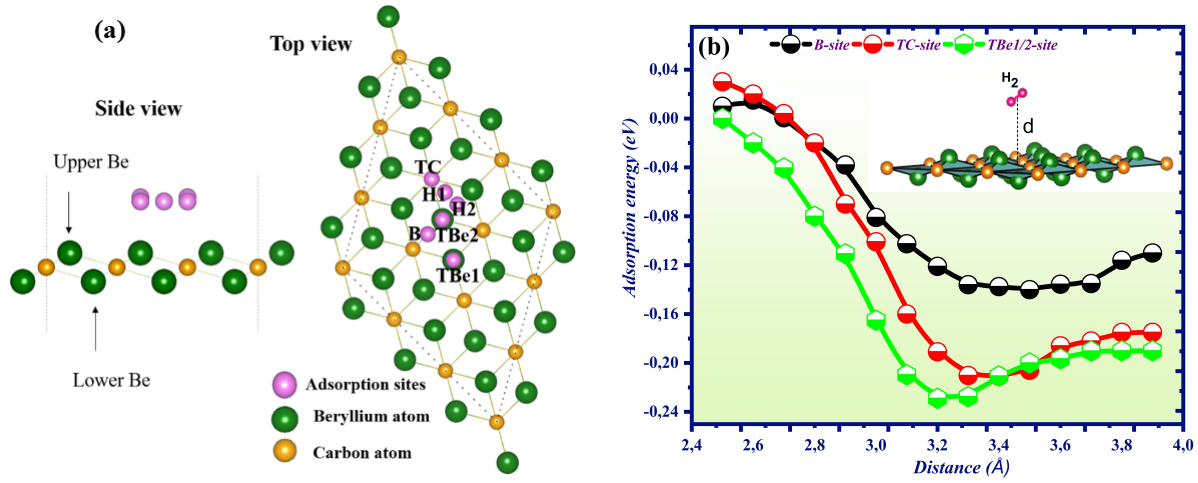


Figure 6.2: (a) Side and top views of different adsorption sites, (b) the calculated adsorption energies at the three most preferable sites as a function of the H_2-Be_2C distance.

Figure 6.2(b) summarizes the adsorption energies of a single hydrogen molecule adsorbed on the Be_2C substrate at the most favorable adsorption sites. The optimal distance between the molecule and the surface was obtained by taking into consideration vdW interactions. We note that the B, TC and TBe1/2 adsorption sites have the most stable adsorption energies with values of -0.140, -0.210 and -0.228 eV and adsorption distances of 3.51, 3.73 and 3.25 Å, respectively. These adsorption energies are more stable than those of some previously explored 2D materials [208, 193]. Besides, the calculated H-H bond distance separating two hydrogen atoms within an adsorbed H_2 molecule are around 0.742–0.749 Å, in well agreement with the experimental value of 0.74 Å for a hydrogen molecule [209]. To understand the bonding mechanism of the interactions between the participating hydrogen molecule and the adsorption surface, it is necessary to calculate the densities of states of a single hydrogen molecule in the most favorable adsorption sites on the Be_2C monolayer, as shown in Figure 6.3.

According the topological analysis, it can be observed that the H-s orbital mainly overlaps with Be-p/C-p atoms between -8 eV and -6 eV in valence band and indicates the strong and stable adsorption of H_2 in the three sites. The overlap difference between adsorption sites has been visualized in the interior frame. In one hand, the H-s state peak in site TBe1/2 is higher compared to the other sites (TBe1/2>TC>TB). Furthermore, as we know that the more the electronic states are towards the valence band (negative energies), the more the material is thermodynamically stable. As shown in P-DOS, the H-s electronic state peak moves to the negative energies in TBe1/2 site compared to TC and TB sites leading to a superior stability of H_2 in TBe1/2 site, indicating that the TBe1/2 site is the most preferable for hydrogen storage adsorption in Be_2C substrate. Based on

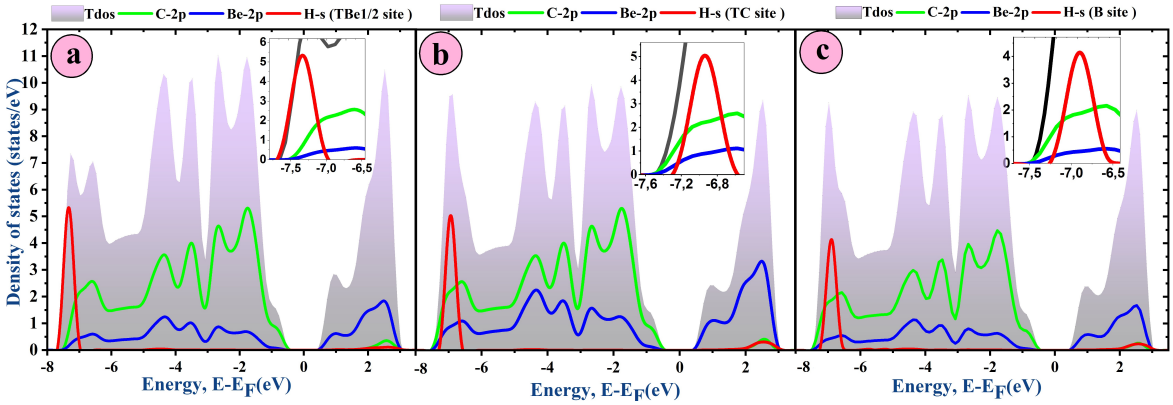


Figure 6.3: DOS of single adsorption of a hydrogen molecule on pristine Be_2C in the (a) TBe1/2, (b) TC and (c) B adsorption sites.

the adsorption results of a single H_2 molecule on Be_2C monolayer, we can conclude the maximum number of hydrogen molecules to be adsorbed on the surface as summarized in Table 6.1.

n	E_s **(eV)**	E_{ads}**(eV/**H_2**)**	**D(Å)**	d_{H-H} **(Å)**
$1H_2/Be_2C$	-0.228	-0.228	3.25	0.742
$2H_2/Be_2C$	-0.230	-0.229	3.18	0.745
$4H_2/Be_2C$	-0.216	-0.221	3.05	0.746
$6H_2/Be_2C$	-0.208	-0.219	2.96	0.751
$8H_2/Be_2C$	-0.198	-0.201	2.65	0.750
$10H_2/Be_2C$	-0.168	-0.189	2.43	0.749
$11H_2/Be_2C$	-0.153	-0.161	2.14	0.744

Table 6.1: The successive and average adsorption energy (E_s and E_{ads}) per H_2, the average distances between H_2 and Be_2C monolayer (D) and adsorbed hydrogen distance (H-H)

Using equation 6.2, we gradually increased the number of H_2 molecules on both sides of the Be_2C substrate and found, based on the optimization results, that this system can adsorb up to 11 H_2 molecules without any structural deformation while keeping the successive H_2 adsorption energy values in the range between -0.153 and -0.228 eV as shown in Table 6.1. The average hydrogen interaction and successive adsorption energy values indicating that the adsorbed H_2 molecules in Be_2C-$11H_2$ are reversible at ambient conditions. Consequently, we can calculate that the hydrogen storage weight percentage of this structure is about $6.7wt.\%$. Our calculated gravimetric capacity exceeds the recommended minimal value proposed by the US-DoE and most of other 2D-materials such as B_2C-graphene, t-SiC, and $2D - Si_2BN$ [187, 210] In what follows, we will employ a novel strategy to improve the hydrogen storage capacity of the system by studying the hydrogen adsorption on a metal-decorated Be_2C.

6.3.3 Metal decoration of Be_2C monolayer

To investigate the effect of metal decoration [211] on the hydrogen storing capability in our material, we first started by adsorbing a single metallic atom (Li, Na, K and Mg), equivalent to metal-coverage 3.57%, on the adsorption sites shown in Figure 6.2(a). After carrying out a full structure optimization, we calculated the average binding energy of an individual M-atom decorated on the Be_2C monolayer as determined by the following equation:

$$E_b = (E_{mM@Be_2C} - E_{Be_2C} - mE_M)/m \tag{6.4}$$

where, $E_{M@Be_2C}$ denotes the lowest total energy of metal-decorated Be_2C sheet, E_{Be_2C} stands for the lowest total energy of freestanding Be_2C nano-sheet and E_M is the lowest total energy of isolated single metal (M= Li, Na, K, Mg). m denotes the number of decorative atoms. An E_b<0 refers to an exothermic reaction, revealing attractive characteristics of host material towards the guest metal, which is a key factor for a 2D material to be successfully used in a storage application. The binding energy properties and the corresponding charge transfer for each metal in the considered sites of a Be_2C surface are summarized in Table 6.2.

	Li		**Na**		**K**		**Mg**	
site	**E(eV)**	(Charge|q|)	**E(eV)**	(Charge|q|)	**E(eV)**	(Charge|q|)	**E(eV)**	(Charge|q|)
TBe2	-1.80	0.82	-1.01	0.62	-1.16	0.65	-0.84	0.29
TC	-1.50	0.72	-0.94	0.55	-1.02	0.60	-0.67	0.28
B	-0.98	0.70	-0.75	0.52	-0.89	0.57	-0.60	0.25
TBe2	-0.91	0.67	-0.73	0.51	-0.87	0.57	-0.58	0.23
TBe2	-0.82	0.66	-0.71	0.50	-0.86	0.56	-0.57	0.21
TBe1	-0.74	0.60	-0.66	0.50	-0.82	0.55	-0.53	0.16

Table 6.2: The calculated binding energy (E_b) of single Li/Na/K/Mg-decorated Be_2C system and Bader charge analysis of M atoms at TBe2, TC, B, H1, H2, and TBe1 sites.

According to the results from Table 6.2, it is evident that among the six-sites, the adatoms prefer to attach strongly to the beryllium carbide surface at the TBe2 site. Interestingly, all the sites are suitable owing to their negative values, therefore metal-atoms decoration are easily stabilized on the Be_2C surface. We observed also that the adsorption energies decrease in the following order Li>K>Na>Mg. Making of Li, the lightest element, as the most suitable choice for improving hydrogen storage, which is in line with previously published works [212, 213, 178]. Also, the minimum distances from Li, Na, K or Mg to the substrate are found to be 1.62, 2.06, 2.23 and 1.98 Å, respectively. Upon decoration, Bader charge analysis was used to study the charge transfer between M atom and Be_2C sheet. A charge transfer of 0.82, 0.62, 0.65 and 0.29|e| is observed from Li, Na, K and Mg to Be_2C monolayer, respectively. To sum up, these values indicate that: *i)* M atoms can chemically adsorb on the Be_2C monolayer; *ii)* lightest element contribute almost all

outer electrons to the 2D-Be_2C monolayer, and turn into M ions. Notably, because of strong Coulomb repulsion, it prevents the adsorbed M ions to form clusters.

To obtain more H_2 molecules on Be_2C surface and enhance the effect of hydrogen storage properties on this 2D material, one can increase the concentration of Li-, Na-, K- and Mg-atoms from 3.57% to 6.90% (referring to two M-atoms) at the most stable site (TBe2) on both sides of Be_2C layer as seen in Figure 6.4. After full structure relaxation of the Be_2C system with two adatoms on both sides, we found, based on equation 6.4, that E_b for 2Li-, 2Na-, 2K- and 2Mg-Be_2C are -1.47 eV, -0.97, -1.07 eV and -0.62 eV, respectively. Here the average binding energy values per 2M is slightly higher than for 3.57% M-coverage but, the $d_{M-sheet}$ distance increases due to the Coulomb repulsive interaction as compared to the single M case. They are close to other 2D-materials including GeC monolayer [178], graphene [89] and graphyne [182].

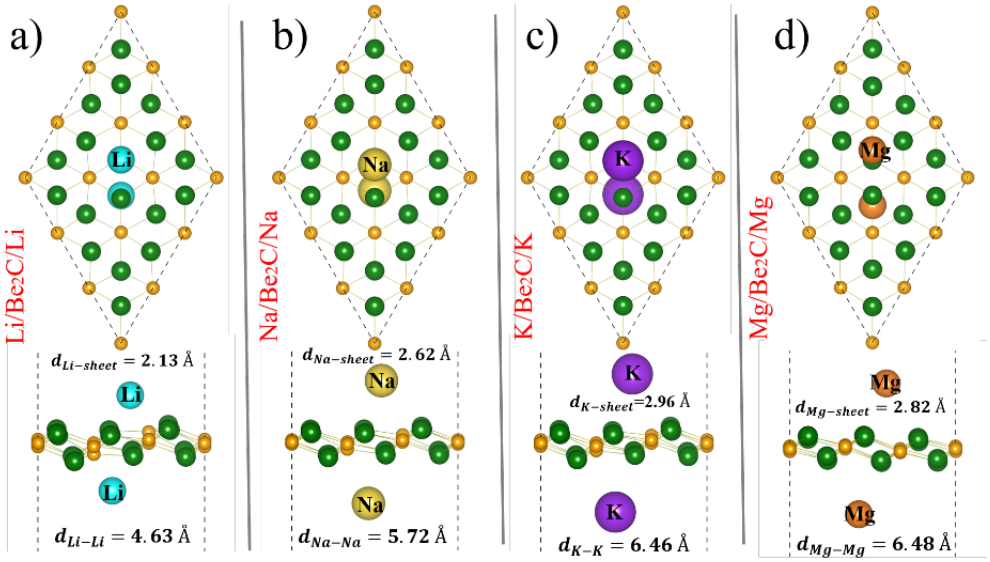


Figure 6.4: The optimized structures of Li/Na/K/Mg-decorated Be_2C on both sides using the DFT/vdW function.

In order to obtain further elucidation into the adsorption mechanism, we calculated the charge density difference ($\Delta\rho$) of M-doped Be_2C on both sides by a similar formula to equation 5.3, as illustrated in Figure 6.5(a-d). After adding M into Be_2C, most of charges are distributed in the intermediate area between the dopant and the adjacent atoms of the host material. Contour of electron depletion can be found on the Li, Na, K and Mg-atom (cyan color), while contour of electron accumulation is around Be_2C system (magenta color), which signifies that the charges are transferred from the guest metal to the host layer. Moreover, Bader charge atomic analysis was performed to quantify the number of electron transfer during the decoration process. Results show that over a TBe2-site, the

charged state of Li, Na, K, and Mg-atom are 0.70, 0.55, 0.57 and 0.20 |e|. This means that the M-atoms become cationic after adsorption which is beneficial for hydrogen storage as will be explained next.

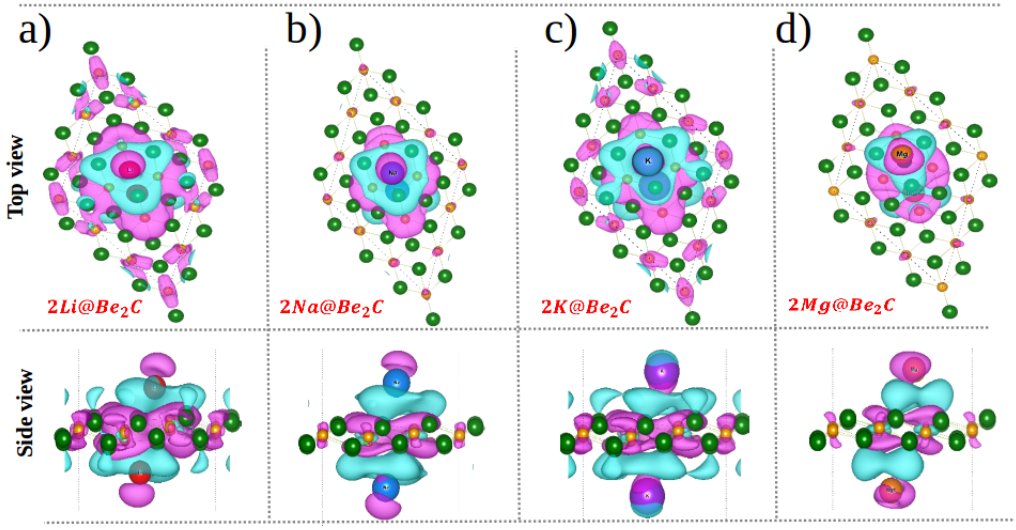


Figure 6.5: Top and side views of charge density differences for two-sided metal-decorated Be_2C monolayer at the most preferable adsorption site (TBe2) for: a) Li_2, b) Na_2, c) K_2, and d) Mg_2. The magenta and cyan areas stand for the charge gain and loss, respectively. The isosurfaces value are set to 0.0007 e/Å^3

Apart from the binding energy discussed previously, it is also important to understand the binding nature between M and Be_2C. For this, the electronic features of functionalized Be_2C sheets were analyzed through calculating the total (T-DOS) and projected (P-DOS) density of states. Figure 6.6(a-d) depicts the T-DOS and P-DOS of the pristine, magnesiated, lithiated, potassiated and sodiated Be_2C monolayer. As mentioned above, the pure Be_2C system behaves as a semiconductor material with a direct band gap similar to black phosphorene [214]. However, this gap characteristic changes upon the introduction of a guest adatom into the host-layer due to the downshifting of states occupied in the conduction band, confirming charge transfer discussed previously. For example, the adsorption of 2Li/2K into the surface of Be_2C introduces sizable DOS at fermi level (E_f). Furthermore, one can see a noticeable overlap between s-orbital of 2Li/2K and p-orbital of C/Be at E_f, which indicates a strong binding energy between Li/K and the Be_2C layer originating from s-p hybridizations interactions. This is a desired characteristic for a H_2 storage material. On the contrary, there is no electronic states at the Fermi level for the case of 2Mg/2Na, which proves the lower binding energy reported in the previous part. A similar tendency has also been observed in some other hydrogen storage materials such as boron phosphide [194], and siligraphene monolayer [213].

Next, with the aim of validating the promise of the Be_2C system as efficient H_2 stor-

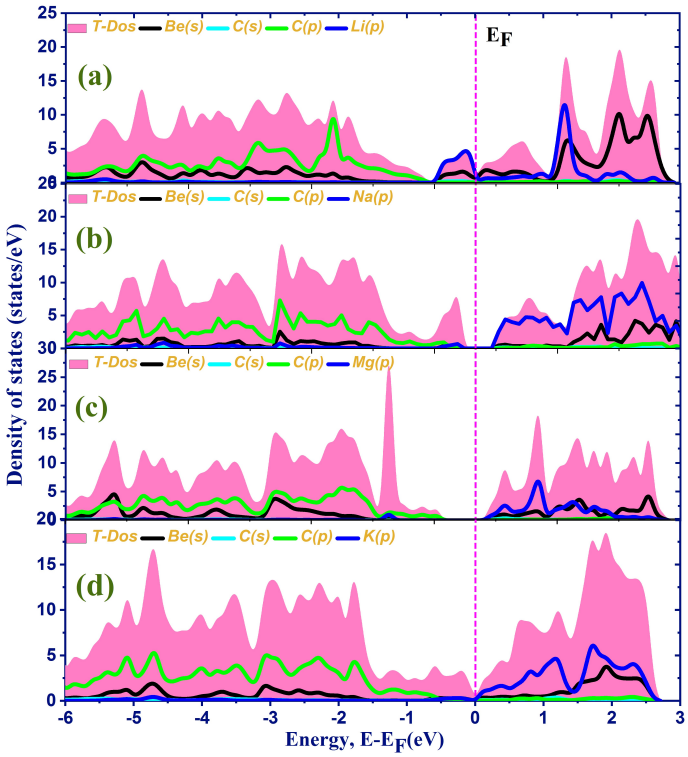


Figure 6.6: DOS plots of 2M@Be_2C monolayer at most adsorption site (TBe2) for: (a) 2Li, (b) 2Na, (c) 2Mg and (d)2K.

age substrate under ambient conditions, AIMD calculations within the framework of the canonical ensemble (NVT) where performed to assess the thermal stability of the Li/Na/K/Mg metalized Be_2C. By using the Nose Thermostat algorithm [215], each system was exposed to a temperature of 298 K for up to a total time of 55 ps. The computations results are plotted in Figure 6.7. It can be seen that the oscillations of the total energy of all considered systems are stabilized over the MDs time. In addition, the structures given at the end of MDs simulation do not show broken bonds or structural disruption. The planarity of the Be_2C sheet is also maintained except a tiny shifting of atoms from their average equilibrium positions, especially in the z-axis. These results stand for a good chance for establishing high-quality and high-stability H_2 storage by selecting Be_2C as media.

6.3.4 H_2 adsorption on Li/K-decorated Be_2C monolayer

We will now investigate the physisorption phenomena of hydrogen adsorption at a higher coverage with respect to understanding the effect of decorative metals on the storage capacity and the desorption temperature of a Be_2C monolayer as compared with the pure system. To estimate the interaction strength of the M@Be_2C system, we started by placing the H_2 molecules in the vicinity of the most stable elements (2Li and 2K atoms,

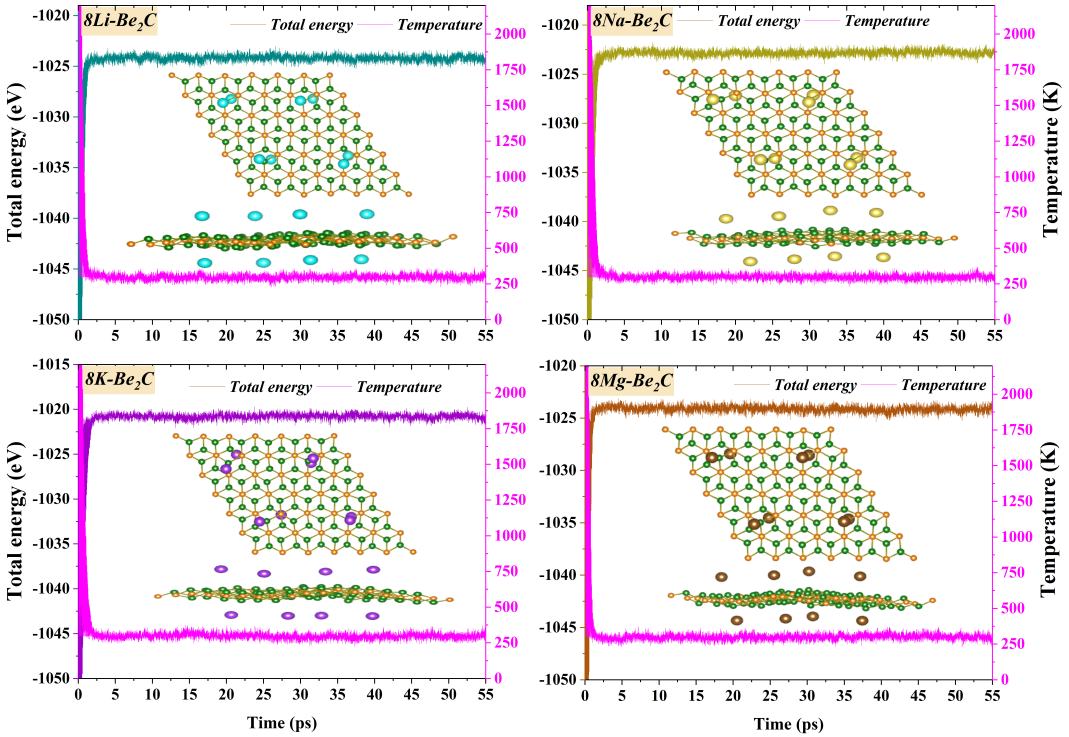


Figure 6.7: AIMD simulations were run for 55 ps at 298 K in (6×6)-supercell; temperature and total energy of the beryllium carbide decorated with 8Li, 8K, 8Mg and 8Na.

one from top and another from bottom side) in the surface structure based on results from Table 6.2.

In Figure 6.8, we display maximum amount of hydrogen molecules adsorbed on both sides of 2Li@Be_2C and 2K@Be_2C, which allows for a maximum gravimetric density and checking desorption temperature for the charge/release process of H_2 molecules.

We calculated the average and successive adsorption energies per hydrogen molecule (E_{ads}) and (E_s) for H_2 molecules adsorbed on the 2Li@Be_2C and 2K@Be_2C monolayer using the following equations:

$$E_{ads} = (E_{nH_2+2M@Be_2C} - E_{2M@Be_2C} - nE_{H_2})/n \tag{6.5}$$

$$E_s = E_{nH_2+2M@Be_2C} - E_{(n-1)H_2+2M@Be_2C} - E_{H_2} \tag{6.6}$$

where n is the number of H_2 molecules, $E_{nH_2+2M@Be_2C}$, E_{H_2}, $E_{(n-1)H_2+2M@Be_2C}$, and $E_{2M@Be_2C}$ are the total energies of: nH_2 molecules adsorbed on Be_2C monolayer of the decorated system by M= Li or K, single H_2 molecule, (n-1)H_2 molecules adsorbed on $2M@Be_2C$ monolayer, and system without H_2, respectively.

By adding one by one hydrogen molecules to adsorb on the 2Li and 2K-decorated

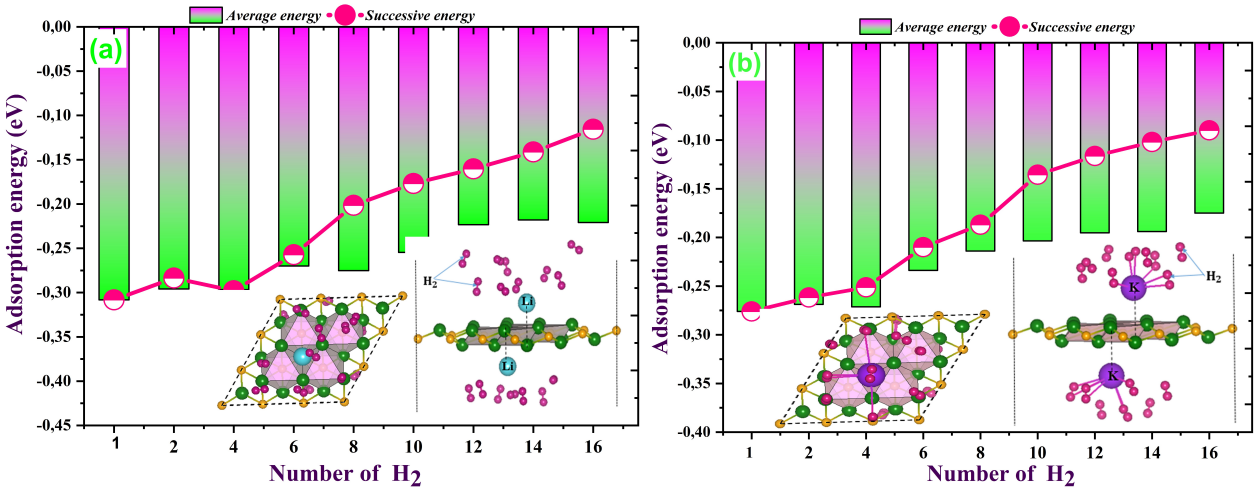


Figure 6.8: Average/successive adsorption energies as a function of the number of adsorbed hydrogen molecules on (a) 2Li@Be_2C and (b) 2K@Be_2C.

Be_2C system, using the vdW-DF-ob86 function which is more precise for the optimization of the hydrogen interaction mechanism [216], we can see the effect of the decoration concentration of the 2Li/2K elements on the adsorption energies between one and several molecules of hydrogen. The obtained results of successive H_2 adsorption energies for nH_2/2Li@Be_2C and nH_2/2K@Be_2C are found in the range of [-0.308; -0.152 eV] and [-0.276; -0.168 eV], respectively, as shown in Figure 6.8(a-b). The distance between neighboring hydrogen molecules is between 1.74 and 2.59 Å, while the average distance between H atoms in the same molecule is 0.749-0.762 Å. For the same reason, we found that the adsorption energy of a single adsorbed hydrogen molecule with Li/K-decorated Be_2C systems is drastically improved in comparison to the pure Be_2C monolayer as shown in Figure 6.8. For example, the adsorption energies for 2Li@Be_2C increased from -0.308 to -0.263 eV for Be_2C. These values are significantly lower than the E_b of the single H_2/Li-Be_3C_2 monolayer, which were reported at -0.260 eV [203]. It is also observed that there is a substantial increase of the successive adsorption energies as a function of the concentration (6.90%) for the Li/K-decoration elements and the increase of the number of adsorbed hydrogen molecules. Successive addition of H_2 molecules to the functionalized 2Li@Be_2C and 2K@Be_2C reveals that even if the adsorption energy E_s<0.150 eV per H_2, a total of 13 hydrogen molecules are adsorbed for 2Li@Be_2C while 2K@Be_2C adsorbs only 9 H_2. Then, the H_2 uptakes is 8.45$wt.$% and 4.94$wt.$% for 2Li@Be_2C+13H_2 and 2K@Be_2C+9H_2, respectively. These values are found to be very remarkable than those obtained according to previous works [217, 187, 212].

On the other hand, it is important to mention that the average adsorption energy per H_2 for associative adsorption varies from -0.308 to -0.220 eV for 2Li@Be_2C and -0.276 to -0.175 eV for 2K@Be_2C. It is located in the desired energy range of (-0.15) ~(-0.6 eV).

These results are in good agreement with those found in the literature [210, 182]. Moreover, these results demonstrate that the hydrogen molecules strongly bind to Li/K-metal cations in the decorated Be_2C system by an extent of electron density transfer depending on the ionization potential. Thus, we proved that the decoration by the considered elements has a large effect on the adsorption of hydrogen with of Be_2C monolayer.
Based on the average energy results, we conclude that both systems reach saturation at 16 H_2 hydrogen molecules, with stable adsorption energies. At the maximum H_2 coverage, H_2 storage capacities of 10.21 and 8.48$wt.\%$ have been achieved for 2Li@Be_2C and 2K@Be_2C, respectively. Figure 6.9 shows a comparison between the storage capacities in this work for the maximum number of adsorbed H_2 molecules per lithium- and potassium-decorated with other theoretical studies that address related 2D materials. Thus, this system can be distinguished from other currently available 2D-materials as a promising candidate for H_2 storage under room conditions.

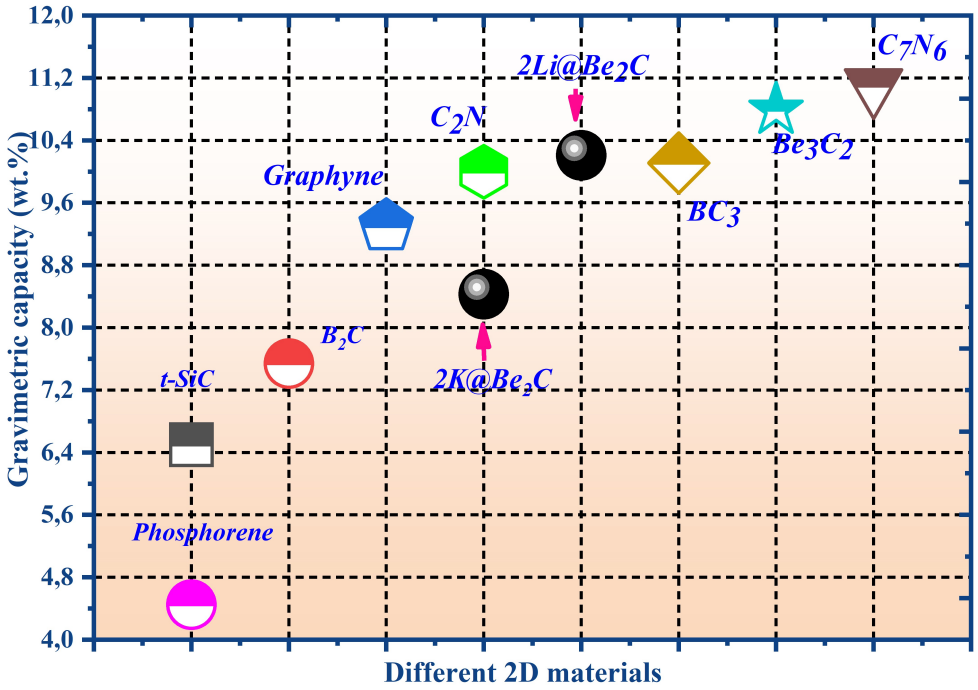


Figure 6.9: Hydrogen storage capacities for $16H_2/2Li@Be_2C$ and $16H_2/2K@Be_2C$ compared to other different 2D-materials.

According to equation 5.5, the desorption temperature depends on the average adsorption energies (see Figure 6.8). The 2Li@Be_2C temperature lies in the range of 228-163 K while for 2K@Be_2C, it is located between 204 and 129 K. For both decorated-systems, we found that the desorption temperature values are considerably higher than those of other 2D materials such as Li-carbyne [195] and Li/Na@BP [194] whose values are of 149 and 116/95 K, respectively. We mention that the T_{des} of our systems are also much higher

than the critical temperature (33K) of hydrogen and about two times the boiling point of liquid nitrogen (77 K).

6.3.5 Thermodynamics of adsorption hydrogen molecules

In order to verify the desorption temperature estimations, we performed ab-initio MD in the NVT ensemble for hydrogenated 2Li@Be_2C and 2K@Be_2C of the highest gravimetric density (See Figure 6.8) at two chosen temperatures of 100K and 298K. To avoid restricting H_2 movements on Li and K decorated Be_2C (3×3)-cells in AIMD calculations, we used a (6×6)-supercell containing 244 atoms with the vacuum layer increased to 30 Å and a time step of 1 fs. As shown in Figure.11, we selectively depict the snapshots of the structures (top and side views): H_2-atoms with distance Li/K-H_2 more than 2.5 Å are noted by pink color and less than 2.5 Å by blue color. At 100 K (Figure 6.10 (a,c)), we can see that the hydrogen molecules moved noticeably far away from 8Li/8K-decorated and substrate. At ambient temperatures (Figure 6.10 (b,d)), all H_2 molecules moved from 8Li/8K-atoms and some of them have been removed from structures, with a small corrugation along z-axis. Thus, these results support the van't Hoff desorption temperature estimations.

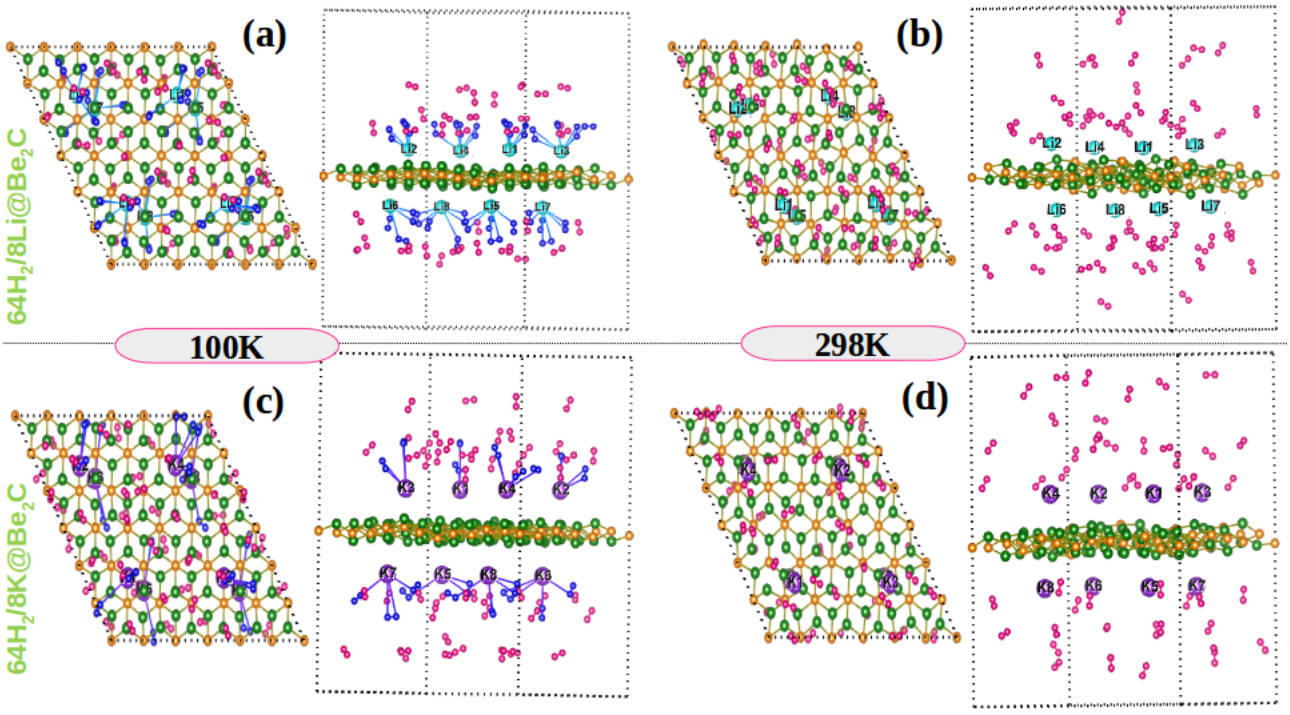


Figure 6.10: Images of AIMD simulations at 100 and 298 K of 64H_2 desorbed 8Li@Be_2C and 8K@Be_2C systems as obtained at the end of 20 ps.

Our study demonstrates that lithium and potassium doped Be_2C monolayer could be

considered as a promising host material with great physisorption characteristics and high gravimetric density for hydrogen storage.

6.4 Summary and conclusion

In summary, van der Waals-density functional theory (DFT) calculations were carried out to study the structural and electronic properties, thermal stability, and hydrogen storage properties of the 2D structure of pristine Be_2C as a hosting material for H_2-storage applications. The effect of decoration using the alkali metal (Li, Na and K) and alkaline earth metal (Mg) adatoms on the Be_2C system was also investigated. Ab initio molecular dynamics (AIMD) calculations confirmed the thermal stabilities of 8M@Be_2C (M= Li, Na, K, Mg) at 298 K. The results show that the adsorption of a single hydrogen molecule on a pristine Be_2C system at different adsorption sites gives adsorption energies in the range of -0.140/-0.228 eV. We showed that the Li/K-decorations on both sides of Be_2C improves the adsorption energies to -0.308 eV/H_2 for the case of 2Li@Be_2C monolayer. Overall, 2Li@Be_2C and 2K@Be_2C can adsorb up to 16 molecular hydrogen H_2 on both sides, with an average energy within the desirable range of an effective hydrogen storage characteristics and desorption temperature. The maximum gravimetric hydrogen storage capacities of 2Li@Be_2C and 2K@Be_2C reach 10.21 and 8.48$wt.\%$, respectively, exceeding US-DOE requirements of the weight percentage in hydrogen storage materials.

General Conclusion and Perspectives

Hydrogen storage capacity, re/dehydrogenation temperature, reversibility, and kinetic performance of hydrogen storage materials are some of the most challenging obstacles to the widespread use of hydrogen energy. The ultimate goal of hydrogen storage capacity is 6.5 wt% with operation temperature in the range of 233 to 333 K according to the standard released by US-DoE. However, it is a major challenge for the high-pressure gas storage and low-temperature liquid storage to achieve the future goals due to the volume density, safety requirements, or practical issues. Solid-state H_2 storage materials are the most potential ones to meet the practical standard for mobile applications. This thesis aims to provide an in-depth understanding of the hydrogen storage properties in Metal Organic Framework-5 (MOF-5) and two-dimensional materials (2D) through the use of quantum mechanical simulations: density functional theory (DFT) and DFT based ab initio molecular dynamics (AIMD).

The primary aim of this work has been devoted to the nanoporous materials of the metal-organic frameworks type MOF-5. New approach aims to tune the hydrogen storage properties of connector-MOF-5. The model presents a good stability (-13.85 $kJ/mol.H_2$) with a decomposition temperature of 115.4 K . Also, we showed that the metallic and cyclic sites are more stable for multiple hydrogen molecule storage and the system reaches 4.57 wt% as a gravimetric storage capacity which is located in the interval 4.50-5.20 wt% found experimentally. The second strategy used to improve the hydrogen storage capacity is the effect of decoration and substitution on the unit cell-MOF-5. Precisely, two phenomena at the same time: substitution of Zn atoms by Cd and Mg in the unit cell center and decoration by three elements namely Li, Be and Na atoms in the center of the 6-atoms carbon ring. The obtained results indicated that the functionalization of Li, Be and Na combined with the substitution enhances the hydrogen storage properties and gravimetric capacity as well as desorption temperature. It was found that the maximum gravimetric storage capacity shifted from 4.09 wt% (pure) to 5.41, 4.78 and 4.45 wt% for Li_2-decorated Mg-MOF-5, Li_2-decorated Zn-MOF-5 and Li_2-decorated Cd-MOF-5, respectively. Moreover, the desorption temperature is 513 for Mg-MOF-5:Li_2 and 463 K for Zn-MOF-5:Li_2. All results are in good agreement with the available theoretical and

experimental data.

Moving on, the conditions that a 2D material must satisfy to become an efficient solid-state H_2 storage medium were investigated, where the main factors in focus are thermodynamic stability, adsorption energy, desorption temperature, H_2 diffusion, storage capacities and hydrogenation/dehydrogenation kinetics. In this regard, a novel 2D t-graphene-like boron nitride ($t - B_4N_4$) monolayer is considered as a material suitable for the hydrogen storage due to its interesting properties. Our results show that the adsorption energy (-0.386 to -0.217 eV) of H_2 on Li-decorated double-sided $t - B_4N_4$ is appropriate for storage, with a maximum hydrogen storage capacity of 12.47 wt%. Further, the reversibility of adsorbed hydrogen was checked and the calculated desorption temperature was 161 K, much higher than the critical point for hydrogen. The analysis of diffusion pathways between different physisorbed states on the $t - B_4N_4$ surface shows that a single hydrogen molecule diffuses very easily (0.0098 eV) compared to t-graphene and graphene.
On the other hand, we systematically studied the structural stability, electronic properties and the hydrogen storage properties of the pure beryllium carbide (Be_2C) monolayer. The obtained results show that the adsorption energies of H_2 molecules in this system are exactly located in the desirable energy range. Furthermore, the stabilization of hydrogen by metal decoration of Be_2C on both sides was improved in comparison to that of pristine Be_2C. 2Li@Be_2C and 2K@Be_2C were able to host up to 16 molecules of hydrogen reaching a gravimetric capacity of 10.21 and 8.48 wt%, respectively. In addition, the desorption temperature estimates were validated by AIMD simulations of hydrogenated Li@Be_2C and K@Be_2C. Thus, the Li/K@Be_2C system can be a promising candidate for the experimental setup for hydrogen storage.

The work presented in this thesis gives insight on the performance improvement of hydrogen storage in solid state materials by Ab initio simulations. Specifically, there are additional details which must be obtained to provide a more complete picture at the practical real-world level for hydrogen storage applications. Hence, the following avenues of investigation should be explored further in the future:

- Hydrogen Storage in Metal Organic Frameworks

- Study mechanism of other light weight metals to create strong binding sites between molecular hydrogen and the metal-organic frameworks.
- MgH_2-nanocluster impregnated isoreticular metal-organic framework (IRMOF-1) to achieve unique H_2 storage properties, in the sense that chemical interactions would be expected to be stronger than weak van der Waals forces.
- Study the hydrogen storage ability of *two-dimensional metal–organic frameworks*

(2D-MOFs) under ambient temperature and pressure conditions.

- Hydrogen Storage in two-dimensional materials (2D)

- Study a novel H_2 storage architecture by decorating Be_2C and $t-B_4N_4$ monolayer with the super-alkali clusters (NLi4, Li3O,...) to higher their hydrogen desorption temperature and increase their hydrogen storage reversibility.
- Design of new 2D-materials with improved hydrogen storage capacities and with favorable hydrogen properties.

Bibliography

[1] Amutha Chinnappan, John Marc C Puguan, Wook-Jin Chung, and Hern Kim. Hydrogen generation from the hydrolysis of sodium borohydride using chemically modified multiwalled carbon nanotubes with pyridinium based ionic liquid and decorated with highly dispersed mn nanoparticles. *Journal of Power Sources*, 293:429–436, 2015.

[2] Carolyn C Elam, Catherine E Gregoire Padró, Gary Sandrock, Andreas Luzzi, Peter Lindblad, and Elisabet Fjermestad Hagen. Realizing the hydrogen future: the international energy agency's efforts to advance hydrogen energy technologies. *International Journal of Hydrogen Energy*, 28(6):601–607, 2003.

[3] Muhammet Deveci. Site selection for hydrogen underground storage using interval type-2 hesitant fuzzy sets. *International Journal of Hydrogen Energy*, 43(19):9353–9368, 2018.

[4] Sheetal Kumar Dewangan, Man Mohan, Vinod Kumar, Ashutosh Sharma, and Byungmin Ahn. A comprehensive review of the prospects for future hydrogen storage in materials-application and outstanding issues. *International Journal of Energy Research*, 2022.

[5] Bernard Chukwudi Tashie-Lewis and Somtochukwu Godfrey Nnabuife. Hydrogen production, distribution, storage and power conversion in a hydrogen economy-a technology review. *Chemical Engineering Journal Advances*, 8:100172, 2021.

[6] George W Crabtree, Mildred S Dresselhaus, and Michelle V Buchanan. The hydrogen economy. *Physics today*, 57(12):39–44, 2004.

[7] Ferdinand G Brickwedde. Harold urey and the discovery of deuterium. *Physics Today*, 35(9):34–39, 1982.

[8] Marcus Laurence Elwin Oliphant, Paul Harteck, and Ernest Rutherford. Transmutation effects observed with heavy hydrogen. *Proceedings of the Royal Society of*

London. Series A, Containing Papers of a Mathematical and Physical Character, 144(853):692–703, 1934.

[9] MP Malkov. Hand-book on physical-chemical fundamentals of cryogenics. *Energoatomizdat, Moscow, USSR*, 1985.

[10] VL Bondarenko, DN Ilyinskaya, AA Kazakova, PS Kozlovtsev, NA Lavrov, and EA Razenko. Hydrogen, its unique properties and applications in industry. *Chemical and Petroleum Engineering*, 57(11):1015–1019, 2022.

[11] Andreas Züttel. Hydrogen storage methods. *Naturwissenschaften*, 91(4):157–172, 2004.

[12] WB Leung, NH March, and H Motz. Primitive phase diagram for hydrogen. *Physics Letters A*, 56(6):425–426, 1976.

[13] Sunita Sharma and Sib Krishna Ghoshal. Hydrogen the future transportation fuel: From production to applications. *Renewable and sustainable energy reviews*, 43:1151–1158, 2015.

[14] Hiroyasu Furukawa, Kyle E Cordova, Michael O'Keeffe, and Omar M Yaghi. The chemistry and applications of metal-organic frameworks. *Science*, 341(6149):1230444, 2013.

[15] Kimberley Cousins and Renwu Zhang. Highly porous organic polymers for hydrogen fuel storage. *Polymers*, 11(4):690, 2019.

[16] Hyun Tae Hwang and Arvind Varma. Hydrogen storage for fuel cell vehicles. *Current Opinion in Chemical Engineering*, 5:42–48, 2014.

[17] T Ozturk and A Demirbas. Boron compounds as hydrogen storage materials. *Energy Sources, Part A*, 29(15):1415–1423, 2007.

[18] Hervé Barthélémy. Hydrogen storage–industrial prospectives. *International journal of hydrogen energy*, 37(22):17364–17372, 2012.

[19] Hervé Barthélémy, Mathilde Weber, and Françoise Barbier. Hydrogen storage: Recent improvements and industrial perspectives. *International Journal of Hydrogen Energy*, 42(11):7254–7262, 2017.

[20] Martin Khzouz and Evangelos I Gkanas. Hydrogen technologies for mobility and stationary applications: hydrogen production, storage and infrastructure development. In *Renewable Energy-Resources, Challenges and Applications*. IntechOpen, 2020.

[21] RS Irani. Hydrogen storage: high-pressure gas containment. *Mrs Bulletin*, 27(9):680–682, 2002.

[22] Joachim Wolf. Liquid-hydrogen technology for vehicles. *MRS bulletin*, 27(9):684–687, 2002.

[23] SA Sherif, N Zeytinoglu, and TN Veziroğlu. Liquid hydrogen: Potential, problems, and a proposed research program. *International journal of hydrogen energy*, 22(7):683–688, 1997.

[24] Arthur M James and Mary P Lord. *Macmillan's chemical and physical data*. Macmillan, 1992.

[25] Adnan Midilli, Mo Ay, Ibraham Dincer, and Marc A Rosen. On hydrogen and hydrogen energy strategies: I: current status and needs. *Renewable and sustainable energy reviews*, 9(3):255–271, 2005.

[26] Louis Schlapbach and Andreas Züttel. Hydrogen-storage materials for mobile applications. In *Materials for sustainable energy: a collection of peer-reviewed research and review articles from nature publishing group*, pages 265–270. World Scientific, 2011.

[27] RK Ahluwalia, TQ Hua, J-K Peng, S Lasher, Kurtis McKenney, J Sinha, and Monterey Gardiner. Technical assessment of cryo-compressed hydrogen storage tank systems for automotive applications. *International journal of hydrogen energy*, 35(9):4171–4184, 2010.

[28] Patrick Preuster, Alexander Alekseev, and Peter Wasserscheid. Hydrogen storage technologies for future energy systems. *Annual review of chemical and biomolecular engineering*, 8:445–471, 2017.

[29] A Demirbas. Storage and transportation opportunities of hydrogen. *Energy Sources, Part B*, 2(3):287–295, 2007.

[30] Valentina Tozzini and Vittorio Pellegrini. Prospects for hydrogen storage in graphene. *Physical Chemistry Chemical Physics*, 15(1):80–89, 2013.

[31] Kean Long Lim, Hossein Kazemian, Zahira Yaakob, and Wan Ramli Wan Daud. Solid-state materials and methods for hydrogen storage: a critical review. *Chemical Engineering & Technology: Industrial Chemistry-Plant Equipment-Process Engineering-Biotechnology*, 33(2):213–226, 2010.

[32] Y Miura, H Kasai, W Dino, H Nakanishi, and T Sugimoto. First principles studies for the dissociative adsorption of h 2 on graphene. *Journal of Applied Physics*, 93(6):3395–3400, 2003.

[33] A Züttel, P Sudan, Ph Mauron, T Kiyobayashi, Ch Emmenegger, and LJIJoHE Schlapbach. Hydrogen storage in carbon nanostructures. *International Journal of Hydrogen Energy*, 27(2):203–212, 2002.

[34] Darren P Broom. Potential storage materials. In *Hydrogen Storage Materials*, pages 19–59. Springer, 2011.

[35] Otto Pesonen and Tuomas Alakunnas. Energy storage: A missing piece of the puzzle for the self-sufficient living. 2017.

[36] Martin Dornheim. Thermodynamics of metal hydrides: tailoring reaction enthalpies of hydrogen storage materials. In *Thermodynamics-Interaction Studies-Solids, Liquids and Gases*. IntechOpen, 2011.

[37] T Palewski, NV Tristan, H Drulis, and J Ćwik. Hydrogenation process of the gd3m (m= ni or co) intermetallics compound. *Journal of alloys and compounds*, 404:584–587, 2005.

[38] Hongge Pan, Yongfeng Liu, Mingxia Gao, Yunfeng Zhu, and Yongquan Lei. The structural and electrochemical properties of la0. 7mg0. 3 (ni0. 85co0. 15) x (x= 3.0–5.0) hydrogen storage alloys. *International Journal of Hydrogen Energy*, 28(11):1219–1228, 2003.

[39] M Okada, T Kuriiwa, A Kamegawa, and H Takamura. Role of intermetallics in hydrogen storage materials. *Materials Science and Engineering: A*, 329:305–312, 2002.

[40] Biljana Rolih. *A First Principles Study of Mass Transport in the Dehydrogenation of Lithium Amides and Lithium Alanates*. University of California, Los Angeles, 2014.

[41] Sesha Srinivasan, Diego Escobar, Yogi Goswami, and Elias Stefanakos. Effects of catalysts doping on the thermal decomposition behavior of zn (bh4) 2. *International Journal of Hydrogen Energy*, 33(9):2268–2272, 2008.

[42] Tapas K Mandal and Duncan H Gregory. Hydrogen: a future energy vector for sustainable development. *Proceedings of the institution of mechanical engineers, part C: journal of mechanical engineering science*, 224(3):539–558, 2010.

[43] B Bogdanović, Michael Felderhoff, Stefan Kaskel, Andre Pommerin, Klaus Schlichte, and Ferdi Schueth. Improved hydrogen storage properties of ti-doped sodium alanate using titanium nanoparticles as doping agents. *Advanced Materials*, 15(12):1012–1015, 2003.

[44] Marcello A Budroni, Sebastiano Garroni, Gabriele Mulas, and Mauro Rustici. Bursting dynamics in molecular hydrogen generation via sodium borohydride hydrolysis. *The Journal of Physical Chemistry C*, 121(9):4891–4898, 2017.

[45] Mohammad Ismail, Yue Zhao, XB Yu, Abbas Ranjbar, and SX Dou. Improved hydrogen desorption in lithium alanate by addition of swcnt–metallic catalyst composite. *international journal of hydrogen energy*, 36(5):3593–3599, 2011.

[46] Lyci George and Surendra K Saxena. Structural stability of metal hydrides, alanates and borohydrides of alkali and alkali-earth elements: A review. *International Journal of Hydrogen Energy*, 35(11):5454–5470, 2010.

[47] Jun Yang, Andrea Sudik, Christopher Wolverton, and Donald J Siegel. High capacity hydrogen storage materials: attributes for automotive applications and techniques for materials discovery. *Chemical Society Reviews*, 39(2):656–675, 2010.

[48] Xiang-Dong Kang, Jun-Hong Luo, and Ping Wang. Efficient and highly rapid hydrogen release from ball-milled 3nh3bh3/mmgh3 (m= na, k, rb) mixtures at low temperatures. *International journal of hydrogen energy*, 37(5):4259–4266, 2012.

[49] Olena Zavorotynska, Abdelouahab El-Kharbachi, Stefano Deledda, and Bjørn C Hauback. Recent progress in magnesium borohydride mg (bh4) 2: Fundamentals and applications for energy storage. *international journal of hydrogen energy*, 41(32):14387–14403, 2016.

[50] Jinxiang Dong, Xiaoyan Wang, Hong Xu, Qiang Zhao, and Jinping Li. Hydrogen storage in several microporous zeolites. *International Journal of Hydrogen Energy*, 32(18):4998–5004, 2007.

[51] Peter M Budd, Anna Butler, James Selbie, Khalid Mahmood, Neil B McKeown, Bader Ghanem, Kadhum Msayib, David Book, and Allan Walton. The potential of organic polymer-based hydrogen storage materials. *Physical Chemistry Chemical Physics*, 9(15):1802–1808, 2007.

[52] Keyu Geng, Ting He, Ruoyang Liu, Sasanka Dalapati, Ke Tian Tan, Zhongping Li, Shanshan Tao, Yifan Gong, Qiuhong Jiang, and Donglin Jiang. Covalent organic

frameworks: design, synthesis, and functions. *Chemical reviews*, 120(16):8814–8933, 2020.

[53] Linyu Wang, Shasha Hong, Yuxi Yang, Yonghai Song, and Li Wang. Covalent organic frameworks for electrochemical sensors: Recent research and future prospects. *Current Analytical Chemistry*, 18(6):646–663, 2022.

[54] Emmanouel Klontzas, Emmanuel Tylianakis, and George E Froudakis. Hydrogen storage in 3d covalent organic frameworks. a multiscale theoretical investigation. *The Journal of Physical Chemistry C*, 112(24):9095–9098, 2008.

[55] Antek G Wong-Foy, Adam J Matzger, and Omar M Yaghi. Exceptional h2 saturation uptake in microporous metal- organic frameworks. *Journal of the American Chemical Society*, 128(11):3494–3495, 2006.

[56] Nathaniel L Rosi, Juergen Eckert, Mohamed Eddaoudi, David T Vodak, Jaheon Kim, Michael O'Keeffe, and Omar M Yaghi. Hydrogen storage in microporous metal-organic frameworks. *Science*, 300(5622):1127–1129, 2003.

[57] Omar M Yaghi, Michael O'Keeffe, Nathan W Ockwig, Hee K Chae, Mohamed Eddaoudi, and Jaheon Kim. Reticular synthesis and the design of new materials. *Nature*, 423(6941):705–714, 2003.

[58] EA Tomic. Thermal stability of coordination polymers. *Journal of Applied Polymer Science*, 9(11):3745–3752, 1965.

[59] B F Hoskins and Richard Robson. Design and construction of a new class of scaffolding-like materials comprising infinite polymeric frameworks of 3d-linked molecular rods. a reappraisal of the zinc cyanide and cadmium cyanide structures and the synthesis and structure of the diamond-related frameworks [n (ch3) 4][cuiznii (cn) 4] and cui [4, 4', 4", 4"'-tetracyanotetraphenylmethane] bf4. xc6h5no2. *Journal of the American Chemical Society*, 112(4):1546–1554, 1990.

[60] OM Yaghi and Hailian Li. Hydrothermal synthesis of a metal-organic framework containing large rectangular channels. *Journal of the American Chemical Society*, 117(41):10401–10402, 1995.

[61] Hailian Li, Mohamed Eddaoudi, Michael O'Keeffe, and Omar M Yaghi. Design and synthesis of an exceptionally stable and highly porous metal-organic framework. *nature*, 402(6759):276–279, 1999.

[62] Seyed Mohamad Moosavi, Aditya Nandy, Kevin Maik Jablonka, Daniele Ongari, Jon Paul Janet, Peter G Boyd, Yongjin Lee, Berend Smit, and Heather J Kulik. Understanding the diversity of the metal-organic framework ecosystem. *Nature communications*, 11(1):1–10, 2020.

[63] PS Sharanyakanth and Mahendran Radhakrishnan. Synthesis of metal-organic frameworks (mofs) and its application in food packaging: A critical review. *Trends in Food Science & Technology*, 104:102–116, 2020.

[64] Mohamed Eddaoudi, Jaheon Kim, Nathaniel Rosi, David Vodak, Joseph Wachter, Michael O'Keeffe, and Omar M Yaghi. Systematic design of pore size and functionality in isoreticular mofs and their application in methane storage. *Science*, 295(5554):469–472, 2002.

[65] Sami Ullah, MA Bustam, AM Shariff, Ali EI Elkhalifah, G Murshid, and Nadia Riaz. Synthesis and co 2 adsorption study of modified mof-5 with multi-wall carbon nanotubes and expandable graphite. In *AIP Conference Proceedings*, volume 1621, pages 34–39. American Institute of Physics, 2014.

[66] Samir Alghool and Carla Slebodnick. One dimensional structure of zn (ii) metal organic framework (mof) assembled rapidly at room temperature: structural, thermal study, and luminescent properties. *Journal of Inorganic and Organometallic Polymers and Materials*, 24(3):644–651, 2014.

[67] Wang Peng-Fei, Wu Xiao-Shuo, Wei Bo, and Wu Guo-Zhi. Syntheses, crystal structures, thermal stabilities of nickel (ii) coordination polymers constructed from the substitutional benzenedicarboxylic acid and auxiliary n-donor ligands. *Chinese Journal of Inorganic Chemistry*, 30(7):1511–1517, 2014.

[68] Sven MJ Rogge, Michel Waroquier, and Veronique Van Speybroeck. Reliably modeling the mechanical stability of rigid and flexible metal–organic frameworks. *Accounts of chemical research*, 51(1):138–148, 2018.

[69] Hexiang Deng, Sergio Grunder, Kyle E Cordova, Cory Valente, Hiroyasu Furukawa, Mohamad Hmadeh, Felipe Gándara, Adam C Whalley, Zheng Liu, Shunsuke Asahina, et al. Large-pore apertures in a series of metal-organic frameworks. *science*, 336(6084):1018–1023, 2012.

[70] Jesse LC Rowsell, Andrew R Millward, Kyo Sung Park, and Omar M Yaghi. Hydrogen sorption in functionalized metal- organic frameworks. *Journal of the American Chemical Society*, 126(18):5666–5667, 2004.

[71] Steven S Kaye, Anne Dailly, Omar M Yaghi, and Jeffrey R Long. Impact of preparation and handling on the hydrogen storage properties of zn4o (1, 4-benzenedicarboxylate) 3 (mof-5). *Journal of the American Chemical Society*, 129(46):14176–14177, 2007.

[72] Michael Hirscher. Hydrogen storage by cryoadsorption in ultrahigh-porosity metal–organic frameworks. *Angewandte Chemie International Edition*, 50(3):581–582, 2011.

[73] Dipendu Saha, Zuojun Wei, and Shuguang Deng. Equilibrium, kinetics and enthalpy of hydrogen adsorption in mof-177. *International journal of hydrogen energy*, 33(24):7479–7488, 2008.

[74] Barbara Panella, Katja Hönes, Ulrich Müller, Natalia Trukhan, Markus Schubert, Hermann Pütter, and Michael Hirscher. Desorption studies of hydrogen in metal–organic frameworks. *Angewandte Chemie International Edition*, 47(11):2138–2142, 2008.

[75] Jesse LC Rowsell, Juergen Eckert, and Omar M Yaghi. Characterization of h2 binding sites in prototypical metal- organic frameworks by inelastic neutron scattering. *Journal of the American Chemical Society*, 127(42):14904–14910, 2005.

[76] T Yildirim and MR Hartman. Direct observation of hydrogen adsorption sites and nanocage formation in metal-organic frameworks. *Physical Review Letters*, 95(21):215504, 2005.

[77] Andreas Blomqvist, C Moysés Araújo, P Srepusharawoot, and Rajeev Ahuja. Li-decorated metal–organic framework 5: a route to achieving a suitable hydrogen storage medium. *Proceedings of the National Academy of Sciences*, 104(51):20173–20176, 2007.

[78] Sang Soo Han, Wei-Qiao Deng, and William A Goddard III. Improved designs of metal–organic frameworks for hydrogen storage. *Angewandte Chemie*, 119(33):6405–6408, 2007.

[79] Cristian I Contescu, Craig M Brown, Yun Liu, Vinay V Bhat, and Nidia C Gallego. Detection of hydrogen spillover in palladium-modified activated carbon fibers during hydrogen adsorption. *The Journal of Physical Chemistry C*, 113(14):5886–5890, 2009.

[80] Pradip Kumar, Shiv Singh, SAR Hashmi, and Ki-Hyun Kim. Mxenes: Emerging 2d materials for hydrogen storage. *Nano Energy*, 85:105989, 2021.

[81] Massimiliano Bartolomei, Estela Carmona-Novillo, and Giacomo Giorgi. First principles investigation of hydrogen physical adsorption on graphynes' layers. *Carbon*, 95:1076–1081, 2015.

[82] Ekaterina Anikina, Amitava Banerjee, Valery Beskachko, and Rajeev Ahuja. Li-functionalized carbon nanotubes for hydrogen storage: importance of size effects. *ACS Applied Nano Materials*, 2(5):3021–3030, 2019.

[83] Minxiang Zeng, Mingfeng Chen, Dali Huang, Shijun Lei, Xuan Zhang, Ling Wang, and Zhengdong Cheng. Engineered two-dimensional nanomaterials: An emerging paradigm for water purification and monitoring. *Materials Horizons*, 8(3):758–802, 2021.

[84] Tingting Hu, Xuan Mei, Yingjie Wang, Xisheng Weng, Ruizheng Liang, and Min Wei. Two-dimensional nanomaterials: fascinating materials in biomedical field. *Science Bulletin*, 64(22):1707–1727, 2019.

[85] Ankur Gupta, Tamilselvan Sakthivel, and Sudipta Seal. Recent development in 2d materials beyond graphene. *Progress in Materials Science*, 73:44–126, 2015.

[86] Mingyue Zhao, Yurui Hao, Chen Zhang, Rongli Zhai, Benqing Liu, Wencheng Liu, Cong Wang, Syed Hassan Mujtaba Jafri, Aamir Razaq, Raffaello Papadakis, et al. Advances in two-dimensional materials for optoelectronics applications. *Crystals*, 12(8):1087, 2022.

[87] Xuebin Yu, Ziwei Tang, Dalin Sun, Liuzhang Ouyang, and Min Zhu. Recent advances and remaining challenges of nanostructured materials for hydrogen storage applications. *Progress in Materials Science*, 88:1–48, 2017.

[88] Mudita Nagpal and Rita Kakkar. An evolving energy solution: intermediate hydrogen storage. *International Journal of Hydrogen Energy*, 43(27):12168–12188, 2018.

[89] C Ataca, E Aktürk, SALİM Ciraci, and HANDE Ustunel. High-capacity hydrogen storage by metallized graphene. *Applied Physics Letters*, 93(4):043123, 2008.

[90] Jianfu Li, Xiaoli Wang, Kai Liu, Yuanyuan Sun, and Li Chen. High hydrogen-storage capacity of b-adsorbed graphene: first-principles calculation. *Solid state communications*, 152(5):386–389, 2012.

[91] Ning Lu, Zhenyu Li, and Jinlong Yang. Electronic structure engineering via on-plane chemical functionalization: a comparison study on two-dimensional polysilane and graphane. *The Journal of Physical Chemistry C*, 113(38):16741–16746, 2009.

[92] Hiroki Takamatsu and Tomonori Ohba. Water adsorption control by surface nanostructures on graphene-related materials by grand canonical monte carlo simulations. *Langmuir*, 37(50):14646–14656, 2021.

[93] Aleksandar Rikalo, Marina Nikolić, Marija Alanov, Aleksandar Vuković, Sanja J Armaković, and Stevan Armaković. A dft and md study of reactive, h2 adsorption and optoelectronic properties of graphane nanoparticles–an influence of boron doping. *Materials Chemistry and Physics*, 241:122329, 2020.

[94] RH Baughman, H Eckhardt, and M Kertesz. Structure-property predictions for new planar forms of carbon: Layered phases containing sp 2 and sp atoms. *The Journal of chemical physics*, 87(11):6687–6699, 1987.

[95] Hongyu Zhang, Mingwen Zhao, Hongxia Bu, Xiujie He, Meng Zhang, Lixia Zhao, and Youhua Luo. Ultra-high hydrogen storage capacity of li-decorated graphyne: A first-principles prediction. *Journal of Applied Physics*, 112(8):084305, 2012.

[96] Vikram Mahamiya, Alok Shukla, Nandini Garg, and Brahmananda Chakraborty. High-capacity reversible hydrogen storage in scandium decorated holey graphyne: Theoretical perspectives. *International Journal of Hydrogen Energy*, 47(12):7870–7883, 2022.

[97] Bohayra Mortazavi, Masoud Shahrokhi, Mohamed E Madjet, Tanveer Hussain, Xiaoying Zhuang, and Timon Rabczuk. N-, b-, p-, al-, as-, and ga-graphdiyne/graphyne lattices: first-principles investigation of mechanical, optical and electronic properties. *Journal of Materials Chemistry C*, 7(10):3025–3036, 2019.

[98] Qinyan Gu, Dingyu Xing, and Jian Sun. Superconducting single-layer t-graphene and novel synthesis routes. *Chinese Physics Letters*, 36(9):097401, 2019.

[99] Xiaoming Zhang, Lei Jin, Xuefang Dai, Guifeng Chen, and Guodong Liu. A record-high ion storage capacity of t-graphene as two-dimensional anode material for li-ion and na-ion batteries. *Applied Surface Science*, 527:146849, 2020.

[100] Xiao-Juan Ye, Chun-Sheng Liu, Wei Zhong, Zhi Zeng, and You-Wei Du. Metalized t graphene: A reversible hydrogen storage material at room temperature. *Journal of Applied Physics*, 116(11):114304, 2014.

[101] P Wang, S Orimo, T Matsushima, H Fujii, and Günter Majer. Hydrogen in mechanically prepared nanostructured h-bn: a critical comparison with that in nanostructured graphite. *Applied Physics Letters*, 80(2):318–320, 2002.

[102] Weiwei Lei, Hui Zhang, Ying Wu, Bao Zhang, Dan Liu, Si Qin, Zongwen Liu, Limin Liu, Yanming Ma, and Ying Chen. Oxygen-doped boron nitride nanosheets with excellent performance in hydrogen storage. *Nano Energy*, 6:219–224, 2014.

[103] Michael Rivera Mananghaya. Hydrogen saturation limit of ti-doped bn nanotube with bn defects: An insight from dft calculations. *international journal of hydrogen energy*, 43(22):10368–10375, 2018.

[104] Tiantian Wang, Chunbo Wang, Yajin Huo, and Mengjie Liu. Hydrogen storage in c-doped h-bn decorated with titanium atom: A computational study. *Chemical Physics Letters*, 803:139853, 2022.

[105] M Born and R Oppenheimer. Annalen der physik 389. *Issue*, 20(457):10, 1927.

[106] John Clarke Slater. The self consistent field and the structure of atoms. *Physical Review*, 32(3):339, 1928.

[107] JA Gaunt. A theory of hartree's atomic fields. In *Mathematical Proceedings of the Cambridge Philosophical Society*, volume 24, pages 328–342. Cambridge University Press, 1928.

[108] Douglas R Hartree. The wave mechanics of an atom with a non-coulomb central field. part i. theory and methods. In *Mathematical Proceedings of the Cambridge Philosophical Society*, volume 24, pages 89–110. Cambridge university press, 1928.

[109] Pierre Hohenberg and Walter Kohn. Inhomogeneous electron gas. *Physical review*, 136(3B):B864, 1964.

[110] Llewellyn H Thomas. The calculation of atomic fields. In *Mathematical proceedings of the Cambridge philosophical society*, volume 23, pages 542–548. Cambridge University Press, 1927.

[111] Enrico Fermi. Eine statistische methode zur bestimmung einiger eigenschaften des atoms und ihre anwendung auf die theorie des periodischen systems der elemente. *Zeitschrift für Physik*, 48(1):73–79, 1928.

[112] Walter Kohn and Lu Jeu Sham. Self-consistent equations including exchange and correlation effects. *Physical review*, 140(4A):A1133, 1965.

[113] John P Perdew. Density functional theory and the band gap problem. *International Journal of Quantum Chemistry*, 28(S19):497–523, 1985.

[114] Peter E Blöchl. Projector augmented-wave method. *Physical review B*, 50(24):17953, 1994.

[115] DR Hamann, M Schlüter, and C Chiang. Norm-conserving pseudopotentials. *Physical Review Letters*, 43(20):1494, 1979.

[116] O Krogh Andersen. Linear methods in band theory. *Physical Review B*, 12(8):3060, 1975.

[117] Michael P Marder. *Condensed matter physics*. John Wiley & Sons, 2010.

[118] Paolo Giannozzi, Stefano Baroni, Nicola Bonini, Matteo Calandra, Roberto Car, Carlo Cavazzoni, Davide Ceresoli, Guido L Chiarotti, Matteo Cococcioni, S. De Gironcoli S. Fabris G. Fratesi R. Gebauer U. Gerstmann C. Gougoussis A. Kokalj M. Lazzeri L. Martin-samos N. Marzari F. Mauri R. Mazzarello S. Paolini A. Pasquarello L. Paulatto C. Sbraccia S. Scandolo G. Sclauzero A. P. Seitsonen A. Smogunov P. Umari Dabo, A. D. Corso, and R. M. Wentzcovitch. Quantum espresso: a modular and open-source software project for quantum simulations of materials. *Journal of physics: Condensed matter*, 21(39):395502, 2009.

[119] Graeme Henkelman, Gísli Jóhannesson, and Hannes Jónsson. Methods for finding saddle points and minimum energy paths. In *Theoretical methods in condensed phase chemistry*, pages 269–302. Springer, 2002.

[120] Graeme Henkelman, Blas P Uberuaga, and Hannes Jónsson. A climbing image nudged elastic band method for finding saddle points and minimum energy paths. *The Journal of chemical physics*, 113(22):9901–9904, 2000.

[121] Richard Car and Mark Parrinello. Unified approach for molecular dynamics and density-functional theory. *Physical review letters*, 55(22):2471, 1985.

[122] Georg Kresse and Jürgen Hafner. Ab initio molecular dynamics for liquid metals. *Physical review B*, 47(1):558, 1993.

[123] Thomas D Kühne. Second generation car–parrinello molecular dynamics. *Wiley Interdisciplinary Reviews: Computational Molecular Science*, 4(4):391–406, 2014.

[124] M Mattesini, JM Soler, and F Yndurain. Ab initio study of metal-organic framework-5 zn 4 o (1, 4- benzenedicarboxylate) 3: An assessment of mechanical and spectroscopic properties. *Physical Review B*, 73(9):094111, 2006.

[125] John P Perdew, Kieron Burke, and Matthias Ernzerhof. Generalized gradient approximation made simple. *Physical review letters*, 77(18):3865, 1996.

[126] Koichi Momma and Fujio Izumi. Vesta 3 for three-dimensional visualization of crystal, volumetric and morphology data. *Journal of applied crystallography*, 44(6):1272–1276, 2011.

[127] Anton Kokalj. Computer graphics and graphical user interfaces as tools in simulations of matter at the atomic scale. *Computational Materials Science*, 28(2):155–168, 2003.

[128] Tim Mueller and Gerbrand Ceder. A density functional theory study of hydrogen adsorption in mof-5. *The Journal of Physical Chemistry B*, 109(38):17974–17983, 2005.

[129] Mudit Dixit, Tuhina Adit Maark, and Sourav Pal. Ab initio and periodic dft investigation of hydrogen storage on light metal-decorated mof-5. *International journal of hydrogen energy*, 36(17):10816–10827, 2011.

[130] R Lotfi and Y Saboohi. Effect of metal doping, boron substitution and functional groups on hydrogen adsorption of mof-5: A dft-d study. *Computational and Theoretical Chemistry*, 1044:36–43, 2014.

[131] Carlos O Areán, Sachin Chavan, Carlos P Cabello, Edoardo Garrone, and Gemma T Palomino. Thermodynamics of hydrogen adsorption on metal-organic frameworks. *ChemPhysChem*, 11(15):3237–3242, 2010.

[132] Anne Dailly, John J Vajo, and Channing C Ahn. Saturation of hydrogen sorption in zn benzenedicarboxylate and zn naphthalenedicarboxylate. *The Journal of Physical Chemistry B*, 110(3):1099–1101, 2006.

[133] David Durette, Pierre Bénard, Renju Zacharia, and Richard Chahine. Investigation of the hydrogen adsorbed density inside the pores of mof-5 from path integral grand canonical monte carlo at supercritical and subcritical temperature. *Science Bulletin*, 61(8):594–600, 2016.

[134] Tae Bum Lee, Daejin Kim, Dong Hyun Jung, Sang Beom Choi, Ji Hye Yoon, Jaheon Kim, Kihang Choi, and Seung-Hoon Choi. Understanding the mechanism of hydrogen adsorption into metal organic frameworks. *Catalysis Today*, 120(3-4):330–335, 2007.

[135] Amit Samanta, Terumi Furuta, and Ju Li. Theoretical assessment of the elastic constants and hydrogen storage capacity of some metal-organic framework materials. *The Journal of chemical physics*, 125(8):084714, 2006.

[136] M Abdellaoui, M Lakhal, H Benzidi, M Garara, A Benyoussef, A El Kenz, O Mounkachi, M Loulidi, and H Ez-Zahraouy. Enhancing of hydrogen storage properties of perovskite-type mgnih3 by introducing cobalt dopant (mgcoxni1- xh3) using first-principle calculations. *Applied Physics A*, 125(11):1–8, 2019.

[137] Jaeyong Joo, Hyungjun Kim, and Sang Soo Han. Volume shrinkage of a metal–organic framework host induced by the dispersive attraction of guest gas molecules. *Physical Chemistry Chemical Physics*, 15(43):18822–18826, 2013.

[138] C Wolverton and Alex Zunger. Short-and long-range order of the binary madelung lattice. *Physical Review B*, 51(11):6876, 1995.

[139] Yasuharu Okamoto and Yoshiyuki Miyamoto. Ab initio investigation of physisorption of molecular hydrogen on planar and curved graphenes. *The journal of physical chemistry B*, 105(17):3470–3474, 2001.

[140] Tatsuhiko Sagara, James Klassen, Julia Ortony, and Eric Ganz. Binding energies of hydrogen molecules to isoreticular metal-organic framework materials. *The Journal of chemical physics*, 123(1):014701, 2005.

[141] Diego A Gomez, Aldo F Combariza, and German Sastre. Quantum-chemistry calculations of hydrogen adsorption in mof-5. *Physical Chemistry Chemical Physics*, 11(40):9250–9258, 2009.

[142] Barbara Panella, Michael Hirscher, Hermann Pütter, and Ulrich Müller. Hydrogen adsorption in metal–organic frameworks: Cu-mofs and zn-mofs compared. *Advanced Functional Materials*, 16(4):520–524, 2006.

[143] Michael Hirscher and Barbara Panella. Hydrogen storage in metal–organic frameworks. *Scripta Materialia*, 56(10):809–812, 2007.

[144] Dan Zhao, Daqiang Yuan, and Hong-Cai Zhou. The current status of hydrogen storage in metal–organic frameworks. *Energy & Environmental Science*, 1(2):222–235, 2008.

[145] Tae Bum Lee, Dong Hyun Jung, Daejin Kim, Jaheon Kim, Kihang Choi, and Seung-Hoon Choi. Molecular dynamics simulation study on the hydrogen adsorption and diffusion in non-interpenetrating and interpenetrating irmofs. *Catalysis Today*, 146(1-2):216–222, 2009.

[146] Graeme Henkelman and Hannes Jónsson. Improved tangent estimate in the nudged elastic band method for finding minimum energy paths and saddle points. *The Journal of chemical physics*, 113(22):9978–9985, 2000.

[147] Kenichi Koizumi, Katsuyuki Nobusada, and Mauro Boero. Hydrogen storage mechanism and diffusion in metal–organic frameworks. *Physical Chemistry Chemical Physics*, 21(15):7756–7764, 2019.

[148] Mudit Dixit, Tuhina Adit Maark, Kamalika Ghatak, Rajiv Ahuja, and Sourav Pal. Scandium-decorated mof-5 as potential candidates for room-temperature hydrogen storage: a solution for the clustering problem in mofs. *The Journal of Physical Chemistry C*, 116(33):17336–17342, 2012.

[149] Sihai Yang, Xiang Lin, Alexander J Blake, K Mark Thomas, Peter Hubberstey, Neil R Champness, and Martin Schröder. Enhancement of h 2 adsorption in li+-exchanged co-ordination framework materials. *Chemical communications*, (46):6108–6110, 2008.

[150] Xiaolong Zou, Moon-Hyun Cha, Seungchul Kim, Manh Cuong Nguyen, Gang Zhou, Wenhui Duan, and Jisoon Ihm. Hydrogen storage in ca-decorated, b-substituted metal organic framework. *international journal of hydrogen energy*, 35(1):198–203, 2010.

[151] Li-Ming Yang, Ponniah Ravindran, Ponniah Vajeeston, Stian Svelle, and Mats Tilset. A quantum mechanically guided view of cd-mof-5 from formation energy, chemical bonding, electronic structure, and optical properties. *Microporous and mesoporous materials*, 175:50–58, 2013.

[152] Li-Ming Yang, Ponniah Vajeeston, Ponniah Ravindran, Helmer Fjellvåg, and Mats Tilset. Revisiting isoreticular mofs of alkaline earth metals: A comprehensive study on phase stability, electronic structure, chemical bonding, and optical properties of a–irmof-1 (a= be, mg, ca, sr, ba). *Physical Chemistry Chemical Physics*, 13(21):10191–10203, 2011.

[153] Tshiamo Segakweng, Nicholas M Musyoka, Jianwei Ren, Philip Crouse, and Henrietta W Langmi. Comparison of mof-5-and cr-mof-derived carbons for hydrogen storage application. *Research on Chemical Intermediates*, 42(5):4951–4961, 2016.

[154] I Cabria, MJ Lopez, and JA Alonso. Shape of the hydrogen adsorption regions of mof-5 and its impact on the hydrogen storage capacity. *Physical Review B*, 78(20):205432, 2008.

[155] F Ortmann, F Bechstedt, and WG Schmidt. Semiempirical van der waals correction to the density functional description of solids and molecular structures. *Physical Review B*, 73(20):205101, 2006.

[156] Hendrik J Monkhorst and James D Pack. Special points for brillouin-zone integrations. *Physical review B*, 13(12):5188, 1976.

[157] Li-Ming Yang, Ponniah Vajeeston, Ponniah Ravindran, Helmer Fjellvag, and Mats Tilset. Theoretical investigations on the chemical bonding, electronic structure, and optical properties of the metal- organic framework mof-5. *Inorganic chemistry*, 49(22):10283–10290, 2010.

[158] Y Marcus, MJ Kamlet, and RW Taft. Linear solvation energy relationships: standard molar gibbs free energies and enthalpies of transfer of ions from water into nonaqueous solvents. *The Journal of Physical Chemistry*, 92(12):3613–3622, 1988.

[159] H Benzidi, M Lakhal, M Abdellaoui, M Garara, A Benyoussef, M Loulidi, M Hamedoun, O Mounkachi, et al. Improved thermodynamic properties of doped libh4 for hydrogen storage: First-principal calculation. *International Journal of Hydrogen Energy*, 44(31):16793–16802, 2019.

[160] Sang Soo Han and William A Goddard. Lithium-doped metal-organic frameworks for reversible h2 storage at ambient temperature. *Journal of the American Chemical Society*, 129(27):8422–8423, 2007.

[161] Natarajan Sathiyamoorthy Venkataramanan, Ryoji Sahara, Hiroshi Mizuseki, and Yoshiyuki Kawazoe. Probing the structure, stability and hydrogen adsorption of lithium functionalized isoreticular mof-5 (fe, cu, co, ni and zn) by density functional theory. *International journal of molecular sciences*, 10(4):1601–1608, 2009.

[162] Li-Ming Yang. Quantum chemistry investigation of rigid a-irmof-m0 series (a= zinc, cadmium, and alkaline-earth metals) on crystal structure, electronic structure, formation energy, chemical bonding, and optical properties. *Microporous and mesoporous materials*, 183:218–233, 2014.

[163] Graeme Henkelman, Andri Arnaldsson, and Hannes Jónsson. A fast and robust algorithm for bader decomposition of charge density. *Computational Materials Science*, 36(3):354–360, 2006.

[164] Jae-Shin Lee. Binding energy of h 2 to mof-5: A model study. *Bulletin of the Korean Chemical Society*, 32(12):4199–4204, 2011.

[165] Junping Hu, Yu Liu, Ning Liu, Jianwen Li, and Chuying Ouyang. Theoretical prediction of t-graphene as a promising alkali-ion battery anode offering ultrahigh capacity. *Physical Chemistry Chemical Physics*, 22(6):3281–3289, 2020.

[166] Arka Bandyopadhyay, Atanu Nandy, Arunava Chakrabarti, and Debnarayan Jana. Optical properties and magnetic flux-induced electronic band tuning of a t-graphene

sheet and nanoribbon. *Physical Chemistry Chemical Physics*, 19(32):21584–21594, 2017.

[167] Gu Qinyan, Xing Dingyu, and Sun Jian. Erratum: Superconducting single-layer t-graphene and novel synthesis routes [< a href=. *Chinese Physics Letters*, 36(10):109901–109902, 2019.

[168] R Majidi. Electronic properties of t graphene-like c–bn sheets: a density functional theory study. *Physica E: Low-dimensional Systems and Nanostructures*, 74:371–376, 2015.

[169] Huayue Mei, Yuhan Zhong, Dafang He, Xue Du, Chunmei Li, and Nanpu Cheng. Elastic, electronic and optical properties of new 2d and 3d boron nitrides. *Scientific Reports*, 10(1):1–9, 2020.

[170] Stefan Grimme. Semiempirical gga-type density functional constructed with a long-range dispersion correction. *Journal of computational chemistry*, 27(15):1787–1799, 2006.

[171] James D Pack and Hendrik J Monkhorst. " special points for brillouin-zone integrations"—a reply. *Physical Review B*, 16(4):1748, 1977.

[172] B Chettri, PK Patra, Nguyen N Hieu, and DP Rai. Hexagonal boron nitride (h-bn) nanosheet as a potential hydrogen adsorption material: A density functional theory (dft) study. *Surfaces and Interfaces*, 24:101043, 2021.

[173] William M Haynes, David R Lide, and Thomas J Bruno. *CRC handbook of chemistry and physics*. CRC press, 2016.

[174] Kevin T Chan, JB Neaton, and Marvin L Cohen. First-principles study of metal adatom adsorption on graphene. *Physical Review B*, 77(23):235430, 2008.

[175] Yang-Xin Yu. Graphenylene: a promising anode material for lithium-ion batteries with high mobility and storage. *Journal of Materials Chemistry A*, 1(43):13559–13566, 2013.

[176] Charles Kittel, Paul McEuen, and Paul McEuen. *Introduction to solid state physics*, volume 8. Wiley New York, 1996.

[177] Vikram Mahamiya, Alok Shukla, and Brahmananda Chakraborty. Ultrahigh reversible hydrogen storage in k and ca decorated 4-6-8 biphenylene sheet. *International Journal of Hydrogen Energy*, 2022.

[178] Lucia Guadalupe Arellano, Francisco De Santiago, Álvaro Miranda, Luis Antonio Pérez, Fernando Salazar, Alejandro Trejo, Jun Nakamura, and Miguel Cruz-Irisson. Ab initio study of hydrogen storage on metal-decorated gec monolayers. *International Journal of Hydrogen Energy*, 46(57):29261–29271, 2021.

[179] LE Klebanoff and JO Keller. 5 years of hydrogen storage research in the us doe metal hydride center of excellence (mhcoe). *International Journal of Hydrogen Energy*, 38(11):4533–4576, 2013.

[180] Mina Yoon, Shenyuan Yang, Enge Wang, and Zhenyu Zhang. Charged fullerenes as high-capacity hydrogen storage media, 2007.

[181] Er Hong Song, Sung Ho Yoo, Jae Joon Kim, Shiau Wu Lai, Qing Jiang, and Sung Oh Cho. External electric field induced hydrogen storage/release on calcium-decorated single-layer and bilayer silicene. *Physical Chemistry Chemical Physics*, 16(43):23985–23992, 2014.

[182] Yafei Zhang, Pingping Liu, and Xiaoling Zhu. Li decorated penta-silicene as a high capacity hydrogen storage material: A density functional theory study. *International Journal of Hydrogen Energy*, 46(5):4188–4200, 2021.

[183] Chen Pan, Jiaoqiang Zhang, Kaichang Kou, Yu Zhang, and Guanglei Wu. Investigation of the through-plane thermal conductivity of polymer composites with in-plane oriented hexagonal boron nitride. *International Journal of Heat and Mass Transfer*, 120:1–8, 2018.

[184] S Rabab Naqvi, T Hussain, P Panigrahi, Wei Luo, and Rajeev Ahuja. Manipulating energy storage characteristics of ultrathin boron carbide monolayer under varied scandium doping. *RSC advances*, 7(14):8598–8605, 2017.

[185] Yusheng Wang, Yong Ji, Meng Li, Pengfei Yuan, Qiang Sun, and Yu Jia. Li and ca co-decorated carbon nitride nanostructures as high-capacity hydrogen storage media. *Journal of Applied Physics*, 110(9):094311, 2011.

[186] Yan Song, Hongshan Chen, Yan Zhang, and Yuehong Yin. High-capacity hydrogen storage on li-decorated b16n16. *Environmental Progress & Sustainable Energy*, 40(4):e13623, 2021.

[187] Hui An, Chun-sheng Liu, Zhi Zeng, Chao Fan, and Xin Ju. Li-doped b 2 c graphene as potential hydrogen storage medium. *Applied Physics Letters*, 98(17):173101, 2011.

[188] I Ya Nikiforov, VV Ilyasov, and N Yu Safontseva. Electronic energy structure of non-stoichiometric cubic boron nitride. *Journal of Physics: Condensed Matter*, 7(30):6035, 1995.

[189] I Cabria, MJ López, and JA Alonso. Enhancement of hydrogen physisorption on graphene and carbon nanotubes by li doping. *The Journal of chemical physics*, 123(20):204721, 2005.

[190] P Álvarez-Zapatero, A Herrero, A Lebon, LJ Gallego, and A Vega. Ab initio study of lithium decoration of popgraphene and hydrogen storage capacity of the hybrid nanostructure. *International Journal of Hydrogen Energy*, 46(29):15724–15737, 2021.

[191] Sezgin Aydin and Mehmet Şimşek. The enhancement of hydrogen storage capacity in li, na and mg-decorated bc3 graphene by clich and rich algorithms. *International Journal of Hydrogen Energy*, 44(14):7354–7370, 2019.

[192] Tanveer Hussain, Bohayra Mortazavi, Hyeonhu Bae, Timon Rabczuk, Hoonkyung Lee, and Amir Karton. Enhancement in hydrogen storage capacities of light metal functionalized boron–graphdiyne nanosheets. *Carbon*, 147:199–205, 2019.

[193] Majid EL Kassaoui, Mohamed Houmad, Marwan Lakhal, Abdelilah Benyoussef, Abdallah El Kenz, and Mohammed Loulidi. Hydrogen storage in lithium, sodium and magnesium-decorated on tetragonal silicon carbide. *International Journal of Hydrogen Energy*, 46(47):24190–24201, 2021.

[194] Nabil Khossossi, Younes Benhouria, Syeda R Naqvi, Pritam K Panda, Ismail Essaoudi, Abdelmajid Ainane, and Rajeev Ahuja. Hydrogen storage characteristics of li and na decorated 2d boron phosphide. *Sustainable Energy & Fuels*, 4(9):4538–4546, 2020.

[195] Ekaterina Anikina, Amitava Banerjee, Valery Beskachko, and Rajeev Ahuja. Li-decorated carbyne for hydrogen storage: charge induced polarization and van't hoff hydrogen desorption temperature. *Sustainable Energy & Fuels*, 4(2):691–699, 2020.

[196] JS Arellano, LM Molina, A Rubio, and JA Alonso. Density functional study of adsorption of molecular hydrogen on graphene layers. *The Journal of Chemical Physics*, 112(18):8114–8119, 2000.

[197] Yafei Li, Yunlong Liao, and Zhongfang Chen. Be2c monolayer with quasi-planar hexacoordinate carbons: a global minimum structure. *Angewandte Chemie International Edition*, 53(28):7248–7252, 2014.

[198] Mosayeb Naseri, Ali H Reshak, Arash Boochani, DP Rai, Laleh Farhang Matin, and Shahram Solaymani. Effect of si and ge surface doping on the be2c monolayer: Case study on electrical and optical properties. *Silicon*, 10(5):1893–1902, 2018.

[199] Gautam Sharma and KC Bhamu. Impressive electronic transport in be _2 c monolayer limited by phonon. *arXiv preprint arXiv:2003.07400*, 2020.

[200] Mosayeb Naseri, Jaafar Jalilian, Faribrz Parandin, and Khaled Salehi. A new stable polycrystalline be2c monolayer: a direct semiconductor with hexa-coordinate carbons. *Physics Letters A*, 382(32):2144–2148, 2018.

[201] Fanhao Jia, Yuting Qi, Shunbo Hu, Tao Hu, Musen Li, Guodong Zhao, Jihua Zhang, Alessandro Stroppa, and Wei Ren. Structural properties and strain engineering of a beb 2 monolayer from first-principles. *RSC advances*, 7(61):38410–38414, 2017.

[202] Hua-Liang Cao, Xin-Lu Cheng, and Hong Zhang. Beryllium carbide as diffusion barrier against cu: First-principles study. *Chinese Physics B*, 29(1):016601, 2020.

[203] Long Chen, Xianfei Chen, Jia Liu, Pan Xiang, Fuyu Zhuge, and Beibei Xiao. Li decorated be3c2 as light-weight host material for reversible hydrogen storage. *Applied Surface Science*, 459:217–223, 2018.

[204] Hyeondeok Shin, Sinabro Kang, Jahyun Koo, Hoonkyung Lee, Jeongnim Kim, and Yongkyung Kwon. Cohesion energetics of carbon allotropes: Quantum monte carlo study. *The Journal of chemical physics*, 140(11):114702, 2014.

[205] Chun-Sheng Liu, Hao-Hao Zhu, Xiao-Juan Ye, and Xiao-Hong Yan. Prediction of a new bec monolayer with perfectly planar tetracoordinate carbons. *Nanoscale*, 9(18):5854–5858, 2017.

[206] ND Drummond, Viktor Zolyomi, and VI Fal'Ko. Electrically tunable band gap in silicene. *Physical Review B*, 85(7):075423, 2012.

[207] H Liu, AT Neal, Z Zhu, Z Luo, X Xu, D Tománek, and PD Ye. Acs nano 2014, 8 (4), 4033–4041.

[208] M Garara, H Benzidi, M Lakhal, M Louilidi, H Ez-Zahraouy, A El Kenz, M Hamedoun, A Benyoussef, A Kara, and O Mounkachi. Phosphorene: A promising candidate for h2 storage at room temperature. *International Journal of Hydrogen Energy*, 44(45):24829–24838, 2019.

[209] Puspamitra Panigrahi, Dilip Acharya, Sheeba Rathina Selvi, Rajeev Ahuja, and Tanveer Hussain. Enhancing energy storage efficiency of lithiated carbon nitride

(c7n6) monolayers under co-adsorption of h2 and ch4. *International journal of hydrogen energy*, 46(38):19988–19997, 2021.

[210] Song Hu, Yongliang Yong, Caitao Li, Zijia Zhao, Huiwen Jia, and Yanmin Kuang. Si 2 bn monolayers as promising candidates for hydrogen storage. *Physical Chemistry Chemical Physics*, 22(24):13563–13568, 2020.

[211] Omar Faye, Tanveer Hussain, Amir Karton, and Jerzy Szpunar. Tailoring the capability of carbon nitride (c3n) nanosheets toward hydrogen storage upon light transition metal decoration. *Nanotechnology*, 30(7):075404, 2018.

[212] Ekaterina Anikina, Tanveer Hussain, Valery Beskachko, and Rajeev Ahuja. Elucidating hydrogen storage properties of two-dimensional siligraphene (sic 8) monolayers upon selected metal decoration. *Sustainable Energy & Fuels*, 4(11):5578–5587, 2020.

[213] Syeda R Naqvi, Tanveer Hussain, Wei Luo, and Rajeev Ahuja. Metallized siligraphene nanosheets (sic7) as high capacity hydrogen storage materials. *Nano Research*, 11(7):3802–3813, 2018.

[214] A Sibari, Z Kerrami, A Kara, and M Benaissa. Strain-engineered p-type to n-type transition in mono-, bi-, and tri-layer black phosphorene. *Journal of Applied Physics*, 127(22):225703, 2020.

[215] Shuichi Nosé. A unified formulation of the constant temperature molecular dynamics methods. *The Journal of chemical physics*, 81(1):511–519, 1984.

[216] Janet Wong, Shwetank Yadav, Jasmine Tam, and Chandra Veer Singh. A van der waals density functional theory comparison of metal decorated graphene systems for hydrogen adsorption. *Journal of Applied Physics*, 115(22):224301, 2014.

[217] Zhiyang Liu, Tanveer Hussain, Amir Karton, and Süleyman Er. Empowering hydrogen storage properties of haeckelite monolayers via metal atom functionalization. *Applied Surface Science*, 556:149709, 2021.

Appendix A

List of publications

- *Published papers on hydrogen storage:*

1. **Majid EL Kassaoui**, M. Lakhal, A. Benyoussef, A. El Kenz, M. Loulidi, and O. Mounkachi. Improvement of the hydrogen storage performance of t-graphene-like two-dimensional boron nitride upon selected lithium decoration.*Phys. Chem. Chem. Phys*,24 (2022) 15048-15059.

2. **Majid EL Kassaoui**, Z. Mansouri, A. Al-Shami, A. Sibari, A. Benyoussef, A. El Kenz, O. Mounkachi, M. Loulidi, Design of metal-decorated beryllium carbide (Be_2C) as a high-capacity hydrogen storage material with strong adsorption characteristics. *Applied Surface Science* 589 (2022) 152960.

3. **Majid EL Kassaoui**, M. Houmad, M. Lakhal, A. Benyoussef, A. El Kenz, M. Loulidi, Hydrogen storage in lithium, sodium and magnesium-decorated on tetragonal silicon carbide, *Int. J. Hydrogen Energy.* 46 (2021) 24190–24201.

4. **Majid EL Kassaoui**, M. Lakhal, M. Abdellaoui, A. Benyoussef, A. El Kenz, M. Loulidi, Modeling hydrogen adsorption in the metal organic framework (MOF-5, connector): $Zn_4O(C_8H_4O_4)_3$,*Int. J. Hydrogen Energy.* 45 (2020) 33663–33674.

5. **Majid EL Kassaoui**, M. Lakhal, A. Benyoussef, A.El Kenz, M. Loulidi, Effect of zinc substitution by magnesium and cadmium on hydrogen storage properties of connector-metal-organic framework-5, *Journal of Alloys and Compounds.* 874 (2021) 159902.

6. **Majid EL Kassaoui**, M. Lakhal, A. Benyoussef, A.El Kenz, M. Loulidi, Enhancement of hydrogen storage properties of metal-organic framework-5 by substitution

(Zn, Cd and Mg) and decoration (Li, Be and Na), *Int. J. Hydrogen Energy.* 46 (2021) 26426-26436

7. **Majid EL Kassaoui**, M. Lakhal, A. Benyoussef, A.El Kenz, M. Loulidi. Scandium/Lithium-Decorated c-MOF-10 as potential material for High-capacity hydrogen storage: An ab initio DFT and AIMD Study, 2023 (in preparation)

8. **Majid EL Kassaoui**, M. Lakhal, A. Benyoussef, A. El Kenz, M. Loulidi, and O. Mounkachi. Towards hydrogen storage properties of Li and Na decorated 3D-Ch, 2023 (in preparation)

- *Other publications:*

1. M. Ait Tamerd, **Majid EL Kassaoui**, B. Abraime, A. Marjaoui, M. El Marssi, A. Benyoussef, A.El Kenz, A. Lahmar. First-principles investigation on multiferroic properties of BiFeO3-REMnO3 (RE= Er, Eu, Gd, Ho, La, Tb). *Materials Today Communications.* 29 (2021) 102976.

2. M. Ait Tamerd, **Majid EL Kassaoui**, A. Marjaoui, A.El Kenz, A. Benyoussef, M. El Marssi, M. Bouchaib, A. Lahmar. "Magnetic, Electronic, and Electrical Properties of Tri-Layered SrMO3/BaTiO3/SrMO3 (M= Ru and Os): First-Principles Investigations.*Journal of Superconductivity and Novel Magnetism* (2022) 1-7.

Appendix B

List of conferences and Seminars

1. 8th International Conference On Materials and Energy (ICOME 2022), Baku, Azerbaijan, 22^{nd}-25^{th} May 2022 .
   Oral: Hydrogen Storage in Metal-Organic Framework-5 (MOF-5).

2. Fifth Edition International Conference Nano-TN 2022 : Nano-Materials: Theory and Experiments, Marrakech, Morocco, 4-7 May 2022.
   Oral: High-capacity reversible hydrogen storage in two-dimensional materials (2D): A combination of DFT and ab initio molecular dynamics study.

3. The first edition of Condensed Matter, Optics and Nanosciences Days (JMCON-2021), UM6P-Ben Guerir, Morocco, 23-24 December 2021.
   Oral: Ab Initio Study of two-dimensional materials: A route to achieving a suitable hydrogen storage medium.

4. Inter-Lab-LaMCScI-LERMA-Annual Meeting-2019, FSR-Rabat, Morocco, 11-12 December 2019.
   Oral: Quantum-chemistry calculations of hydrogen adsorption in Metal Organic Framework (MOF-5, Connector): a DFT Study.

5. Physics Doctoriales Days'22, FSR-Rabat, Morocco, 18-22 July 2022.
   Oral: Recent advances on simulation and theory of Hydrogen Storage in Metal–Organic Framework-5 and 2D-Materials.

6. Seminar series: Quantum physics and mathematics for materials, UM6P-Ben Guerir, Morroco, 2022.
   Oral: Porous two-dimensional materials for hydrogen storage applications: Innovations and challenges.

7. Journées Nationales des Doctorants et Jeunes Chercheurs, FSR-Rabat, Morocco, 24-26 Novembre 2022.

Oral: Hydrogen adsorption in the context of hydrogen storage using solid-state materials.

8. International Symposium Nanomaterials: Microstructure and Properties (TRAMP19), Cadi Ayyad University-Marrakech, Morroco, 07-09 November 2019.
   Poster: Modeling the adsorption of hydrogen in the metal organic frameworks (MOFs, connector).